

2017

# Computational modeling of impact and deformation

Feifei Wang  
*Iowa State University*

Follow this and additional works at: <https://lib.dr.iastate.edu/etd>



Part of the [Applied Mathematics Commons](#), [Computer Sciences Commons](#), and the [Robotics Commons](#)

---

## Recommended Citation

Wang, Feifei, "Computational modeling of impact and deformation" (2017). *Graduate Theses and Dissertations*. 15451.  
<https://lib.dr.iastate.edu/etd/15451>

This Dissertation is brought to you for free and open access by the Iowa State University Capstones, Theses and Dissertations at Iowa State University Digital Repository. It has been accepted for inclusion in Graduate Theses and Dissertations by an authorized administrator of Iowa State University Digital Repository. For more information, please contact [digirep@iastate.edu](mailto:digirep@iastate.edu).

**Computational modeling of impact and deformation**

by

**Feifei Wang**

A dissertation submitted to the graduate faculty  
in partial fulfillment of the requirements for the degree of

**DOCTOR OF PHILOSOPHY**

Co-majors: Applied Mathematics; Computer Science

Program of Study Committee:  
Yan-Bin Jia, Co-major Professor  
Scott Hansen, Co-major Professor  
David Fernandez-Baca  
Paul Sacks  
Sourabh Bhattacharya

The student author and the program of study committee are solely responsible for the content of this dissertation. The Graduate College will ensure this dissertation is globally accessible and will not permit alterations after a degree is conferred.

Iowa State University

Ames, Iowa

2017

Copyright © Feifei Wang, 2017. All rights reserved.

## DEDICATION

I would like to dedicate this thesis to my parents Jinggang Wang, Chunjuan Zhang and to my husband Benjamin Kollasch, without whose support I would not have been able to complete this work.

## TABLE OF CONTENTS

<b>LIST OF TABLES</b> . . . . .	vi
<b>LIST OF FIGURES</b> . . . . .	vii
<b>ACKNOWLEDGEMENTS</b> . . . . .	x
<b>ABSTRACT</b> . . . . .	xi
<b>CHAPTER 1. INTRODUCTION</b> . . . . .	1
<b>CHAPTER 2. ANALYSIS AND COMPUTATION OF TWO BODY IM- PACT IN THREE DIMENSIONS</b> . . . . .	3
2.1 Introduction . . . . .	3
2.2 Impact Equations . . . . .	5
2.2.1 Some properties of Matrices . . . . .	8
2.2.2 Impact Solution . . . . .	8
2.2.3 Sufficient Condition for Impact Solution . . . . .	11
2.3 Sliding Velocity . . . . .	12
2.4 Initial Slip and Invariant Directions . . . . .	13
2.5 Vanishing of Sliding Velocity . . . . .	15
2.5.1 Stick . . . . .	16
2.5.2 Resumed Slip . . . . .	17
2.6 Solution of the Impact Problem . . . . .	19
2.6.1 Fast Numerical Integration . . . . .	20
2.6.2 Sliding Velocity at Zero . . . . .	22
2.6.3 Start of Straight Sliding . . . . .	23
2.6.4 Impact Algorithm and Execution Examples . . . . .	27

<b>CHAPTER 3. COMPUTATIONAL MODELING OF <i>N</i>-BODY COLLISIONS WITH SIMULATION AND EXPERIMENT . . . . .</b>	<b>31</b>
3.1 Introduction . . . . .	31
3.2 Frictionless Collision of Translating Balls . . . . .	32
3.2.1 Impact dynamics and contact kinematics . . . . .	33
3.2.2 Numerical integration . . . . .	36
3.2.3 Example . . . . .	36
3.3 Collision under General Motions with Friction . . . . .	38
3.3.1 Impact dynamics and contact kinematics . . . . .	38
3.3.2 Sticking mode . . . . .	40
3.3.3 Sliding mode . . . . .	41
3.3.4 Algorithm . . . . .	42
3.4 Simulation and experiment . . . . .	42
3.4.1 Newton’s cradle . . . . .	43
3.4.2 Billiard break shots . . . . .	44
<b>CHAPTER 4. PLANNING THE CONTACT VELOCITY FOR ROBOTIC BATTING . . . . .</b>	<b>47</b>
4.1 Introduction . . . . .	47
4.2 Impact Dynamics and Invariant Directions . . . . .	48
4.3 Solution Impulse . . . . .	52
4.4 Finding an Initial Contact Velocity . . . . .	53
4.4.1 Cone of Impulses from Sticking and Straight Sliding . . . . .	53
4.4.2 Solution Contact Velocity in an Invariant Direction . . . . .	55
4.4.3 Closed-Form Solution . . . . .	55
4.4.4 Bounding Triangle Method . . . . .	59
4.5 Simulation Results . . . . .	63
4.5.1 Comparisons Among Three Algorithms . . . . .	63
4.5.2 Success Rate . . . . .	64
4.6 Discussion and Future Work . . . . .	65

<b>CHAPTER 5. EXPLICIT SOLUTIONS AND COEFFICIENT OF RESTI-</b>	
<b>TUTION FOR AN ELASTIC ROD WITH VISCOUS DAMPING . . . . .</b>	<b>67</b>
5.1 Introduction . . . . .	67
5.2 Explicit integral representation of solution . . . . .	70
5.2.1 Calculation of jumps along characteristics . . . . .	73
5.2.2 Calculation of contact time . . . . .	75
5.3 Momentum, Center of Mass, and Energy . . . . .	80
5.3.1 Momentum and Center of Mass . . . . .	80
5.3.2 Energy decomposition . . . . .	83
5.4 Coefficient of restitution . . . . .	86
5.4.1 Momentum coefficient of restitution . . . . .	87
5.4.2 Energetic coefficient of restitution . . . . .	88
5.5 Conclusion . . . . .	92
<b>CHAPTER 6. PICKING UP SOFT OBJECTS AND RECOVERING GRAV-</b>	
<b>ITY FREE SHAPE IN 3D . . . . .</b>	<b>95</b>
6.1 Introduction . . . . .	95
6.2 Picking up soft 3D objects with two fingers . . . . .	96
6.2.1 Theoretical background . . . . .	96
6.2.2 Simulations and experiments . . . . .	101
6.3 Recovering the gravity-free shape of a 3D deformable object . . . . .	103
6.3.1 FEM applied in computing the deformation . . . . .	105
6.3.2 The case of one tetrahedron . . . . .	107
6.3.3 General shape . . . . .	114
6.3.4 Simulation, experiment and results . . . . .	119
<b>CHAPTER 7. SUMMARY AND DISCUSSION . . . . .</b>	<b>124</b>
<b>APPENDIX A. STIFFNESS MATRIX CONSTRUCTION . . . . .</b>	<b>126</b>
<b>APPENDIX B. NUMERICAL COMPUTATION OF <math>\mathcal{E}(t_1)</math> . . . . .</b>	<b>130</b>
<b>APPENDIX C. ELASTIC ROD WITH STRUCTURAL DAMPING . . . . .</b>	<b>132</b>

**LIST OF TABLES**

Table 2.1	Impact computation comparisons . . . . .	28
Table 3.1	Comparisons of experimental and simulation outcomes . . . . .	44
Table 3.2	Parameters used for modeling break shots . . . . .	45
Table 3.3	Effect of ball-ball friction during impact . . . . .	46
Table 4.1	Comparison among the three different algorithms . . . . .	64
Table 6.1	Information of the objects . . . . .	102
Table 6.2	Young's modulus with total work . . . . .	102
Table 6.3	Convergence condition (b) analysis . . . . .	113
Table 6.4	Information of measurements . . . . .	122

## LIST OF FIGURES

Figure 2.1	Impact between two bodies . . . . .	5
Figure 2.2	Impacts between two balls and between a ball and a half-space . . . . .	7
Figure 2.3	Configuration of impact between an icosahedron and a tetrahedron . . . . .	10
Figure 2.5	Hodographs of instances of the icosahedron-tetrahedron impact . . . . .	14
Figure 2.6	Impulse curve for the icosahedron-tetrahedron impact . . . . .	17
Figure 2.7	Bundle of 15 hodographs from the icosahedron-tetrahedron collision . . . . .	18
Figure 2.8	Hodograph of the impact instance . . . . .	19
Figure 2.9	Bundle of 13 hodographs from the icosahedron-tetrahedron collision . . . . .	20
Figure 2.10	Curvature based step size for numerical integration. . . . .	21
Figure 2.12	More hodographs of the icosahedron-tetrahedron impact . . . . .	25
Figure 2.13	Part of seven cases with simulation examples. . . . .	26
Figure 2.14	Part of seven cases with simulation examples. . . . .	27
Figure 2.15	Part of seven cases with simulation examples. . . . .	28
Figure 2.16	Configuration of impact between a bowling pin and a ball . . . . .	29
Figure 3.1	Contact modeling with virtual springs. . . . .	33
Figure 3.2	Newton's cradle initial status . . . . .	37
Figure 3.3	Impulse decomposition along normal and tangential directions. . . . .	39
Figure 3.4	Initial State of Newton's cradle . . . . .	43
Figure 3.5	Comparison of Newton's cradle . . . . .	44
Figure 3.6	Billiards break shot. . . . .	45
Figure 3.8	Resting configurations of ten balls . . . . .	46
Figure 3.9	Initial State of two balls . . . . .	46



Figure 4.1	Impact between a tetrahedron object and a cuboid bat . . . . .	49
Figure 4.2	The 2D cone contains all the total impulses . . . . .	54
Figure 4.3	Solution impulse curve . . . . .	59
Figure 4.4	Relationship between $\mathbf{v}^-$ and the projection on the plane . . . . .	60
Figure 4.5	Projection plane and bounding box demonstration . . . . .	60
Figure 4.6	Centroid-based updates over trajectories in order to pass through $Q$ .	62
Figure 4.7	Midpoint-based updates over trajectories in order to pass through $Q$ .	63
Figure 4.8	Centroid algorithm iterations . . . . .	63
Figure 4.9	Finding solutions of 10 random target points . . . . .	65
Figure 4.10	When rotating the bat, the volume swept out by the impulse cones . .	66
Figure 5.1	Plot for $\Psi_r(t)$ with different $r$ values . . . . .	79
Figure 5.2	Plot for $\mathcal{E}_z(t_b)$ . . . . .	87
Figure 5.3	Plot for $\mathcal{E}_h(t_b)/\mathcal{E}(0)$ , $\mathcal{E}_z(t_b)/\mathcal{E}(0)$ , $\mathcal{E}_z(t_b)$ . . . . .	88
Figure 5.4	Plot for $\mathcal{E}_h(t_1)/\mathcal{E}(0)$ change with $\mu$ . . . . .	90
Figure 5.5	Plot for $\mathcal{E}_h(t_1)/\mathcal{E}(t_1)$ change with $\mu$ . . . . .	92
Figure 5.6	Plot for $\mathcal{E}(t_1)/\mathcal{E}(0)$ change with $\mu$ . . . . .	93
Figure 5.7	Plot for $\frac{\mathcal{E}(t_1)/\mathcal{E}(0)}{e^{-2rt_1}}$ change with $\mu$ . . . . .	94
Figure 6.1	Lifting up a 3D object . . . . .	97
Figure 6.2	Sliding of a node on the hemispherical finger . . . . .	100
Figure 6.3	Picking up objects successfully . . . . .	103
Figure 6.4	Relations between the Young's modulus and total work . . . . .	104
Figure 6.5	A tetrahedron . . . . .	108
Figure 6.6	Convergence analysis of single tetrahedron . . . . .	112
Figure 6.7	Iteration comparisons . . . . .	113
Figure 6.8	A ball sitting on a table under gravity . . . . .	119
Figure 6.9	Curves from the simulation . . . . .	120
Figure 6.10	Gelatin pudding . . . . .	120
Figure 6.11	Mesh representation of the pudding . . . . .	121

Figure 6.12	Gelatin with recovered shape mesh . . . . .	121
Figure 6.13	Experiments and simulation pictures of the flipped gelatin . . . . .	122
Figure 6.14	2-norm of the vector $\Delta$ during the iterations at $l$ th step . . . . .	123
Figure 6.15	2-norm of the logarithm . . . . .	123
Figure B.1	Integration regions $A$ , $B$ and $C$ . . . . .	131
Figure C.1	Plot for $v(x, t)$ . . . . .	140
Figure C.2	Plot for $v_x(0, t)$ . . . . .	141
Figure C.3	Plot for $E(t)$ using a different method . . . . .	141
Figure C.4	Plot for integration of $v_{xt}^2$ with $t$ from 0 to $T$ . . . . .	142
Figure C.5	Plot for integration of $v_{xt}^2$ with $t$ from 0 to $T$ with more terms . . . . .	142
Figure C.6	summary of COR computed by $(\mathcal{E}(0) + \Delta\mathcal{E}(t))/\mathcal{E}(0)$ . . . . .	142

## ACKNOWLEDGEMENTS

I would like to take this opportunity to express my thanks to those who helped me with various aspects of conducting research and the writing of this thesis.

First and foremost, Dr. Yan-Bin Jia and Dr. Scott Hansen for their guidance, patience and support for me both mentally and financially throughout this research and the writing of this thesis. I would like to thank all my lab mates as well, especially Feng Guo, Huan Lin and Jacob Stimes. They gave me a lot of help during my thesis work. I would also like to thank my committee members for their efforts and contributions to this work: Dr. Paul Sacks, Dr. David Fernandez-Baca and Dr. Sourabh Bhattacharya.

Finally, I would like to thank my friends and family for their loving guidance and assistance during the writing of this work.

Support of this research was provided in part by Iowa State University (ISU), and in part by the National Science Foundation through the grant IIS-0915876 , IIS-1421034 and DMS-1312952. Any opinions, findings and thoughts discussed in this material are those of the author and do not necessarily reflect the views of the National Science Foundation.

## ABSTRACT

This thesis tackles several problems arising in robotics and mechanics: analysis and computation of two- and multi-body impacts, planning a contact velocity for robotic batting, impact of an elastic rod onto a fixed foundation, robotic pickup of soft three-dimensional objects, and recovery of their gravity-free shapes.

Impact is an event that lasts a very short period of time but generates a very large interaction force. Assuming Stronge's energy-based restitution, a formal impulse-based analysis is presented for the collision of two rigid bodies at single contact point under Coulomb friction in three dimensions (3D). Based on this analysis, we describe a complete algorithm to take advantage of fast numerical integration and closed-form evaluation. For a simultaneous collision involving more than two bodies, we describe a general computational model for predicting its outcome.

Based on the impact model, we then look into the task of planning an initial contact velocity between a bat and an in-flight object to send the latter to a target. In certain situations, a closed-form solution can be found, while in others, a bounding triangle algorithm of iterative nature can be employed.

An alternative way of modeling impact is to consider the engaged objects to be elastic rather than rigid. A damped one-dimensional wave equation can model an elastic rod bouncing off the ground at a given initial velocity, under the influence of gravity. We derive an explicit solution based on the Method of Descent and D'Alembert's formula. We also obtain formulas for the time of contact and analyze the dependence of the energetic coefficient of restitution on the physical constants.

I conclude the thesis with two pieces of work involving deformable objects. First, an algorithm for picking up a 3D object is introduced. Homotopy continuation method is applied to solve a non-linear system for slips between objects and fingers. Some simulation and experi-

mental results are compared. Second, I discuss an iterative fixed-point method for recovering the gravity-free shape of an object. An experiment shows that the resulting stiffness matrix gives better predictions on deformations than the conventional stiffness matrix influenced by gravity.

## CHAPTER 1. INTRODUCTION

Collision is a common phenomenon in life. For example, it happens during car accidents, billiard games and so on. Simulation of collisions is important in earthquake modeling, automobile impact tests, the movie industry and some gaming/virtual reality applications. The computation of deformations of soft objects is also very challenging. Interesting projects can be seen in programming a robot to manipulate contact and impulsive forces of various objects, such as tomato, ping pong balls and automobile parts.

This thesis describes modeling of two-body and multi-body impact in three dimensions; planning the contact velocity in robotic batting; finding explicit solutions of elastic rod impact the ground; methods of grasping soft objects and recovering objects' gravity-free shapes.

Chapter 1 gives a brief introduction on each of the topics.

In Chapter 2, a complete impulse based model for solving two body impact in 3D is introduced. The model keeps track of the growing normal impulse, and computes other physical parameters, such as energy and so on, based on their differential relationships with respect to normal impulse. Closed form analysis is applied to the computation of the collision outcome. A curvature-based step size algorithm is introduced to speed up numerical integration process. At the end, we also do comparisons among different methods for two different impact instances.

In Chapter 3, the focus is on computing multi-body collisions. A general model is proposed to simulate the physical process and compute the post-impact velocity of each object. The whole system is initialized by first solving for the proportions of impulses on each pair of contacting objects, based on their impulse differential relationships. At the same time, the net impulse on each pair of objects is reduced to a function of the primary objects' normal impulse. Numerical calculations are then carried out through the growth of primary normal impulse to obtain the final results.

Chapter 4 discusses planning the initial contact velocity in a robotic batting task. In order to bat a flying object toward a target in 3D, the object's post-impact velocity must obey certain constraints, so does the initial contact velocity. We present a closed-form solution approach as well as numerical iterative methods for solving this type of problem.

In Chapter 5, instead of modeling the collision as virtual springs connecting rigid bodies, the study focuses on the problem of an elastic rod bouncing on a fixed foundation. A one dimensional wave equation with viscous damping is used as the model. The resulting PDE forms a (nonlinear) Signorini problem, which means the boundary condition changes depending upon whether the rod is in contact with the foundation. Based on this formulation, we compute

- contact time
- motion of center of mass
- momentum
- translational and vibrational energy
- momentum based coefficient of restitution
- energy based coefficient of restitution

Chapter 6 presents methods of picking up soft objects and discusses recovering gravity free shape of 3D objects. At the beginning, an algorithm of picking up a 3D object from table is introduced. The Homotopy Continuation Method is applied to solve the non-linear system of equations describing the sliding distance between objects and fingers. Then, we compare simulation results based on the algorithm with experimental data.

Later in Chapter 6, we also describe iteration methods for recovering the gravity-free shape of objects based upon their constitutive equations. The data will show that using the gravity-free situation constructed stiffness matrix predicts better result than using the stiffness matrix constructed under gravity.

Chapter 7 gives a brief summary and concludes the thesis.

## CHAPTER 2. ANALYSIS AND COMPUTATION OF TWO BODY IMPACT IN THREE DIMENSIONS

This chapter discusses a complete algorithm for two body collisions in 3D. The objects are rigid, and there is assumed to exist a virtual spring connecting the two objects at a single contact point. This spring stores energy, and will compress and reconstitute as the impact process goes on. The post-impact velocities of objects will be solved from the total impulse accumulated during the collision. The whole process follows the growth of normal impulse as the base parameter, and all other parameters have relationships with impulse. Energy has a differential relationship with normal impulse, and when the energy decreases back to zero, it indicates the end of impact. Impulse is related to the tangential velocity, which is governed by an ODE system. Usually it doesn't have a closed form solution, except in special situations such as when straight sliding happens or when sliding velocity vanishes. Invariant directions are proposed for the sake of more detailed analysis. Those terms are all explained in this chapter in detail. The complete algorithm makes use of closed form analysis in different cases, and also combines numerical integration using the modified curvature based step size. It gives results fast and accurately. Simulation has been done for two impact instances, and also verifies the theories of specific cases discussed. At the end, there are comparison tables among different numerical methods to demonstrate the efficiency and accuracy of the algorithm that is proposed and focused on in this chapter.

### 2.1 Introduction

Collision happens over a very short period of time and generates large forces. Newton's second law using the integral form gives the impulse, which is a finite quantity during the impact.



The model assumes a virtual spring in between the rigid bodies that can store energy. People in earlier time proposed different hypotheses for the relationships of physical parameters before and after impact. They are velocities, impulses and energy in different impact phases (compression and restitution) proposed by Newton (1686), Poisson (1827), and Stronge (1990). Those are also corresponds to three different types of coefficients of restitution: kinematic, kinetic and energetic. The involve of friction also requires the computation of tangential impulse relative to normal impulse. Brach (1989) and Smith (1991) proposed some untheoretically justified ratios. There are other people Glocker and Pfeiffer (1995), Stewart (2000), and Chatterjee and Ruina (1998) using linear complementarity formulation methods to solve the problem, but did not catch the nature of the physical process.

Section 2.2 introduces the set up of impact equations according to theories. This includes impulse relationship with velocities changes; local principle frame, rotation matrices and so on relationship with change of angular velocities. The impact solution scheme and differential relationships between energy and impulse are described. Besides, there are several specific examples stated in order to help readers following the idea. It is still a hard problem to prove the termination of the impact model. However, a sufficient condition was proposed such that under certain condition, the impact process will end. This model can also be easily adjusted to apply to the frictionless case just by setting frictional coefficient to be zero.

Section 2.3 discusses the relationship between impulse and sliding velocity, which is very important to see why the tangential velocity plays a key role in the system.

Section 2.4 discusses of how to compute invariant directions and their meanings, including centripetal and centrifugal directions. A theorem is proposed to discuss the number and type of invariant directions.

Section 2.5 deals with the situation when sliding velocity goes down to zero. Either sticking or resumed sliding will happen in this situation, which depends on a judging condition according to Coulomb's friction law. Different hodographs from simulation are also presented to help illustrate the different conditions and situations.

Section 2.6 proposes a detailed process of computing the solution of impact problem. Straight sliding is now introduced besides vanishing of sliding velocity, since it can lead to closed

form for the ODE of tangential velocity. When closed form can be applied to the ODE that tangential velocity yields, there are in general seven different cases can happen. Each of them is computed based on the order of events happening, including end of sliding, start of straight sliding, end of compression, end of restitution and so on. Besides, a faster way of numerical integration is proposed based on the curvature of the velocity hodograph.

## 2.2 Impact Equations

Assume two bodies  $\mathcal{B}_1$  and  $\mathcal{B}_2$  colliding at a point  $\mathbf{c}$  as shown in Fig. 2.1. Without loss

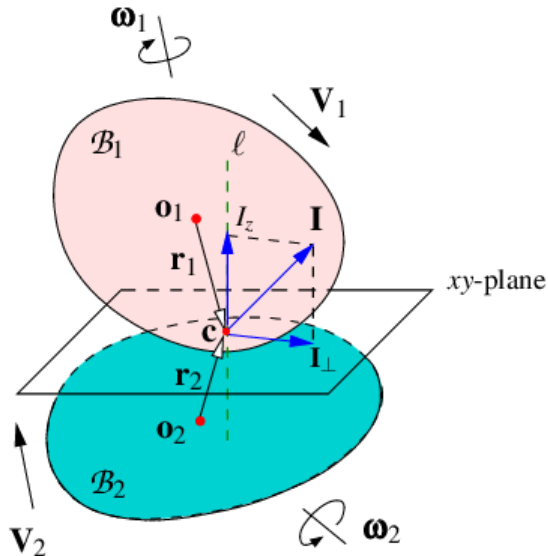


Figure 2.1: Impact between two bodies. The impulse  $\mathbf{I}$  consists components of normal impulse  $I_z$  along their contact normal and tangential component  $\mathbf{I}_\perp$  (in the  $xy$  plane) if there is contact friction.

of generality, we place the world frame  $\mathcal{W}$  at  $\mathbf{c}$ , and the  $z$ -axis points to the inward surface normal of  $\mathcal{B}_1$ . Thus, the tangential plane is also the  $xy$ -plane. We define the local principal body frames  $\mathcal{F}_i$  with origin at their center of mass  $\mathbf{o}_i$ , such that the inertia matrices  $Q_i$  are diagonal in these frames. The rotation matrix from the world frame to the local principal frame is  $R_i$ . The vector pointing from the center of mass to the contact point is  $\mathbf{r}_i = \mathbf{c} - \mathbf{o}_i$ . Let  $\mathbf{V}_i$  and  $\boldsymbol{\omega}_i$  be the velocity and angular velocity of the body  $\mathcal{B}_i$  respectively. The definitions

of direct/oblique, central/eccentric follow from (Stronge, 2004b, pp.2–3). The symbols of ‘−’ and ‘+’ in the superscripts denote values just before and after the impact.

$\mathbf{F}$  denotes the contact force exerted on  $\mathcal{B}_1$  by  $\mathcal{B}_2$ . Gravity is ignored since it is negligible compared to the very large impulse force. Newton’s and Euler’s equations are

$$\begin{aligned}\mathbf{F} &= m_1 \dot{\mathbf{V}}_1, \\ R_1^{-1}(\mathbf{r}_1 \times \mathbf{F}) &= Q_1 \dot{\boldsymbol{\omega}}_1 + \boldsymbol{\omega}_1 \times Q_1 \boldsymbol{\omega}_1,\end{aligned}$$

where we let dot ‘.’ be differentiation with respect to time. Integrate the above equations over time,

$$\begin{aligned}\mathbf{I} &= m_1 \Delta \mathbf{V}_1, \\ R_1^{-1}(\mathbf{r}_1 \times \mathbf{I}) &= Q_1 \Delta \boldsymbol{\omega}_1.\end{aligned}$$

$\mathbf{I}$  is the impulse exerted by  $\mathcal{B}_2$  onto  $\mathcal{B}_1$ .  $\Delta \mathbf{V}_1$  and  $\Delta \boldsymbol{\omega}_1$  are the changes in  $\mathbf{V}_1$  and  $\boldsymbol{\omega}_1$ . The impact equations for  $\mathcal{B}_2$  can be set up similarly. Together we have

$$\begin{aligned}\Delta \mathbf{V}_1 &= \frac{1}{m_1} \mathbf{I} & \text{and} & \quad \Delta \boldsymbol{\omega}_1 = Q_1^{-1} R_1^{-1}(\mathbf{r}_1 \times \mathbf{I}), \\ \Delta \mathbf{V}_2 &= -\frac{1}{m_2} \mathbf{I} & \text{and} & \quad \Delta \boldsymbol{\omega}_2 = -Q_2^{-1} R_2^{-1}(\mathbf{r}_2 \times \mathbf{I}).\end{aligned}\tag{2.1}$$

The contact velocity (of  $\mathcal{B}_1$  relative to  $\mathcal{B}_2$ ) at  $\mathbf{c}$  is

$$\mathbf{v} = (v_x, v_y, v_z)^T = \mathbf{V}_1 + (R_1 \boldsymbol{\omega}_1) \times \mathbf{r}_1 - \mathbf{V}_2 - (R_2 \boldsymbol{\omega}_2) \times \mathbf{r}_2.\tag{2.2}$$

Denote by  $P_i$  the antisymmetric matrix such that  $P_i \mathbf{u} = \mathbf{r}_i \times \mathbf{u}$  for all vectors  $\mathbf{u} \in \mathbb{R}^3$ , and by  $U_3$  the  $3 \times 3$  identity matrix  $\text{diag}(1, 1, 1)$ . Let

$$S = P_1 R_1 Q_1^{-1} R_1^{-1} P_1 + P_2 R_2 Q_2^{-1} R_2^{-1} P_2.\tag{2.3}$$

By (4.2) :

$$\begin{aligned}\Delta \mathbf{v} &= \Delta \mathbf{V}_1 + (R_1 \Delta \boldsymbol{\omega}_1) \times \mathbf{r}_1 - \Delta \mathbf{V}_2 - (R_2 \Delta \boldsymbol{\omega}_2) \times \mathbf{r}_2 \\ &= \mathbf{W} \mathbf{I},\end{aligned}\tag{2.4}$$

by plugging in (4.1), where

$$\mathbf{W} = \left( \frac{1}{m_1} + \frac{1}{m_2} \right) U_3 - S.\tag{2.5}$$

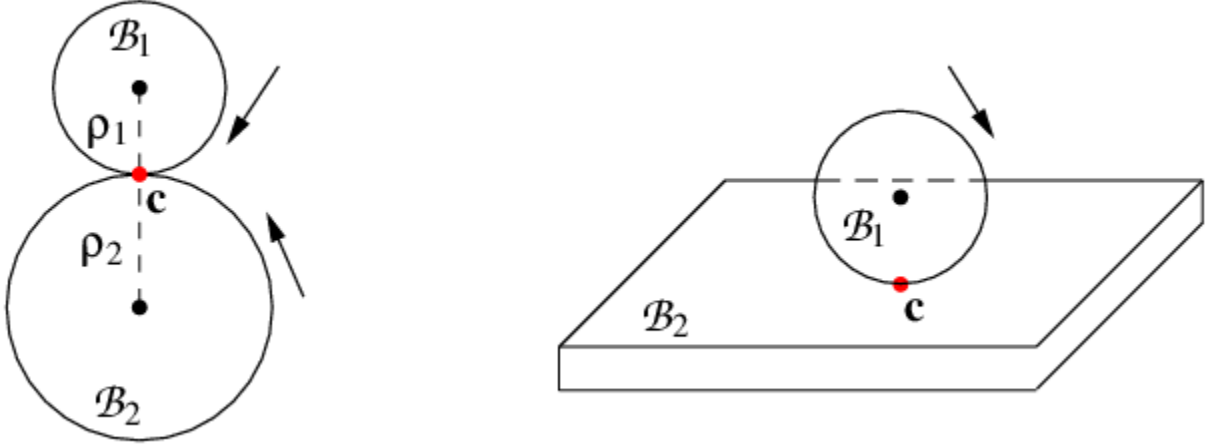


Figure 2.2: Impacts (a) between two balls and (b) between a ball and a half-space with infinite mass.

Fig. 2.2(a) shows a ball ( $\mathcal{B}_1$ ) of radius  $\rho_1$  impacting another ball ( $\mathcal{B}_2$ ) of radius  $\rho_2$ . Let the body frames of  $\mathcal{F}_1$  and  $\mathcal{F}_2$  have the same orientations as that of the world frame  $\mathcal{W}$ . Note that  $\mathbf{r}_1 = (0, 0, -\rho_1)^T$  and  $\mathbf{r}_2 = (0, 0, \rho_2)^T$ , thus

$$P_1 = \begin{pmatrix} 0 & \rho_1 & 0 \\ -\rho_1 & 0 & 0 \\ 0 & 0 & 0 \end{pmatrix} \quad \text{and} \quad P_2 = \begin{pmatrix} 0 & -\rho_2 & 0 \\ \rho_2 & 0 & 0 \\ 0 & 0 & 0 \end{pmatrix}.$$

Their inertia matrix  $Q_i = \frac{2}{5}m_i\rho_i^2U_3$ . Then

$$S = \sum_{i=1}^2 \frac{5}{2m_i\rho_i^2} P_i P_i = -\frac{5}{2} \left( \frac{1}{m_1} + \frac{1}{m_2} \right) \begin{pmatrix} 1 & 0 & 0 \\ 0 & 1 & 0 \\ 0 & 0 & 0 \end{pmatrix},$$

$$W = \left( \frac{1}{m_1} + \frac{1}{m_2} \right) \begin{pmatrix} \frac{7}{2} & 0 & 0 \\ 0 & \frac{7}{2} & 0 \\ 0 & 0 & 1 \end{pmatrix}.$$

Let  $\mathcal{B}_1$  be a ball but let  $\mathcal{B}_2$  to be a half-space with infinite mass and thus infinite moments of inertia about its principal axes. It is shown in Fig. 2.2(b). One obtains  $W = \frac{1}{2m_1} \text{diag}(7, 7, 2)$ .

### 2.2.1 Some properties of Matrices

Matrix  $W$  in (2.5) is called the *inverse inertia matrix* (Stronge, 2004b, p. 66).

**Lemma 1** *The matrix  $S$  defined in (2.3) is symmetric. It is negative definite if  $\mathbf{o}_1$ ,  $\mathbf{o}_2$ , and  $\mathbf{c}$  are not collinear, and negative semi-definite otherwise.*

**Proof** Since  $P_i^T = -P_i$ ,  $(Q_i^{-1})^T = Q_i^{-1}$ , and  $R_i^{-1} = R_i^T$ , the symmetry of  $S$  follows from

$$\begin{aligned} S^T &= \sum_{i=1}^2 (P_i R_i Q_i^{-1} R_i^{-1} P_i)^T = \sum_{i=1}^2 (-P_i) R_i Q_i^{-1} R_i^T (-P_i) \\ &= \sum_{i=1}^2 P_i R_i Q_i^{-1} R_i^T P_i = S. \end{aligned}$$

Suppose  $\mathbf{u} \neq \mathbf{0}$ . We have, for  $i = 1, 2$ ,

$$\begin{aligned} \mathbf{u}^T (P_i R_i Q_i^{-1} R_i^{-1} P_i) \mathbf{u} &= (\mathbf{u}^T P_i R_i) Q_i^{-1} (R_i^T P_i \mathbf{u}) \\ &= -(R_i^T P_i \mathbf{u})^T Q_i^{-1} (R_i^T P_i \mathbf{u}) \\ &\leq 0, \end{aligned} \tag{2.6}$$

because  $Q_i^{-1}$  is positive definite. Hence  $\mathbf{u}^T S \mathbf{u} \leq 0$ .

In (2.6), the product is zero if and only if  $R_i^T P_i \mathbf{u} = R_i^{-1}(\mathbf{r}_i \times \mathbf{u}) = \mathbf{0}$ , which is equivalent to  $\mathbf{r}_i \times \mathbf{u} = \mathbf{0}$  in the world frame. Therefore, by (2.3),  $\mathbf{u}^T S \mathbf{u} = 0$  if and only if  $\mathbf{r}_1 \times \mathbf{u} = \mathbf{r}_2 \times \mathbf{u} = \mathbf{0}$ , or equivalently, if and only if  $\mathbf{u}$  is collinear with the vectors from the origin to  $\mathbf{o}_1$  and  $\mathbf{o}_2$ . Trivial reasoning from here establishes the second statement of the theorem.  $\square$

By Lemma 1, the matrix  $-S$  is positive semidefinite. From (2.5),  $W$  is the sum of  $-S$  with the positive definite matrix  $(\frac{1}{m_1} + \frac{1}{m_2})U_3$ .

**Proposition 2** *The inverse inertia matrix  $W$  is symmetric and positive definite.*

### 2.2.2 Impact Solution

Two-body impact has two phases: compression and restitution. During compression, normal contact velocity  $v_z$  increases from pre-impact value  $v_z^- < 0$  to zero. Based on (4.3),

$$v_z = \hat{\mathbf{z}}^T(\mathbf{v}^- + \Delta \mathbf{v}) = v_z^- + \hat{\mathbf{z}}^T W \mathbf{I}.$$

We can decompose  $\mathbf{v}$ ,  $\mathbf{F}$  and  $\mathbf{I}$  for tangential and normal components as follows

$$\mathbf{v} = \mathbf{v}_\perp + v_z \hat{\mathbf{z}} = v_x \hat{\mathbf{x}} + v_y \hat{\mathbf{y}} + v_z \hat{\mathbf{z}}, \quad (2.7)$$

$$\mathbf{F} = \mathbf{F}_\perp + F_z \hat{\mathbf{z}} = F_x \hat{\mathbf{x}} + F_y \hat{\mathbf{y}} + F_z \hat{\mathbf{z}}, \quad (2.8)$$

$$\mathbf{I} = I_t + I_z \hat{\mathbf{z}} = I_x \hat{\mathbf{x}} + I_y \hat{\mathbf{y}} + I_z \hat{\mathbf{z}}, \quad (2.9)$$

where  $\hat{\mathbf{x}}$ ,  $\hat{\mathbf{y}}$ , and  $\hat{\mathbf{z}}$  in the world frame  $\mathcal{W}$  are the unit vectors in the directions of  $x$ -,  $y$ -, and  $z$ -axes. Here, the subscript ‘ $\perp$ ’ means tangential component. Variable  $\mu$  is the coefficient of friction.

Let ‘ $'$ ’ denote differentiation with respect to  $I_z$ . From Jia (2012b),  $E' = -v_z$ . By (4.3),

$$\begin{aligned} E' &= -v_z^- - \hat{\mathbf{z}}^T \mathbf{W} \mathbf{I} \\ &= -v_z^- - \left( \frac{1}{m_1} + \frac{1}{m_2} \right) I_z + \hat{\mathbf{z}}^T \mathbf{S} \mathbf{I}. \end{aligned} \quad (2.10)$$

Let  $e$  be *energetic coefficient of restitution*.

During impact process, the normal impulse  $I_z$  increases. Denote the following:

$$\begin{aligned} I_{zc} &: \text{value of } I_z \text{ at which compression ends } (v_z = 0); \\ I_{zr} &: \text{(positive) value of } I_z \text{ at which restitution ends } (E = 0); \\ \mathbf{I}_c &: \text{value of } \mathbf{I} \text{ when } I_z = I_{zc}; \\ \mathbf{I}_r &: \text{value of } \mathbf{I} \text{ when } I_z = I_{zr}, \text{ i.e., the total impulse}; \\ E_c &: \text{value of } E \text{ when } I_z = I_{zc}, \text{ i.e., maximum value of } E. \end{aligned} \quad (2.11)$$

The idea of solving impact problem is as follows

1. Solve  $E' = -v_z = 0$  for  $I_{zc}$  with (2.10) and  $\mathbf{I}(I_z)$  plugged in.
2. Integrating (2.10) over  $[0, I_{zc}]$  start from zero to get  $E_c$  at the end of compression.
3. Apply energy loss by a factor of  $1 - e^2$  at the end of compression. The beginning of restitution starts with energy initial value  $e^2 E_c$ . Then integrating (2.10) over  $[I_{zc}, I_z]$  to get the value.
4. Solve  $E = 0$  to get  $I_{zr}$  and  $\mathbf{I}_r$ .

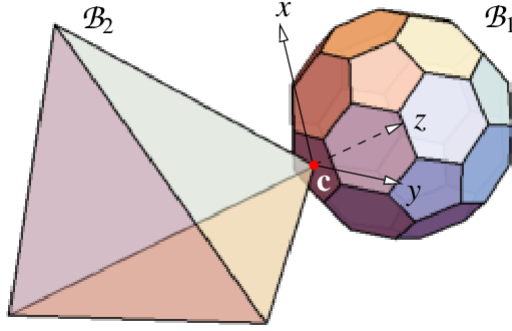


Figure 2.3: Configuration of impact ( $\mu = 0.8$  and  $e = 0.95$ ) between an icosahedron  $\mathcal{B}_1$  and tetrahedron  $\mathcal{B}_2$ , both with uniform mass density. All pentagons and hexagons on  $\mathcal{B}_1$  have side length 0.1. The  $x$ - $y$  plane is the extension of pentagon face of  $\mathcal{B}_1$ , whose center coincides with a vertex of  $\mathcal{B}_2$  at  $\mathbf{c}$ . The vector from  $\mathbf{c}$  to the vertex of the contacting pentagon with the largest  $y$ -coordinate rotates from the  $y$ -axis about the  $z$ -axis (through  $\mathcal{B}_1$ 's center of geometry) through  $\pi/10$ . The remaining three vertices of the tetrahedron are  $(0, 0, -0.75)^T$ ,  $(0.5, 0, -0.5)$ , and  $(0, 0.5, -0.5)$ . Other parameters include:  $\mathbf{o}_1 = (0, 0, 0.232744)^T$ ,  $\mathbf{o}_2 = (0.125, 0.125, -0.4375)^T$ ,  $m_1 = 3.0$ ,  $m_2 = 1.0$ ,  $Q_1 = 0.0671673 U_3$ , and  $Q_2 = \text{diag}(0.017239, 0.022813, 0.027135)$ .

5. Using (4.1) with  $\mathbf{I} = \mathbf{I}_r$  to get the post-impact velocities  $\mathbf{V}_i^+ = \mathbf{V}_i^- + \Delta \mathbf{V}_i$  and  $\boldsymbol{\omega}_i^+ = \boldsymbol{\omega}_i^- + \Delta \boldsymbol{\omega}_i$ ,  $i = 1, 2$ .

Fig. 2.3 demonstrates an impact example between an icosahedron and a tetrahedron.

Here,

$$W = \begin{pmatrix} 11.5984 & -0.910367 & 2.44236 \\ -0.910367 & 9.90134 & 1.95747 \\ 2.44235 & 1.95746 & 2.59042 \end{pmatrix}. \quad (2.12)$$

The pre-impact velocities are

$$\begin{aligned} \mathbf{V}_1^- &= (-0.1, 0.5, 0.95)^T, & \boldsymbol{\omega}_1^- &= (0.1, 0.1, 0.1)^T, \\ \mathbf{V}_2^- &= (0.1, 0.1, 1)^T, & \boldsymbol{\omega}_2^- &= (0.1, -0.1, 0.1)^T. \end{aligned} \quad (2.13)$$

The total impulse, computed by Algorithm 1 to be described in Section 2.6, is

$$\mathbf{I}_r = (-0.00326657, -0.0592263, 0.1007)^T. \quad (2.14)$$

The post-impact velocities are:

$$\begin{aligned}\mathbf{V}_1^+ &= (-0.101089, 0.480258, 0.983567)^T, \\ \boldsymbol{\omega}_1^+ &= (0.138764, -0.100369, 0.0755903)^T, \\ \mathbf{V}_2^+ &= (0.103267, 0.159226, 0.8993)^T, \\ \boldsymbol{\omega}_2^+ &= (-0.281687, 0.402075, 0.589565)^T.\end{aligned}$$

### 2.2.3 Sufficient Condition for Impact Solution

It is an interesting question to know if the impact process will eventually end, which also means if energy of the virtual spring will decrease to zero. The derivatives of  $v'_z$ , by using (4.3) and (2.9):

$$v'_z = \frac{d}{dI_z}(v_z^- + \hat{\mathbf{z}}^T \Delta \mathbf{v}) = \hat{\mathbf{z}}^T W \mathbf{I}' = \hat{\mathbf{z}}^T W \hat{\mathbf{z}} + \hat{\mathbf{z}}^T W \mathbf{I}'_{\perp}.$$

Meanwhile,

$$\mathbf{I}'_{\perp} = d\mathbf{I}_{\perp}/dI_z = \dot{\mathbf{I}}_{\perp}/\dot{I}_z = \mathbf{F}_{\perp}/F_z. \quad (2.15)$$

We consider the following theorem,

**Theorem 3** *Suppose the following condition holds:*

$$\hat{\mathbf{z}}^T W \hat{\mathbf{z}} + \mu \hat{\mathbf{z}}^T W \hat{\mathbf{s}} > 0, \quad \text{for all tangent vectors } \hat{\mathbf{s}}. \quad (2.16)$$

*Then the impact process as modeled in Section 2.2.2 will end.*

**Proof** Suppose that (2.16) holds. Let  $b > 0$  be the minimum value of  $\hat{\mathbf{z}}^T W \hat{\mathbf{z}} + \mu \hat{\mathbf{z}}^T W \hat{\mathbf{s}}$  for all tangent vectors  $\hat{\mathbf{s}}$ . Since  $\|\mathbf{I}'_{\perp}\| \leq \mu$  under Coulomb's law, we infer from (2.15) that  $v'_z \geq b$ . Thus,  $v_z$  will increase to zero monotonically to end compression. After compression,  $E$  will decrease at the rate of  $v_z$ , which will continue to increase at a rate at least  $b$ . Thus,  $E$  will decrease to zero to end restitution.  $\square$

This condition (2.16) is a sufficient condition for the impact process to end. We suppose it is satisfied in this chapter's discussion.



### 2.3 Sliding Velocity

The sliding velocity in the tangential plane, which is also  $x - y$  plane, has the components  $\boldsymbol{\gamma} = (v_x, v_y)^T$ . We obtain

$$\begin{aligned}\boldsymbol{\gamma} &= (\hat{\boldsymbol{x}}, \hat{\boldsymbol{y}})^T \boldsymbol{v} &&= (\hat{\boldsymbol{x}}, \hat{\boldsymbol{y}})^T (\boldsymbol{v}^- + W\boldsymbol{I}) && \text{(by (4.3))} \\ &= \boldsymbol{\gamma}^- + (\hat{\boldsymbol{x}}, \hat{\boldsymbol{y}})^T W\boldsymbol{I} &&= \boldsymbol{\gamma}^- + (\hat{\boldsymbol{x}}, \hat{\boldsymbol{y}})^T W(I_x \hat{\boldsymbol{x}} + I_y \hat{\boldsymbol{y}} + I_z \hat{\boldsymbol{z}}) \\ &= \boldsymbol{\gamma}^- + B \begin{pmatrix} I_x \\ I_y \end{pmatrix} + I_z \boldsymbol{d},\end{aligned}\tag{2.17}$$

where

$$B = (\hat{\boldsymbol{x}}, \hat{\boldsymbol{y}})^T W (\hat{\boldsymbol{x}}, \hat{\boldsymbol{y}}),\tag{2.18}$$

$$\boldsymbol{d} = (\hat{\boldsymbol{x}}, \hat{\boldsymbol{y}})^T W \hat{\boldsymbol{z}}.\tag{2.19}$$

An example of impact configuration in Fig. 2.3 has

$$B = \begin{pmatrix} 11.5985 & -0.910369 \\ -0.910369 & 9.90134 \end{pmatrix} \text{ and } \boldsymbol{d} = \begin{pmatrix} 2.44236 \\ 1.95747 \end{pmatrix}.\tag{2.20}$$

Central impact always has result of  $\boldsymbol{d} = \mathbf{0}$ , because of  $\boldsymbol{r}_i \times \hat{\boldsymbol{z}} = \mathbf{0}$ . Thus,

$$R_i^T (\boldsymbol{r}_i \times \hat{\boldsymbol{z}}) = \mathbf{0} \Leftrightarrow R_i^T P_i \hat{\boldsymbol{z}} = \mathbf{0} \Rightarrow P_i R_i Q_i^{-1} R_i^T P_i \hat{\boldsymbol{z}} = \mathbf{0},$$

for  $i = 1, 2$ . Then,  $S\hat{\boldsymbol{z}} = \mathbf{0}$  implies  $\hat{\boldsymbol{x}}^T S\hat{\boldsymbol{z}} = \hat{\boldsymbol{y}}^T S\hat{\boldsymbol{z}} = \mathbf{0}$ , and therefore  $\boldsymbol{d} = \mathbf{0}$ .

**Proposition 4** *The  $2 \times 2$  matrix  $B$  is symmetric and positive definite.*

**Proof** The symmetry of  $B$  follows directly from (2.18) and the symmetry of  $W$ . Given any  $\boldsymbol{u} \in \mathbb{R}^2$  and  $\boldsymbol{u} \neq \mathbf{0}$ , we have

$$\boldsymbol{u}^T (\hat{\boldsymbol{x}}, \hat{\boldsymbol{y}})^T W (\hat{\boldsymbol{x}}, \hat{\boldsymbol{y}}) \boldsymbol{u} = \left( (\hat{\boldsymbol{x}}, \hat{\boldsymbol{y}}) \boldsymbol{u} \right)^T W \left( (\hat{\boldsymbol{x}}, \hat{\boldsymbol{y}}) \boldsymbol{u} \right) > 0,$$

because  $(\hat{\boldsymbol{x}}, \hat{\boldsymbol{y}}) \boldsymbol{u} \neq \mathbf{0}$  and  $W$  is positive definite. □

Under Proposition 4, the inverse  $B^{-1}$  exists. From (2.17) we obtain:

$$\begin{pmatrix} I_x \\ I_y \end{pmatrix} = B^{-1} (\gamma_{yz} - \gamma_{yz}^- - I_z \boldsymbol{d}).\tag{2.21}$$

If  $\gamma_{yz}$  is fixed at  $\mathbf{0}$ , then all possible impulses  $\mathbf{I}$  to realize it form a line (parameterized with  $I_z$ ), referred to as the *line of sticking*, in the impulse space:<sup>1</sup>

$$\mathcal{L}_s : \begin{pmatrix} I_x \\ I_y \end{pmatrix} + B^{-1}(\gamma_{yz}^- + I_z \mathbf{d}) = \mathbf{0}. \quad (2.22)$$

Write the impulse and its derivative as follows:

$$\mathbf{I} = I_z \hat{\mathbf{z}} + (\hat{\mathbf{x}} \hat{\mathbf{y}}) B^{-1}(\gamma_{yz} - \gamma_{yz}^- - I_z \mathbf{d}), \quad (2.23)$$

$$\mathbf{I}' = \hat{\mathbf{z}} + (\hat{\mathbf{x}}, \hat{\mathbf{y}}) B^{-1}(\gamma'_{yz} - \mathbf{d}). \quad (2.24)$$

## 2.4 Initial Slip and Invariant Directions

From (2.15),

$$\begin{pmatrix} I'_x \\ I'_y \end{pmatrix} = \begin{pmatrix} F_x \\ F_y \end{pmatrix} / F_z = -\mu \hat{\boldsymbol{\gamma}}, \quad (2.25)$$

where  $\hat{\boldsymbol{\gamma}} = \gamma_{yz} / \|\gamma_{yz}\|$ . From (2.25),

$$\mathbf{I}' = \hat{\mathbf{z}} - \mu(\hat{\mathbf{x}}, \hat{\mathbf{y}}) \hat{\boldsymbol{\gamma}}. \quad (2.26)$$

Differentiate (2.17) and then substitute (2.25) in:

$$\boldsymbol{\gamma}' = B \begin{pmatrix} I'_x \\ I'_y \end{pmatrix} + \mathbf{d} = -\mu B \hat{\boldsymbol{\gamma}} + \mathbf{d}. \quad (2.27)$$

This is the most important ODE through out this chapter. The sliding velocity is a hodograph evolving with the parameter  $I_z$ . This ODE usually does not have closed form solution, except when  $\boldsymbol{\gamma} = \mathbf{0}$  or  $\boldsymbol{\gamma} \times (-\mu B \hat{\boldsymbol{\gamma}} + \mathbf{d}) = \mathbf{0}$ . Suppose  $\boldsymbol{\gamma}_l \neq \mathbf{0}$  so it has the direction  $\hat{\boldsymbol{\gamma}}_l$ . Then by the collinear relationship,

$$\boldsymbol{\gamma} = \boldsymbol{\gamma}_l + \lambda(I_z - I_{zl}) \hat{\boldsymbol{\gamma}}_l. \quad (2.28)$$

Depending on the sign of  $\lambda$ , the norm of sliding velocity may increase, decrease or stays. Fig. 2.5(a) shows the hodograph of the impact instance in Fig. 2.3. In the figure,  $\boldsymbol{\gamma}_c$  and  $\boldsymbol{\gamma}_r$  are the values of  $\gamma_{yz}$  at the end of compression and restitution.

$\hat{\boldsymbol{\gamma}}_l$  is called *invariant* since the sliding velocity  $\gamma_{yz}$  starting at  $\boldsymbol{\gamma}_l$  will have the collinear relationship. Every invariant direction is identified with a unit vector  $\hat{\mathbf{s}} \in \mathbb{R}^2$  satisfying the

---

<sup>1</sup>That  $\mathbf{I}$  reaches the line does not necessarily mean that the contact will become sticking

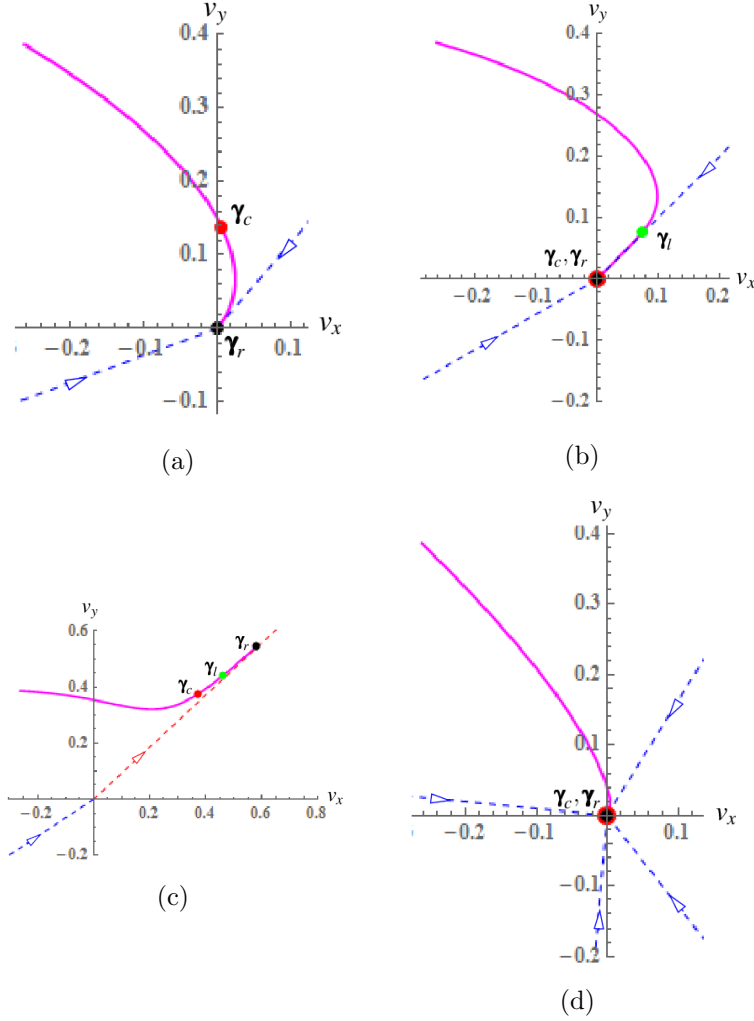


Figure 2.5: Hodographs of four instances of the icosahedron-tetrahedron impact in Fig. 2.3, with changing parameters from caption and (2.13): (a) no change; (b)  $\mu = 0.4$  and  $V_{1z}^- = 0.2$ ; (c)  $\mu = 0.25$  and  $V_{1z}^- = 0.2$ ; and (d)  $\mu = 3.0$  and  $V_{1z}^- = 0.5$ . Here,  $V_{1z}^-$  is the  $z$ -component of the pre-impact velocity  $\mathbf{V}_1^-$  of the icosahedron. Centripetal invariant direction is the blue dashed line. The line is labeled with an arrow pointing towards the origin to indicate the magnitude change of the sliding velocity in this direction. Centrifugal invariant direction is marked as red dashed line. This line is labeled with an arrow pointing away from the origin.

following equation:

$$\hat{\mathbf{s}} \times (-\mu B \hat{\mathbf{s}} + \mathbf{d}) = 0. \quad (2.29)$$

Such  $\hat{\mathbf{s}}$  is called *centripetal invariant* Elkaranshawy (2007) if  $\hat{\mathbf{s}}^T(-\mu B \hat{\mathbf{s}} + \mathbf{d}) \leq 0$ , and *centrifugal invariant* if  $\hat{\mathbf{s}}^T(-\mu B \hat{\mathbf{s}} + \mathbf{d}) > 0$ . Invariant directions only depend on the impact configuration and the coefficient of friction.

**Theorem 5** *Let  $\lambda_1, \lambda_2 > 0$  be the two eigenvalues of  $B$ . The following statements hold:*

- (i) *If  $\lambda_1 = \lambda_2$  and  $\mathbf{d} = \mathbf{0}$ , every unit vector  $\hat{\mathbf{s}} \in \mathbb{R}^2$  is an invariant direction.*
- (ii) *Otherwise, there exist two to four invariant directions.*
- (iii) *If  $\|B^{-1}\mathbf{d}\| \leq \mu$ , every invariant direction is centripetal.*
- (iv) *If  $\|B^{-1}\mathbf{d}\| > \mu$ , there exists at least one centripetal invariant direction and exactly one centrifugal invariant direction.*

The detailed proof of the theorem can be seen in Jia and Wang (2016).

The hodograph will stay and not cross the sectors by the invariant direction rays. For the icosahedron-tetrahedron impact in Fig. 2.3, we have  $\|B^{-1}\mathbf{d}\| = 0.3157$  from (2.20). Fig. 2.5(b)–(d) shows the hodographs of three instances of the impact with modified values of  $\mu$  and  $\mathbf{V}_1^-$ . Fig. 2.5(b), satisfying  $\|B^{-1}\mathbf{d}\| < \mu$ , has two centripetal directions. Fig. 2.5(c), satisfying  $\|B^{-1}\mathbf{d}\| > \mu$ , has a centripetal direction and a centrifugal direction. Fig. 2.5(d) shows four centripetal invariant directions but no centrifugal invariant direction since  $\|B^{-1}\mathbf{d}\| < \mu$ .

## 2.5 Vanishing of Sliding Velocity

If at some value  $I_z = I_{zs}$ ,  $\gamma$  becomes  $\mathbf{0}$ , then either sticking or resumed sliding will happen. This will be introduced next. Note that  $I_{zs} = 0$  if  $\gamma^- = \mathbf{0}$ . In order for sticking to happen, the sliding velocity will have to stay at zero, which means  $\gamma' = \mathbf{0}$ . Plugging in to (2.27), one can get the tangential impulse differential relationship as

$$\begin{pmatrix} I'_x \\ I'_y \end{pmatrix} = -B^{-1}\mathbf{d}. \quad (2.30)$$

To maintain sticking, Coulomb's friction law implies that  $\|\mathbf{F}_\perp/\mathbf{F}_z\| = \|\mathbf{I}'_\perp\| = \sqrt{I_x'^2 + I_y'^2} \leq \mu$ . If the condition  $\|B^{-1}\mathbf{d}\| \leq \mu$  can't be satisfied, then the contact can't stick, instead, resumed sliding will happen. Notice that  $B$  and  $\mathbf{d}$  were computed based on only the pre-impact physical parameters, which are just constants. This indicates that we can predict exactly if sticking or resumed sliding will happen during the impact once the sliding velocity vanishes.

### 2.5.1 Stick

Sticking mode happens when  $\|B^{-1}\mathbf{d}\| \leq \mu$ , as reasoned in the previous paragraph. Plug  $\boldsymbol{\gamma} = \mathbf{0}$  into (2.23), we get impulse in terms of  $I_z$ :

$$\mathbf{I} = I_z \hat{\mathbf{z}} - (\hat{\mathbf{x}}, \hat{\mathbf{y}}) B^{-1} (\boldsymbol{\gamma}^- + I_z \mathbf{d}), \quad I_z \geq I_{zs}. \quad (2.31)$$

This defines the *line of sticking* Bhatt and Koechling (1995), which means when sticking happens, the impulse curve will grow along this line. For a central impact,  $\mathbf{d} = \mathbf{0}$  and  $B^{-1}\mathbf{d} = \mathbf{0}$ . Thus, the sticking condition will always be satisfied. This implies when  $\boldsymbol{\gamma} = \mathbf{0}$  for central impact, sticking will happen.

The 3D impulse curve from impact instance in Fig. 2.3 is given in Fig. 2.6, based on the pre-impact velocities from (2.13).  $B$  and  $\mathbf{d}$  are computed from in (2.20). This also corresponds to graph Fig. 2.5(a). When the curve reaches  $\mathbf{I}_c$ , it means compression ends. When the curve reaches  $\mathbf{I}_s$ , it means sliding velocity vanishes. In this specific example,  $\|B^{-1}\mathbf{d}\| = 0.3157 < \mu = 0.8$ , so sticking happens instead of resumed sliding. Starting from the moment of sticking, the impulse curve will grow along the line of sticking until the end of restitution at  $\mathbf{I}_r$  given in (2.14). The impact instances in Fig. 2.5 (b) and (d) also have sticking mode happens.

The hodograph of the solution curve from ODE in (2.27) is determined by matrix  $B$ , vector  $\mathbf{d}$ ,  $\boldsymbol{\gamma}^-$ . The extension depends on  $v_z^-$ . Fig. 2.7 shows bundles of hodographs with initial sliding velocity on a unit circle. Those curves evolve towards the origin. All except  $\boldsymbol{\gamma}_i$ ,  $1 \leq i \leq 4$ , will go to the origin and stay there because of sticking mode.  $\boldsymbol{\gamma}_1$  and  $\boldsymbol{\gamma}_5$  are straight line segments starting from the centripetal directions.

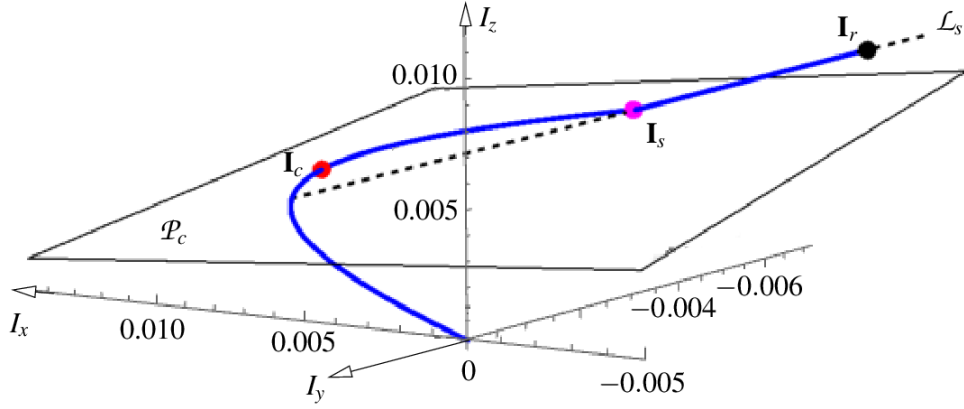


Figure 2.6: Impulse curve for the icosahedron-tetrahedron impact, with the plane of compression  $\mathcal{P}_c$  and the line of sticking  $\mathcal{L}_s$ .

### 2.5.2 Resumed Slip

Resumed sliding mode happens when  $\|B^{-1}\mathbf{d}\| > \mu$ . At  $I_z = I_{zs}$ , the tangential velocity curve  $\gamma$  will grow in some direction  $\hat{\mathbf{s}} = (\cos \phi, \sin \phi)^T$  after passing origin. This direction must agree with the acceleration direction  $\gamma'$ . Thus,  $\gamma'_{yz} = -\mu B\hat{\mathbf{s}} + \mathbf{d}$  must be satisfied according to (2.27) with  $\hat{\gamma} = \hat{\mathbf{s}}$ . Thus, initially the resumed sliding direction must be centrifugal, and also this direction will be maintained. Follow from Theorem 5(iv), one obtains the following corollary.

**Corollary 6** *Suppose  $\|B^{-1}\mathbf{d}\| > \mu$ . Once the sliding velocity  $\gamma_{yz}$  reaches zero, sliding will continue in the unique centrifugal direction.*

Fig. 2.8 shows an example of resumed sliding from the modified instance of the icosahedron-tetrahedron impact. The velocity decreases to zero first, then resume sliding continue compression. Then till the end and finish compression. Fig. 2.9 shows a bundle of curves with  $\gamma^-$  at a unit circle. In this configuration, there is one centrifugal and one centripetal direction. The curves all try to go to the centrifugal direction. Six of them,  $\gamma_i$ ,  $1 \leq i \leq 6$  reach it.  $\gamma_3$  reaches the origin before continuing in the centrifugal direction.  $\gamma_6$  starts in the centrifugal direction and follows the centrifugal direction as a straight line segment;  $\gamma_1$ ,  $\gamma_4$ , and  $\gamma_5$  reach

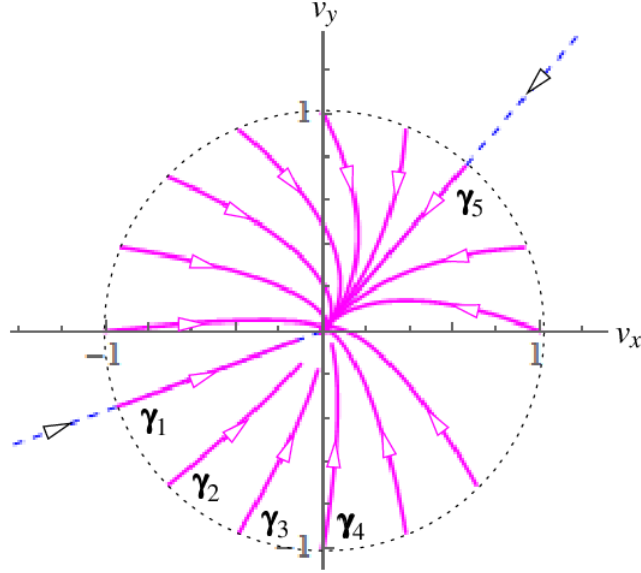


Figure 2.7: Bundle of 15 hodographs resulting from unit  $\gamma^-$  values for the icosahedron-tetrahedron collision ( $\mu = 0.8$  and  $v_z = -0.2$ ).

the direction but not the origin;  $\gamma_2$  starts in the centripetal direction, reaches the origin, and goes to the centrifugal direction.

To compute this unique centrifugal invariant  $\hat{\mathbf{s}}$ , we first verify if  $\hat{\mathbf{s}} = (-1, 0)^T$ . Then, let  $\hat{\mathbf{s}} = ((1 - \eta^2)/(1 + \eta^2), 2\eta/(1 + \eta^2))^T$  from  $(-\infty, \infty)$  to the set of all unit vectors except  $(-1, 0)^T$ . Plug into (2.29) then get a quartic polynomial equation in  $\eta$ , which has roots in analytical forms. The centrifugal direction is the unique  $\hat{\mathbf{s}}$  that satisfies  $\hat{\mathbf{s}}^T(-\mu B \hat{\mathbf{s}} + \mathbf{d}) > 0$ .

After resumed sliding starts, the tangential impulse  $\mathbf{I}_\perp$  will be accumulating along a constant direction. To compute it, one can let  $-\mu B \hat{\mathbf{s}} + \mathbf{d} = \lambda \hat{\mathbf{s}}$  for some  $\lambda > 0$ . Thus,  $\gamma' = \lambda \hat{\mathbf{s}}$  by (2.27) and  $\mathbf{I}' = \hat{\mathbf{z}} + (\hat{\mathbf{x}}, \hat{\mathbf{y}}) B^{-1}(\lambda \hat{\mathbf{s}} - \mathbf{d})$  by (2.24).

There is probably no way of determining  $I_{zs}$  in general without integrating the differential equation (2.27). But once we know the value  $I_z = I_{zs}$  at which  $\gamma$  will become zero, the impulse accumulation will start to take a linear form in  $I_z$ .

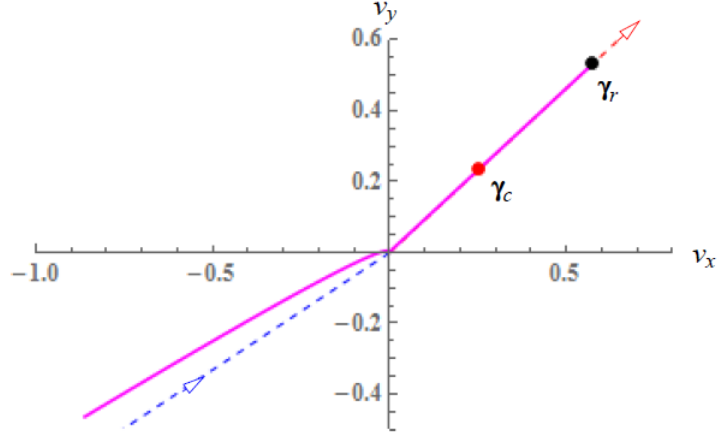


Figure 2.8: Hodograph of the impact instance in Fig. 2.3 with the following changed parameter values:  $\mu = 0.25$  and  $\mathbf{V}_1^- = (-0.7, -0.35, -0.5)^T$ .

## 2.6 Solution of the Impact Problem

The whole system will be initiated and driven by the normal impulse  $I_z$ . At the beginning,  $I_z = 0$ , then slightly increase it to start the whole process. Other values such like  $\mathbf{I}$  and energy, can be computed via differential relationship with respect to  $I_z$ , such as (2.27), (2.23) and (2.10).

**Theorem 7** *Given the impact configuration for two bodies  $\mathcal{B}_1$  and  $\mathcal{B}_2$ , and their inertia properties, the total impulse  $\mathbf{I}_r$  (and therefore the changes in their velocities according to (4.1)) depend on the pre-impact contact velocity  $\mathbf{v}^-$  not on individual pre-impact velocities.*

**Proof** The inverse inertia matrix  $W$  defined in (2.5) is determined by the impact configuration and the bodies' inertia properties, so are the matrix  $B$  in (2.18) and the vector  $\mathbf{d}$  in (2.19) which governs the evolution of the sliding velocity  $\boldsymbol{\gamma}$  in (2.27). During the impact, the impulse  $\mathbf{I}$  is evaluated based on  $\boldsymbol{\gamma}$  and the normal impulse  $I_z$  according to (2.23). When the contact slides,  $\boldsymbol{\gamma}$  evolves according to (2.27) which has a unique solution in terms of  $I_z$ . When the contact sticks, the impulse  $\mathbf{I}$  has a simplified form (2.31) in terms of  $I_z$ . Slip or stick is initialized with  $\mathbf{v}^-$ , and determined by checking if  $\boldsymbol{\gamma} = \mathbf{0}$ , and, if true, by further checking if  $\|B^{-1}\mathbf{d}\| \leq \mu$ . In summary, the growth in  $\mathbf{I}$  is completely determined by the impact configuration.



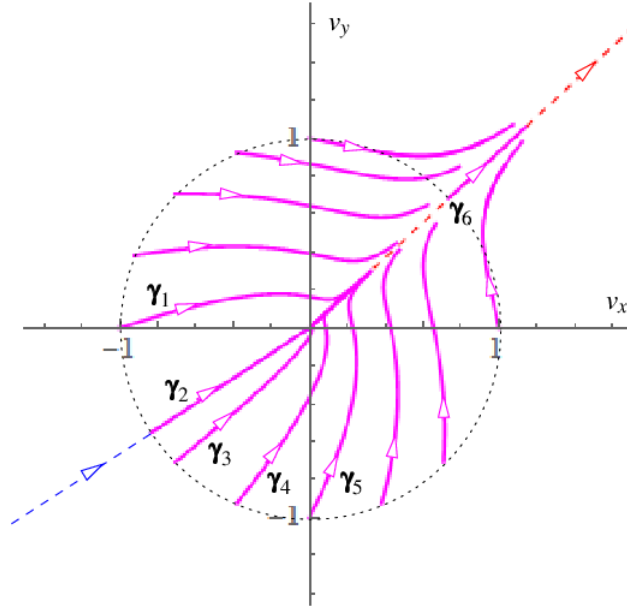


Figure 2.9: Bundle of 13 hodographs resulting from unit  $\gamma_{yz}^-$  values for the icosahedron-tetrahedron collision ( $\mu = 0.5$  and  $v_z = -0.8$ ).

Meanwhile, the potential energy  $E$  at the contact, evolving under (2.10), completely depends on  $\mathbf{I}$  and  $v_z^-$ . So are the ends of compression ( $E' = 0$ ) and restitution ( $E = 0$ ). Thus, the value of  $\mathbf{I}_r$  at the end of restitution is determined.  $\square$

Section 2.6.1 will introduce how we speed up the numerical integration process. We will discuss situations when closed form solution can be applied to directly get the total impulse from the point: a)  $\boldsymbol{\gamma} = \mathbf{0}$  and b)  $\boldsymbol{\gamma} \times (-\mu B \hat{\boldsymbol{\gamma}} + \mathbf{d}) = \mathbf{0}$ . In case a), it is the vanishing of sliding velocity, so either sticking will happen start from that point or resumed sliding will happen. This will be introduced in Section 2.6.2. b) is straight sliding, which is when the tangential velocity curve touches invariant direction, which will be introduced in Section 2.6.3.

### 2.6.1 Fast Numerical Integration

Equation (2.27) usually does not have closed form solution, unless when  $\boldsymbol{\gamma} = \mathbf{0}$  or  $\boldsymbol{\gamma} \times (-\mu B \hat{\boldsymbol{\gamma}} + \mathbf{d}) = \mathbf{0}$  happens. So numerical integration is used until closed form can be applied. To speed up the integration process, we propose to adjust the step size of  $I_z$  based on the speed

of curve  $\|\gamma'\|$  and absolute curvature  $|\kappa|$  of the hodograph.

1. Consider constant increment in the arc length  $h_1$ , then  $I_z$  would follow step size of  $h_1/\|\gamma'\|$ .
2. Consider constant increment in the tangential angle  $h_2$ , then  $I_z$  would follow a step size of  $h_2/(|\kappa|\|\gamma'\|)$ . Adjust the arc length increment  $\Delta s$  as  $h_2/|\kappa|$ .

Combining the above two factors, we set the step size as below:

$$\epsilon \frac{h_1}{\|\gamma'\|} + (1 - \epsilon) \frac{h_2}{|\kappa|\|\gamma'\|}, \quad \text{for } 0 < \epsilon < 1. \quad (2.32)$$

From (2.27), the curvature is

$$\begin{aligned} \kappa &= \frac{\gamma' \times \gamma''}{\|\gamma'\|^3} \\ &= \frac{(-\mu B \hat{\gamma} + \mathbf{d}) \times \left[ -\mu B \hat{\gamma} \times \left( (-\mu B \hat{\gamma} + \mathbf{d}) \times \hat{\gamma} \right) \right]}{\|\gamma'\| \cdot \|\mathbf{d} - \mu B \hat{\gamma}\|^3}. \end{aligned} \quad (2.33)$$

When  $|\kappa|$  is large, the curve is more curly, so the first term dominates the second. Vice versa.  $\epsilon$  in (2.32) can be fixed or adjusted dynamically during the numerical integration. A part of the sliding velocity curve applying the curvature based step size is seen in Fig. 2.10.

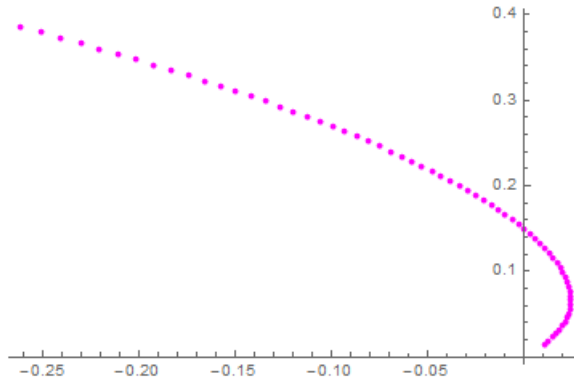


Figure 2.10: Curvature based step size for numerical integration.

### 2.6.2 Sliding Velocity at Zero

As impulse  $I_z$  grows, if  $\boldsymbol{\gamma} \times (-\mu B \hat{\boldsymbol{\gamma}} + \mathbf{d})$  becomes zero before  $\boldsymbol{\gamma}$  becomes zero, besides (2.11), then mark the values:

$$\begin{aligned} I_{zs} : & \quad \text{smallest value of } I_z \text{ at which } \boldsymbol{\gamma} = \mathbf{0} \text{ and,} \\ & \quad \text{for } I_z < I_{zs}, \boldsymbol{\gamma} \times (-\mu B \hat{\boldsymbol{\gamma}} + \mathbf{d}) \neq \mathbf{0}; \\ \mathbf{I}_s : & \quad \text{value of } \mathbf{I} \text{ when } I_z = I_{zs}; \\ E_s : & \quad \text{value of } E \text{ when } I_z = I_{zs}. \end{aligned}$$

First, plug in  $\boldsymbol{\gamma} = \mathbf{0}$  and  $I_z = I_{zs}$  into (2.23) to get the value of  $\mathbf{I}_s$  from numerical integration. Next, combine (2.24) for sticking and (2.26) for resumed sliding into one equation:  $\mathbf{I}' = \boldsymbol{\sigma}$ , where

$$\boldsymbol{\sigma} = \begin{cases} \hat{\mathbf{z}} - (\hat{\mathbf{x}} \hat{\mathbf{y}}) B^{-1} \mathbf{d}, & \text{if } \|B^{-1} \mathbf{d}\| \leq \mu \text{ (sticking);} \\ \hat{\mathbf{z}} - \mu (\hat{\mathbf{x}} \hat{\mathbf{y}}) \hat{\mathbf{s}}, & \text{if } \|B^{-1} \mathbf{d}\| > \mu \text{ (resumed sliding).} \end{cases} \quad (2.34)$$

The impulse now is:

$$\mathbf{I} = \mathbf{I}_s + (I_z - I_{zs}) \boldsymbol{\sigma}, \quad \text{for } I_z \geq I_{zs}, \quad (2.35)$$

with the ending value  $\mathbf{I}_r = \mathbf{I}_s + (I_{zr} - I_{zs}) \boldsymbol{\sigma}$ . We need to determine the normal impulse value  $I_{zr}$  at the end of restitution.

$E_s$  at  $I_{zs}$  is recorded. To find out if  $I_{zs} < I_{zc}$ , one can check the sign of energy derivative. For  $I_z \geq I_{zs}$ , we plug (2.35) into (2.10) to obtain:

$$\begin{aligned} E' &= -v_z^- - \left( \frac{1}{m_1} + \frac{1}{m_2} \right) I_z + \hat{\mathbf{z}}^T S \left( \mathbf{I}_s + (I_z - I_{zs}) \boldsymbol{\sigma} \right) \\ &= -v_z^- + \hat{\mathbf{z}}^T S (\mathbf{I}_s - I_{zs} \boldsymbol{\sigma}) - \frac{1}{m_\sigma} I_z, \end{aligned} \quad (2.36)$$

where  $m_\sigma = \left( \frac{1}{m_1} + \frac{1}{m_2} - \hat{\mathbf{z}}^T S \boldsymbol{\sigma} \right)^{-1}$ . Integrate the above:

$$\Phi_1(I_z) \equiv \left( -v_z^- + \hat{\mathbf{z}}^T S (\mathbf{I}_s - I_{zs} \boldsymbol{\sigma}) \right) I_z - \frac{1}{2m_\sigma} I_z^2. \quad (2.37)$$

Two cases below arise.

**Case 1** Compression has not ended by  $I_z = I_{zs}$ . Example hodographs are shown in Figs. 2.5(d) and 2.8. Solving the equation  $E' = 0$  via a substitution of (2.36), we first obtain  $I_{zc} =$

$m_\sigma \left( -v_z^- + \hat{\mathbf{z}}^T S(\mathbf{I}_s - I_{zs}\boldsymbol{\sigma}) \right)$ . The maximum energy (achieved at the end of compression) is  $E_c = E_s + \Phi_1(I_{zc}) - \Phi_1(I_{zs})$ . During restitution, the energy takes the form  $E = e^2 E_c + \Phi_1(I_z) - \Phi_1(I_{zc})$ . Letting  $E = 0$  and substituting (2.37) in, we end up with a quadratic equation:  $a_2 I_z^2 + a_1 I_z + a_0 = 0$ , where  $a_2 = -\frac{1}{2m_\sigma}$ ,  $a_1 = -v_z^- + \hat{\mathbf{z}}^T S(\mathbf{I}_s - I_{zs}\boldsymbol{\sigma})$ , and  $a_0 = e^2 E_c - \Phi_1(I_{zc})$ . Then,  $I_{zr}$  is the smallest root greater than  $I_{zc}$ .

**Case 2** Compression has ended by  $I_z = I_{zs}$ . An example is Fig. 2.5(a). Since it is during restitution, the energy has the form  $E = E_s + \Phi_1(I_z) - \Phi_1(I_{zs})$ , for  $I_z \geq I_{zs}$ .

Vanishing of  $E$  yields the quadratic equation  $a_2 I_z^2 + a_1 I_z + b_0 = 0$ , where  $b_0 = E_s - \Phi_1(I_{zs})$ . Solve the equation to obtain  $I_{zr}$  as the smallest root greater than  $I_{zs}$ .

### 2.6.3 Start of Straight Sliding

Suppose that  $\boldsymbol{\gamma} \times (-\mu B \hat{\boldsymbol{\gamma}} + \mathbf{d})$  becoming zero happens before  $\boldsymbol{\gamma} = \mathbf{0}$  as  $I_z$  increases from zero. Denote:

$$\begin{aligned} I_{zl} : & \quad \text{smallest value of } I_z \text{ at which } \boldsymbol{\gamma} \times (-\mu B \hat{\boldsymbol{\gamma}} + \mathbf{d}) = \mathbf{0} \text{ and,} \\ & \quad \text{for } I_z \leq I_{zl}, \boldsymbol{\gamma} \neq \mathbf{0}; \\ \mathbf{I}_l : & \quad \text{value of } \mathbf{I} \text{ when } I_z = I_{zl}; \\ E_l : & \quad \text{value of } E \text{ when } I_z = I_{zl}. \end{aligned}$$

At  $I_{zl}$ , let  $\boldsymbol{\gamma}_l$  be the value of  $\boldsymbol{\gamma}$ . Let  $\lambda$  be some value such that  $\boldsymbol{\gamma}' = \lambda \hat{\boldsymbol{\gamma}}_l$  holds. From (2.28) the corresponding normal impulse  $I_{zs} = I_{zl} + \Delta I_z$  when  $\boldsymbol{\gamma}$  is to become zero before impact finishes, where

$$\Delta I_z = \begin{cases} -\|\boldsymbol{\gamma}_l\|/\lambda, & \text{if } \lambda < 0, \text{ i.e., } \hat{\boldsymbol{\gamma}}_l \text{ is centripetal,} \\ \infty, & \text{otherwise.} \end{cases} \quad (2.38)$$

Meanwhile, integrating (2.26),

$$\mathbf{I} = \mathbf{I}_l + (I_z - I_{zl})\boldsymbol{\delta}, \quad (2.39)$$

where

$$\boldsymbol{\delta} = \hat{\mathbf{z}} - \mu(\hat{\mathbf{x}}, \hat{\mathbf{y}})\hat{\boldsymbol{\gamma}}_l. \quad (2.40)$$

Plug (2.39) into (2.10):

$$E' = -v_z^- + \hat{\mathbf{z}}^T S(\mathbf{I}_l - I_{zl}\boldsymbol{\delta}) - \frac{1}{m_\delta} I_z, \quad (2.41)$$

where  $m_\delta = (\frac{1}{m_1} + \frac{1}{m_2} - \hat{\mathbf{z}}^T S\boldsymbol{\delta})^{-1}$ , and integrate:

$$\Phi_2(I_z) = \left(-v_z^- + \hat{\mathbf{z}}^T S(\mathbf{I}_l - I_{zl}\boldsymbol{\delta})\right) I_z - \frac{1}{2m_\delta} I_z^2. \quad (2.42)$$

If compression has not ended by  $I_z = I_{zl}$ , solve normal impulse  $\zeta_c = m_\delta \left(-v_z^- + \hat{\mathbf{z}}^T S(\mathbf{I}_l - I_{zl}\boldsymbol{\delta})\right)$  from  $E' = 0$  to get the value when compression would end still having  $\gamma \neq \mathbf{0}$ . There are two cases for comparing  $I_{zs}$  with  $\zeta_c$ .

**Case 1** ( $I_{zs} \leq \zeta_c$ ) In this case,  $\gamma$  will have decreased to  $\mathbf{0}$  by the end of compression. An example instance is shown in Fig. 2.5(b). Set  $E_s = \Phi_2(I_{zs})$ , and

$$\mathbf{I}_s = \mathbf{I}_l + (I_{zs} - I_{zl})\boldsymbol{\delta}. \quad (2.43)$$

Transition into Case 1 in Section 2.6.2 to determine  $\mathbf{I}_r$ .

**Case 2** ( $I_{zs} > \zeta_c$ ) In this case, sliding will continue into restitution. Set  $I_{zc} = \zeta_c$  and  $E_c = E_l + \Phi_2(I_{zc}) - \Phi_2(I_{zl})$ . During restitution and before  $\gamma$  becomes zero, the energy is  $E = e^2 E_c + \Phi_2(I_z) - \Phi_2(I_{zc})$ . Again, by setting  $E = 0$  we end up with a quadratic equation:

$$-\frac{1}{2m_\delta} I_z^2 + \left(-v_z^- + \hat{\mathbf{z}}^T S(\mathbf{I}_l - I_{zl}\boldsymbol{\delta})\right) I_z + e^2 E_c - \Phi_2(I_{zc}) = 0. \quad (2.44)$$

Let  $\zeta_e$  be the smallest root greater than  $\zeta_c$ . This is the value of  $I_z$  at the end of restitution if sliding lasts until then. There are two further subcases:

**Case 2a** ( $I_{zs} \leq \zeta_e$ ) Here,  $\gamma$  will have reached zero by the end of restitution, as with the instance in Fig. 2.12(a). Let  $E_s = e^2 E_c + \Phi_2(I_{zs}) - \Phi_2(I_{zc})$  and set  $\mathbf{I}_s$  according to (2.43). Transition into Case 2 in Section 2.6.2 to determine  $\mathbf{I}_r$ .

**Case 2b** ( $I_{zs} > \zeta_e$ ) The sliding velocity will never decrease to zero. Fig. 2.12(b) shows an example. We let  $I_{zr} = \zeta_e$  and  $\mathbf{I}_r = \mathbf{I}_l + (\zeta_e - I_{zl})\boldsymbol{\delta}$ .

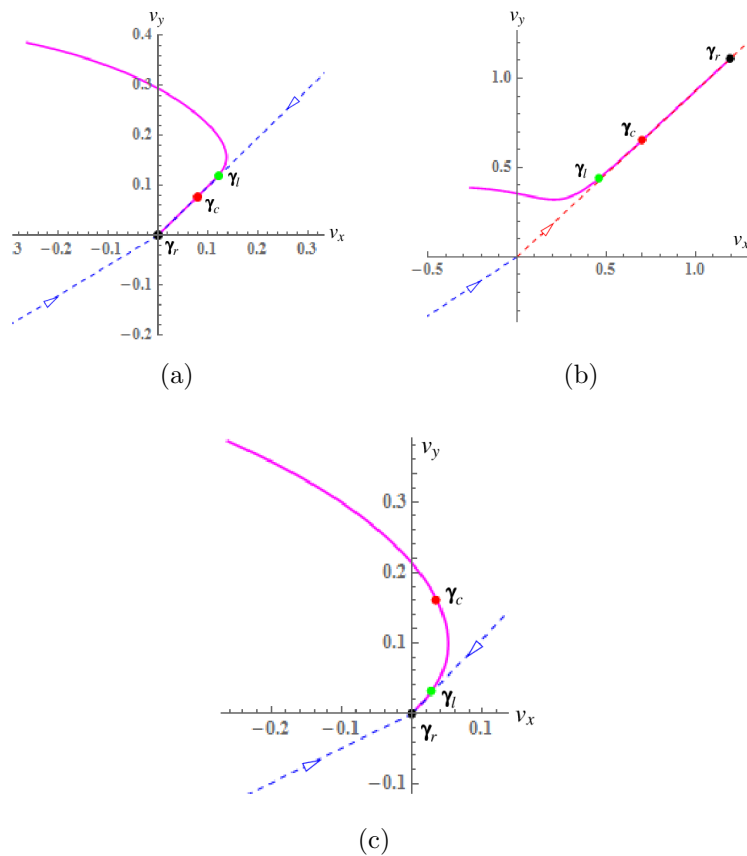


Figure 2.12: Hodographs of the icosahedron-tetrahedron impact in Fig. 2.3 with the following changed parameter values: (a)  $\mu = 0.35$  and  $V_{1z}^- = 0.2$ ; (b)  $\mu = 0.25$  and  $V_{1z}^- = -1$ ; and (c)  $\mu = 0.55$  and  $V_{1z}^- = 0.9$ .

If compression has ended by the moment  $I_z = I_{zl}$ ,  $E = E_l + \Phi_2(I_z) - \Phi_2(I_{zl})$  for  $I_z \geq I_{zl}$ . Let  $E = 0$  and plug (2.42) in, we get a quadratic equation:

$$-\frac{1}{2m_\delta}I_z^2 + \left(-v_z^- + \hat{z}^T S(\mathbf{I}_l - I_{zl}\boldsymbol{\delta})\right)I_z + E_l - \Phi_2(I_{zl}) = 0 \quad (2.45)$$

Solve the above equation for  $\zeta_e$ , which is the smallest root greater than  $I_{zc}$ . There are two cases:

**Case 3** ( $I_{zs} < \zeta_e$ ) Here,  $\gamma$  will become zero before restitution ends, as with the impact instance in Fig. 2.12(c). Let  $E_s = E_l + \Phi_2(I_{zs}) - \Phi_2(I_{zl})$  and set  $\mathbf{I}_s$  according to (2.43). Transition into Case 2 in Section 2.6.2 to determine  $\mathbf{I}_r$ .

**Case 4** ( $I_{zs} \geq \zeta_e$ ) The sliding velocity will never decrease to zero, as with the impact instance in Fig. 2.5(c). Handle the case exactly like Case 2b.

A more clear understanding of all the seven cases from Section 2.6.1 and Section 2.6.3 can be seen in Fig. 2.13, Fig. 2.14 and Fig. 2.15 together with some simulation examples.

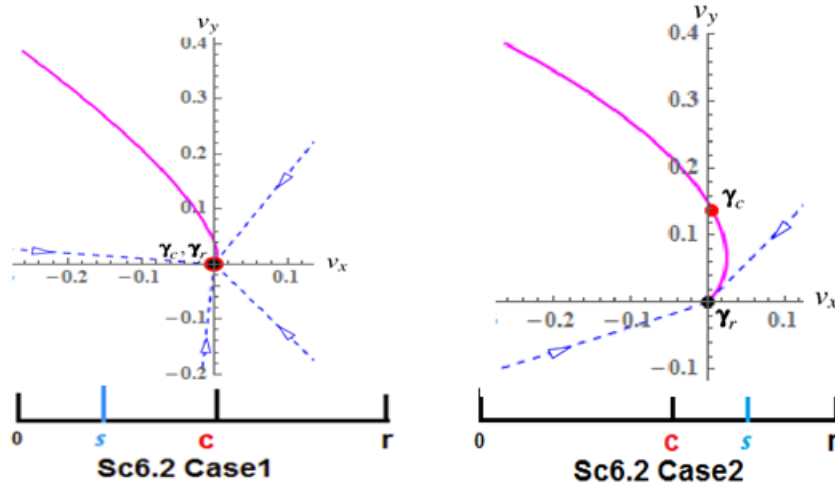


Figure 2.13: Part of seven cases with simulation examples.

The axis underneath each graph shows the growing of normal impulse, the blue "s" implies the vanishing of sliding velocity, and green "l" shows the starting of straight sliding. The seven cases corresponds to the relationships among all these values.

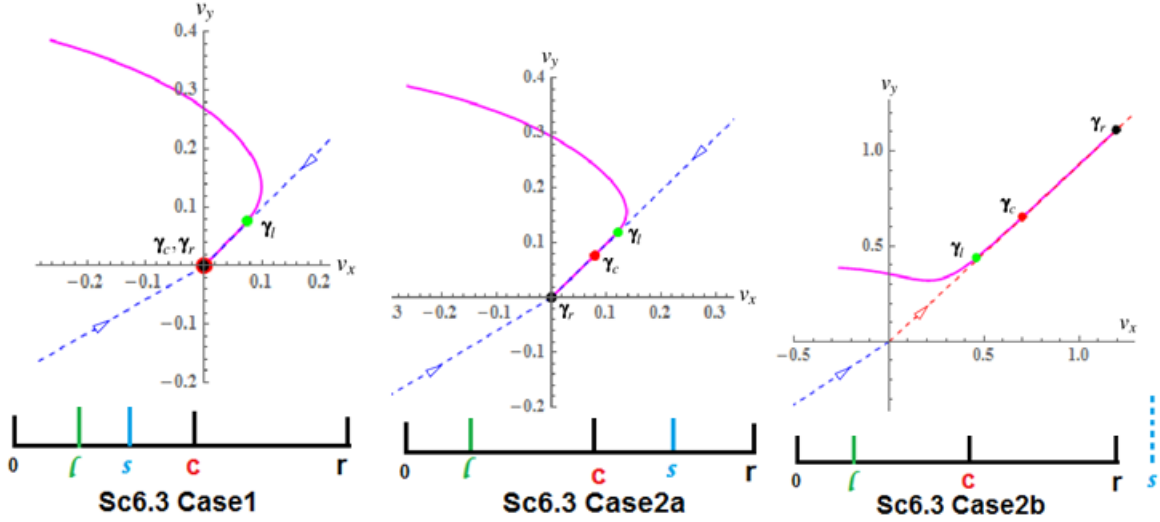


Figure 2.14: Part of seven cases with simulation examples.

#### 2.6.4 Impact Algorithm and Execution Examples

The computation of  $\mathbf{I}_r$  is shown in Algorithm 1. Lines 4–14 performs numerical integration of (2.27) to track the sliding velocity  $\gamma$ . Lines 20–22 is when  $\gamma$  reaches zero along a curved trajectory. Lines 24–30 is when straight sliding starts before  $\gamma = 0$  happens.

We compute Fig. 2.3 with the pre-impact velocities (2.13), and another impact between a bowling pin and a bowling ball using this impact algorithm. The bowling example having its configuration specified in Fig. 2.16, and it has the inverse inertia matrix

$$W = \begin{pmatrix} 1.55465 & 0.00238675 & -0.360808 \\ 0.00238676 & 5.15191 & -0.00313296 \\ -0.360808 & -0.00313296 & 1.105 \end{pmatrix}.$$

The pre-impact velocities are

$$\begin{aligned} \mathbf{V}_1^- &= (-0.1, 0.2, -0.5)^T, & \boldsymbol{\omega}_1^- &= (0.1, 0.1, 0.1)^T, \\ \mathbf{V}_2^- &= (0.1, 0.1, 1)^T, & \boldsymbol{\omega}_2^- &= (0.1, -0.1, 0.1)^T. \end{aligned}$$

The “true value” of  $\mathbf{I}_r$  was computed using numerical integration with very small step size until closed-form evaluation. They are given in (2.14) for the icosahedron-tetrahedron impact and as  $(0.7330654, -0.0216048, 2.585018)^T$  for the pin-ball impact. We also compare it with



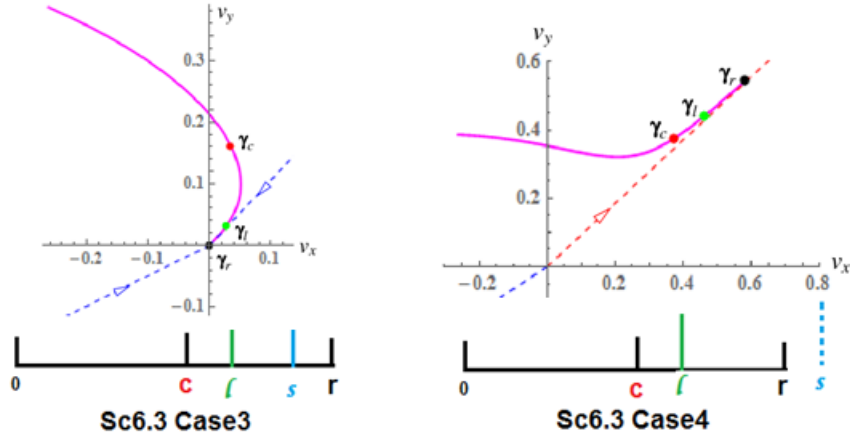


Figure 2.15: Part of seven cases with simulation examples.

three other different solutions: numerical integration all the way (NI) as shown in previous works; Fixed step size of the normal impulse in integration (FS); curvature based adjustable integration step size (2.32) (VS) with  $\epsilon = 0.5$  and  $h_1 = h_2 = 0.01$ . The error is defined as the norm of the difference between its obtained value of  $I_r$  and the “true value”.

The code is written in Mathematica 10.3 and executed on a Lenovo Thinkpad X230i with Intel Core i3-3120M Processors and 4 GB system RAM. Table 2.1 shows the results. For the

Table 2.1: Impact computation comparison among pure numerical integration (NI), integration with fixed step size coupled with closed-form evaluation (FS), and integration with adjustable size coupled with close-form evaluation (VS).

	Icosa-Tetra			
	“Truth”	NI	FS	VS
#Step size	1E-6	0.00095	0.001	—
#Iter.	68212	107	69	<b>29</b>
Time (s)	18.9697	0.0312002	0.000624	<b>0.0004134</b>
Error	—	0.000877	0.00108669	<b>0.00111229</b>
	Pin-Ball			
	“Truth”	NI	FS	VS
#Step size	1E-6	0.001000	0.002	—
#Iter.	165073	2586	83	<b>29</b>
Time (s)	46.9563	0.265200	0.0009360	<b>0.0004006</b>
Error	—	0.001430	6.04690E-5	<b>5.70441E-5</b>

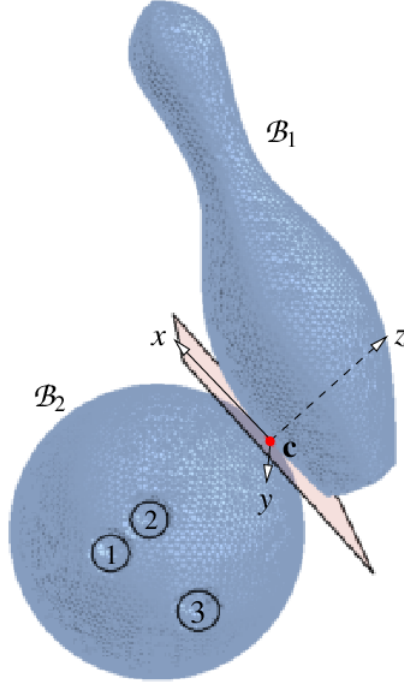


Figure 2.16: Configuration of impact ( $\mu = 0.7$  and  $e = 0.7$ ) between a bowling pin ( $\mathcal{B}_1$ ) and a ball ( $\mathcal{B}_2$ ), both with uniform mass distribution. Here,  $\mathbf{o}_1 = (0.068436, -0.00000242, 0.073735)^T$ ,  $\mathbf{o}_2 = (-0.000061, -0.000890, -0.108458)^T$ ,  $m_1 = 1.63293$ ,  $m_2 = 6.35029$ ,  $Q_1 = \text{diag}(0.0021186, 0.012092, 0.014029)^T$ , and  $Q_2 = \text{diag}(0.0295723, 0.029669, 0.030068)^T$ . The shape of the pin is specified in Lab (2016). The pin is originally symmetric about the  $z$ -axis with its center of mass at the origin. To engage in contact, it rotates about the  $y$ -axis through  $\tan^{-1}(3.15435)$  and then translates by  $(0.068436, 0, 0.073735)^T$ . The ball has radius 0.108458. Its three holes are each created from subtracting a cylinder parallel to the  $y$ -axis. Holes 1 and 2 each has radius 0.0127, while hole 3 has radius 0.0142875. The bottom faces of the three cylinders are centered respectively at  $(0.03302, 0.067845, -0.126238)^T$ ,  $(0.03302, 0.067845, -0.090678)^T$ , and  $(-0.0381, 0.0676971, -0.108458)^T$ .

icosahedron-tetrahedron impact example, NI, FS, VS give comparable errors. VS is 75 times faster than NI and 2 times faster than FS. For the pin-ball impact example, VS is 25 times more accurate than NI in 1/662nd of time. It is also more than two times faster than FS with slightly higher accuracy.

---

**Algorithm 1** Impulse Computation
 

---

```

1: evaluate  $\mathbf{v}^-$  according to (4.2)
2:  $\mathbf{I} \leftarrow \mathbf{0}$ 
3: evaluate  $B$  and  $\mathbf{d}$  according to (2.18) and (2.19)
4: while ( $E \neq 0$  or  $I_z = 0$ ) and  $\boldsymbol{\gamma} \neq \mathbf{0}$  and  $\boldsymbol{\gamma} \times (-\mu B \hat{\boldsymbol{\gamma}} + \mathbf{d}) \neq \mathbf{0}$  do
5:   update  $\boldsymbol{\gamma}$  via one-step integration of (2.27) over  $I_z$ 
6:   update  $\mathbf{I}$  according to (2.23)
7:   update  $v_z$  according to (2.7)
8:   update  $E$  via one-step numerical integration of (2.10)
9:   if  $v_z = 0$  (compression ends) then
10:      $I_{zc} \leftarrow I_z$ 
11:      $E_c \leftarrow E$ 
12:      $E \leftarrow e^2 E$ 
13:   end if
14: end while
15: if  $E = 0$  then
16:   return  $\mathbf{I}$ 
17: else
18:   set  $\boldsymbol{\sigma}$  according to (4.6)
19:   if  $\boldsymbol{\gamma} = \mathbf{0}$  then
20:      $\mathbf{I}_s \leftarrow I_z \hat{\mathbf{z}} - (\hat{\mathbf{x}}, \hat{\mathbf{y}}) B^{-1} (\boldsymbol{\gamma}^- + I_z \mathbf{d})$ 
21:     determine  $I_{zr}$  as in Section 2.6.2
22:     return  $\mathbf{I}_s + (I_{zr} - I_{zs}) \boldsymbol{\sigma}$ 
23:   else
24:     determine  $I_{zs}$ ,  $\mathbf{I}_s$  (if needed) and  $I_{zr}$  as in Section 2.6.3
25:     if  $\boldsymbol{\gamma}$  reaches zero then
26:       return  $\mathbf{I}_s + (I_{zr} - I_{zs}) \boldsymbol{\sigma}$ 
27:     else
28:       set  $\boldsymbol{\delta}$  according to (4.5)
29:       return  $\mathbf{I}_l + (I_{zr} - I_{zl}) \boldsymbol{\delta}$ 
30:     end if
31:   end if
32: end if

```

---

## CHAPTER 3. COMPUTATIONAL MODELING OF $N$ -BODY COLLISIONS WITH SIMULATION AND EXPERIMENT

Multi-body collision is a common phenomenon that takes place when several objects collide together, as observed in the games of marbles, billiards, and bowling. To make the robot purposefully take advantage of impact to become better at certain tasks, a general and computationally efficient model is needed for predicting the outcome of an  $n$ -body collision.

Impact occurs over a short period of time, generating a very large interaction force. Analysis is done in terms of impulse, the integral of force over time, which equals the finite change in momentum. In the past, little work has been done on impulsive manipulation. Noticeable results include Huang and Mason (2000a), Tagawa et al. (2010), Hirai et al. (1999a) and Wang et al. (1992). Recent work by the third author Jia et al. (2012) modeled contacts during a multi-body collision as virtual springs, and described the entire process as a diagram showing different periods that transition into one and another. This model in theory can be extended to predict the outcome of collision with any numbers of bodies involved, when combined with his study Jia (2012a) of tangential impulse under compliance. However, a general framework and related computational issues still need to be worked out.

### 3.1 Introduction

In this paper, we will introduce an  $n$ -body impulse-based collision model that works with or without friction. The model can be used to determine the post-collision motions of any number of objects engaged in the collision. We will focus on the case where the centers of mass of the objects engaged in the collision are coplanar. At the conclusion of the paper, we will discuss how the model can be readily extended to a general collision configuration.

Section 3.2 adopts the idea from Jia et al. (2012), which focused on three-body impact only, to set up a system for frictionless collisions of  $n$  balls. Angular velocities are not considered for the moment. During a collision process, impulses and energies at various contacts are tracked via numerical integration based on their differential relationships to the dominant impulse, which switches from one period to another. To initialize the impulse derivatives, instead of using wave propagation Liu et al. (2008) and Liu et al. (2009), we set up a system of equations and solve it numerically using Newton’s method. This avoids a tedious analysis that enumerates all possible topologies of active contacts during the collision. An energetic coefficient of restitution Stronge (2004a) is employed for tracking the energy loss.

The above model is used to simulate Newton’s cradle, in which no rotation is involved and friction between the balls is negligible. The apparatus has been studied earlier Ceanga and Hurmuzlu (2001); Acary and Brogliato (2003) by considering coupling effects via the use of an impulse correlation ratio.

Section 3.3 considers friction and the angular velocities of  $n$  rigid objects with arbitrary shapes involved in the collision. Tangential impulse, now existing at every contact, has to be determined. This requires an analysis of the sticking and sliding modes under Coulomb’s law of friction, by solving a system in terms of contact velocities. This allows us to determine the relationship between tangential impulse and normal impulse at the same contact.

In Section 3.4, we first conduct simulation and experiment on Newton’s cradle to validate the  $n$ -body collisions model in the frictionless case. Next, we present a simulation of nine-ball break shots based on the implementation of our model in the frictional case, which gives realistic outcomes.

The final section offers a brief summary of the paper, along with some future work to improve the efficiency and further validate the model’s accuracy.

### 3.2 Frictionless Collision of Translating Balls

In this section, we investigate a frictionless collision among  $n$  translating balls whose centers of mass are co-planar, and describe an algorithm to compute the collision outcome. In the next section, the model will be extended to objects with arbitrary geometry, angular velocities, and

contact friction. Later in this section, the model is then applied to solve the classical problem of Newton's Cradle.

### 3.2.1 Impact dynamics and contact kinematics

Suppose that  $n$  rigid balls  $\mathcal{B}_1, \dots, \mathcal{B}_n$  are engaged in a collision. Let  $\mathbf{v}_i$  be the velocity of  $\mathcal{B}_i$ ,  $\mathbf{I}_{ij}$  the impulse that  $\mathcal{B}_i$  receives from  $\mathcal{B}_j$ . By Newton's third law,  $\mathbf{I}_{ij} = -\mathbf{I}_{ji}$ . For  $1 \leq i \leq n$ , denote  $\mathbb{C}_i$  as the set of subscripts of the objects that are in contact with  $\mathcal{B}_i$ , which has initial velocity  $\mathbf{v}_i^{(0)}$ . Then the velocity of  $\mathcal{B}_i$  during the collision changes as follows:

$$\mathbf{v}_i = \mathbf{v}_i^{(0)} + \frac{1}{m_i} \sum_{k \in \mathbb{C}_i} \mathbf{I}_{ik}, \quad i = 1, 2, \dots, n. \quad (3.1)$$

For every two balls  $\mathcal{B}_i$  and  $\mathcal{B}_j$  in contact, we add a virtual spring  $\{i, j\}$  at the contact point. Without ambiguity, we will also refer to the contact by the same notation  $\{i, j\}$ . This spring is along the contacting normal which is perpendicular to their common tangent plane. Fig. 3.1 shows the ball  $\mathcal{B}_i$  with the contact set  $\mathbb{C}_i = \{j_1, j_2, j_3\}$ . Impulsive forces on the balls

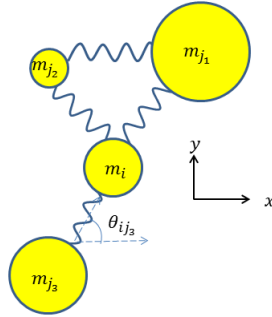


Figure 3.1: Contact modeling with virtual springs.

are much larger than the gravitational forces, which can be ignored consequently. Reorient the system such that all the balls lie on a horizontal plane. For the spring  $\{i, j\}$ , let  $\theta_{ij}$  be the angle from the  $x$ -axis to the spring direction vector, which points from  $\mathcal{B}_j$  to  $\mathcal{B}_i$  if  $j > i$ , and in the opposite direction otherwise. Thus, the unit normal vector  $\hat{\mathbf{n}}_{ij} = (\cos \theta_{ij}, \sin \theta_{ij})$  always points from the ball with the bigger subscript to the ball with the smaller one. We let  $\mathbf{I}_{ij} = \sigma_{ij} \|\mathbf{I}_{ij}\|$ ,

where

$$\sigma_{ij} = \begin{cases} 1 & \text{if } i < j, \\ -1 & \text{if } i > j. \end{cases}$$

The velocity components of ball  $\mathcal{B}_i$  during impact can then be written as:

$$\begin{pmatrix} v_{ix} \\ v_{iy} \end{pmatrix} = \begin{pmatrix} v_{ix}^{(0)} \\ v_{iy}^{(0)} \end{pmatrix} + \frac{1}{m_i} \sum_{k \in \mathbb{C}_i} \begin{pmatrix} I_{ik} \cos \theta_{ik} \\ I_{ik} \sin \theta_{ik} \end{pmatrix}. \quad (3.2)$$

Denote  $\mathbb{P}$  as the set of contacts, and  $\tilde{v}_{ij}$  as  $\mathcal{B}_i$ 's velocity component projected onto the direction of the spring  $\{i, j\}$ . For every contact  $\{i, j\} \in \mathbb{P}$ , we thus have

$$\tilde{v}_{ij} = \mathbf{v}_i \cdot \hat{\mathbf{n}}_{ij}. \quad (3.3)$$

Let  $x_{ij}$  be the change in length of the virtual spring  $\{i, j\}$ , and  $k_{ij}$  as its stiffness. The derivative of energy with respect to its impulse follow from equations (3.1) and (3.3):

$$\begin{aligned} \frac{dE_{ij}}{dI_{ij}} &= -\dot{x}_{ij} = \tilde{v}_{ji} - \tilde{v}_{ij} \\ &= \left( \mathbf{v}_j^{(0)} - \mathbf{v}_i^{(0)} \right) \cdot \hat{\mathbf{n}}_{ij} \\ &\quad + \frac{1}{m_j} \sum_{k \in \mathbb{C}_j} I_{jk} (\hat{\mathbf{n}}_{jk} \cdot \hat{\mathbf{n}}_{ij}) \\ &\quad - \frac{1}{m_i} \sum_{k \in \mathbb{C}_i} I_{ik} (\hat{\mathbf{n}}_{ik} \cdot \hat{\mathbf{n}}_{ij}). \end{aligned} \quad (3.4)$$

The potential energy stored in the spring  $\{i, j\}$  is  $E_{ij} = \frac{1}{2} k_{ij} x_{ij}^2$ , and the formula for the contact force by Hooke's law is  $F_{ij} = k_{ij} x_{ij}$ . Suppose the spring  $\{p, q\}$  accumulates the primary impulse  $I_{pq}$ , which has the largest growth during the period. The expression of  $dE_{pq}/dI_{pq}$  is given by (3.4) after replacing  $i, j$  with  $p, q$  from equation (3.4). Then, the differential ratio between  $I_{ij}$  and  $I_{pq}$  can be derived as

$$\rho_{ij} = \frac{dI_{ij}}{dI_{pq}} = \frac{F_{ij}}{F_{pq}} = \sigma_{ij} \sigma_{pq} \sqrt{\frac{k_{ij} E_{ij}}{k_{pq} E_{pq}}}. \quad (3.5)$$

Integration of equation (3.4) with initial value  $I_{ij}^{(0)}$  yields the accumulated change of energy:

$$\begin{aligned}
\Delta E_{ij} &= \left( \mathbf{v}_j^{(0)} - \mathbf{v}_i^{(0)} \right) \cdot \hat{\mathbf{n}}_{ij} \Delta I_{ij} \\
&\quad - \frac{1}{m_i} \sum_{k \in \mathbb{C}_i} \int_{\rho_{ij} I_{pq}^{(0)}}^{\rho_{ij} (I_{pq}^{(0)} + \delta)} (\hat{\mathbf{n}}_{ik} \cdot \hat{\mathbf{n}}_{ij}) \Delta I_{ik} dI_{ij} \\
&\quad + \frac{1}{m_j} \sum_{k \in \mathbb{C}_j} \int_{\rho_{ij} I_{pq}^{(0)}}^{\rho_{ij} (I_{pq}^{(0)} + \delta)} (\hat{\mathbf{n}}_{jk} \cdot \hat{\mathbf{n}}_{ij}) \Delta I_{jk} dI_{ij} \\
&\quad + \alpha_{ij} (e_{ij}^2 - 1) E_{ijmax},
\end{aligned} \tag{3.6}$$

where  $\delta$  is the increment of the primary impulse  $I_{pq}$ , and  $e_{ij} \in [0, 1]$  is the coefficient of restitution determined by the material properties of the two impacting objects. After the spring finishes compression, it starts to restitute, with the stiffness  $k_{ij}$  adjusted to  $k_{ij}/e_{ij}^2$  to reflect material hardening as explained in Jia et al. (2012). The value of  $\alpha_{ij}$  is set to be 0 during compression and 1 during restitution. At the end of compression, the spring stores the maximum energy  $E_{ijmax}$ , and then immediately loses a portion of  $1 - e_{ij}^2$ . We can work out the integrals in (3.6) below:

$$\int_{\rho_{ij} I_{pq}^{(0)}}^{\rho_{ij} (I_{pq}^{(0)} + \delta)} \Delta I_{ik} dI_{ij} = c \rho_{ij} \rho_{ik}, \tag{3.7}$$

$$\int_{\rho_{ij} I_{pq}^{(0)}}^{\rho_{ij} (I_{pq}^{(0)} + \delta)} \Delta I_{jk} dI_{ij} = c \rho_{ij} \rho_{jk}, \tag{3.8}$$

where  $c = (\delta^2 + 2I_{pq}^{(0)}\delta)/2$ . Substituting (3.7), (3.8) into (3.6), and adding initial energy  $E_{ij}^{(0)}$ , we get

$$\begin{aligned}
E_{ij} &= E_{ij}^{(0)} + \delta \left( \frac{dE_{ij}}{dI_{ij}} \right)^{(0)} \rho_{ij} - c \left( \frac{1}{m_j} + \frac{1}{m_i} \right) \rho_{ij}^2 \\
&\quad + \frac{c \rho_{ij}}{m_j} \left( \sum_{k \neq i, k \in \mathbb{C}_j} \rho_{jk} (\hat{\mathbf{n}}_{jk} \cdot \hat{\mathbf{n}}_{ij}) \right) \\
&\quad - \frac{c \rho_{ij}}{m_i} \left( \sum_{k \neq j, k \in \mathbb{C}_i} \rho_{ik} (\hat{\mathbf{n}}_{ik} \cdot \hat{\mathbf{n}}_{ij}) \right) \\
&\quad + \alpha_{ij} (e_{ij}^2 - 1) E_{ijmax}.
\end{aligned} \tag{3.9}$$

Squaring both sides of equation (3.5) and then plugging in (3.9), we get a systems of equations:

$$\frac{k_{pq}}{k_{ij}} \rho_{ij}^2 E_{pq} = E_{ij}, \quad \{i, j\} \in \mathbb{P}. \tag{3.10}$$



In the above system,  $\rho_{ij}$ ,  $\{i, j\} \in \mathbb{P}$ , are the variables. The energy  $E_{ij}$  is a polynomial of degree at most two, while  $E_{pq}$  has degree at most one. Thus, every equation in (3.10) is at most a cubic polynomial. Newton's method can be applied to solve this non-linear system, with the initial guesses of 1 for  $\rho_{pq}$ , where  $\{p, q\}$  is the contact yielding the primary impulse, and of 0 for  $\rho_{ij}$ , for any  $\{i, j\} \neq \{p, q\}$ . In the first round of initialization, if any  $\rho_{ij}$  exceeds 1, set the primary contact  $\{p, q\}$  to be such  $\{i, j\}$  that has the biggest  $\rho_{ij}$  value. With the updated primary impulse pair, the system should now be solved again to finish the initialization. This process ensures the biggest variable stay as the denominator in the differential relationships, which improves numerical stability.

### 3.2.2 Numerical integration

After initialization of  $\rho_{ij}^{(0)}$ , numerical integration is performed as follows. At the  $n$ th step, increment the primary impulse  $I_{pq}$  by  $\delta$ , and make the updates below:

$$\rho_{ij}^{(n)} = \sigma_{ij} \sigma_{pq} \sqrt{\frac{k_{ij} E_{ij}^{(n-1)}}{k_{pq} E_{pq}^{(n-1)}}}, \quad (3.11)$$

$$I_{ij}^{(n)} = I_{ij}^{(n-1)} + \delta \rho_{ij}^{(n)}, \quad (3.12)$$

$$E_{ij}^{(n)} = E_{ij}^{(n-1)} + \delta \rho_{ij}^{(n)} \left( \frac{dE_{ij}}{dI_{ij}} \right)^{(n)}, \quad (3.13)$$

where  $\left( \frac{dE_{ij}}{dI_{ij}} \right)^{(n-1)}$  is evaluated according to (3.4). In the step, the ball velocities are computed from (3.1). Algorithm 2 summarizes the above procedure.

### 3.2.3 Example

A Newton's cradle consists of five identical balls with mass  $m$  and radius  $r$  aligned in a row. Each ball is hanged by a string of length  $l$ . Denote by  $e$  the coefficient of restitution between two balls. See Fig. 3.2. Usually one drags the left end ball to a certain height and then releases it. Several multi-body collisions will happen after the release. Every ball carries out a simple pendulum motion before it collides with another ball. The angle  $\theta(t)$  between the perpendicular direction and the string at time  $t$  satisfies a second order ordinary differential equation. When it is small, under the approximation  $\sin \theta \approx \theta$ , the angle has a solution in the

---

**Algorithm 2** Frictionless collision for  $n$  balls with translation only
 

---

**Input:**  $\mathcal{B}_i$  with velocities  $\mathbf{v}_i^{(0)}$ ,  $1 \leq i \leq n$ , and contact set  $\mathbb{P}$

```

1: set the active contact set  $\mathbb{A} = \mathbb{P}$ 
2: while  $\mathbb{A} \neq \emptyset$  do
3:   solve  $\rho_{ij}$  from the system (3.10), update  $\mathbf{I}_{ij}, E_{ij}$  according to (3.12) and (3.13), also
      $\mathbf{v}_i, 1 \leq i \leq n$  according to (3.1)
4:   while  $\mathbb{A}$  does not change do
5:     update  $\rho_{ij}, \mathbf{I}_{ij}, E_{ij}$ , for all  $\{i, j\} \in \mathbb{A}$  and  $\mathbf{v}_i, 1 \leq i \leq n$  according to (3.11)–(3.13), and
     (3.1)
6:     for every  $\{i, j\} \in \mathbb{A}$  do
7:       if compression ends then
8:         add energy loss to  $E_{ij}$ 
9:       else if restitution ends then
10:        remove the contact  $\{i, j\}$  from  $\mathbb{A}$ 
11:      end if
12:    end for
13:    for every  $\{i, j\} \in \mathbb{P} \setminus \mathbb{A}$  that  $\mathbf{v}_i = \mathbf{v}_j$  do
14:      add the contact  $\{i, j\}$  to  $\mathbb{A}$ 
15:    end for
16:  end while
17: end while

```

---

form of

$$\theta(t) = A \cos(\omega t + \phi),$$

where  $\omega = \sqrt{g/l}$ , with  $g$  as the gravitational acceleration constant. The constants  $A$  and  $\phi$  can be determined from the initial configuration at time  $t = t_0$ : the angle  $\theta_0$  of the pendulum and

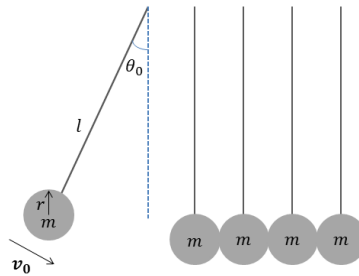


Figure 3.2: Newton's cradle.

the tangential velocity  $v_0$  as shown in Fig. 3.2. We obtain

$$\begin{aligned}\theta(t) &= \sqrt{\theta_0^2 + \frac{v_0^2}{gl}} \cos\left(\sqrt{\frac{g}{l}}t + \beta_0 - \sqrt{\frac{g}{l}}t_0\right), \\ v(t) &= -\sqrt{\theta_0^2 + \frac{v_0^2}{gl}} \sqrt{gl} \sin\left(\sqrt{\frac{g}{l}}t + \beta_0 - \sqrt{\frac{g}{l}}t_0\right).\end{aligned}$$

where  $\beta_0$  is a constant offset determined by  $\theta_0$ ,  $v_0$ ,  $g$ , and  $l$ . As time goes by, collisions are detected by checking if several balls are close enough with non-negligible relative velocities. Each ball may switch to a different simple pendulum motion due to the next collision which results in a sudden change of velocity. Algorithm 2 is applied to compute the motion of the balls for each collision. For more accurate modeling, Hertz contact is used with  $F = kx^{3/2}$ . Then equation (3.5) becomes

$$\rho_{ij} = \frac{dI_{ij}}{dI_{pq}} = \frac{F_{ij}}{F_{pq}} = \sigma_{ij}\sigma_{pq}^{5/2} \sqrt{\frac{k_{ij}E_{ij}^{3/2}}{k_{pq}E_{pq}^{3/2}}}.$$

Newton's method can still be applied to solve this quartic polynomial system. Simulation and experimental results will be shown in section 3.4.1.

### 3.3 Collision under General Motions with Friction

In this section, we will extend the impact model by considering friction and angular velocity of arbitrary shape objects in the system of collision treated in Section 3.2. As before, the objects involved in the collision are assumed to have their centers of mass lying on the same plane. Suppose for every pair of objects, the center of masses and the contact point are in the same line. Section 4.6 will discuss how the assumption can be removed.

#### 3.3.1 Impact dynamics and contact kinematics

Denote by  $\mathbf{v}_i$  and  $\boldsymbol{\omega}_i$  the velocity and angular velocity of the object  $\mathcal{B}_i$  in the world frame. At the moment of collision, let  $\mathbf{r}_{ik}$  be the vector from  $\mathcal{B}_i$ 's center of mass to the contact point between  $\mathcal{B}_i$  and  $\mathcal{B}_k$ . The angular inertia matrix  $Q_i$  of  $\mathcal{B}_i$  is diagonal in its principal frame, which has undergone a rotation described by the matrix  $R_i$  from the world frame. For instance, if  $\mathcal{B}_i$

is a ball with radius  $\tau$ , then

$$Q_i = \frac{2}{5} m_i \tau^2 \begin{pmatrix} 1 & 0 & 0 \\ 0 & 1 & 0 \\ 0 & 0 & 1 \end{pmatrix}.$$

In the world frame, the changes in the velocities and angular velocities of  $\mathcal{B}_i$ ,  $i = 1, \dots, n$ , during the impact can be derived from dynamics:

$$m_i \Delta \mathbf{v}_i = \sum_{k \in \mathcal{C}_i} \mathbf{I}_{ik}, \quad (3.14)$$

$$Q_i (R_i^{-1} \Delta \boldsymbol{\omega}_i) = \sum_{k \in \mathcal{C}_i} R_i^{-1} (\mathbf{r}_{ik} \times \mathbf{I}_{ik}). \quad (3.15)$$

Compared with the frictionless case studied in Section 3.2, impulse now exists in the tangential plane at the contact between two objects. Here, let  $I_{ik\perp}$  be the magnitude of the tangential impulse between  $\mathcal{B}_i$  and  $\mathcal{B}_k$  shown in Fig. 3.3, which is the projection of the total impulse  $\mathbf{I}_{ik}$ , exerted by  $\mathcal{B}_k$  on  $\mathcal{B}_i$ , onto the tangential plane. The component of  $I_{ij\perp}$  in the  $x$ - $y$  plane is

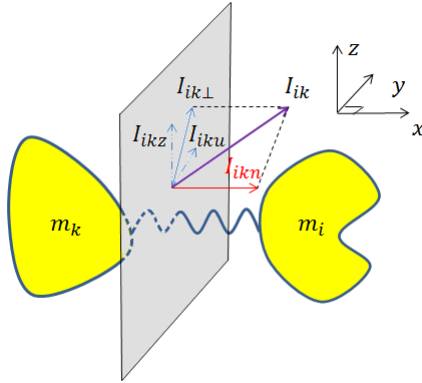


Figure 3.3: Impulse decomposition along normal and tangential directions.

$I_{iku}$ , and the vertical component in  $z$ -direction is  $I_{ikz}$ . Compared to equation (3.2), we now have the velocity in  $x$ -direction and  $y$ -direction as

$$\begin{pmatrix} v_{ix} \\ v_{iy} \end{pmatrix} = \begin{pmatrix} v_{ix}^{(0)} \\ v_{iy}^{(0)} \end{pmatrix} + \frac{1}{m_i} \sum_{k \in \mathcal{C}_i} \begin{pmatrix} I_{ikn} \cos \theta_{ik} - I_{iku} \sin \theta_{ik} \\ I_{ikn} \sin \theta_{ik} + I_{iku} \cos \theta_{ik} \end{pmatrix}. \quad (3.16)$$

The differential relationship between the energy and normal impulse at the contact between object  $\mathcal{B}_i$  and  $\mathcal{B}_j$  is

$$\begin{aligned} \frac{dE_{ij}}{dI_{ijn}} &= \hat{\mathbf{n}}_{ij} \cdot \left( \left( \mathbf{v}_j^{(0)} - \mathbf{v}_i^{(0)} \right) \right. \\ &\quad \left. + \frac{1}{m_j} \sum_{k \in \mathcal{C}_j} (I_{jkn} \hat{\mathbf{n}}_{jk} + I_{jku} \hat{\mathbf{u}}_{jk}) \right. \\ &\quad \left. - \frac{1}{m_i} \sum_{k \in \mathcal{C}_i} (I_{ikn} \hat{\mathbf{n}}_{ik} + I_{iku} \hat{\mathbf{u}}_{ik}) \right). \end{aligned} \quad (3.17)$$

The variable  $\rho_{ij}$  defined in (3.5) for the frictionless case is now replaced by  $\rho_{ijn}$ , whose initial value will still be solved from the system of equations using Newton's method. An expression for  $E_{ij}$  can be derived by integrating equation (3.17) similarly as in Section 3.2.

During the impact, we need to consider the contact mode (stick or slip) between  $\mathcal{B}_i$  and  $\mathcal{B}_j$ . The velocity of  $\mathcal{B}_i$  relative to that of object  $\mathcal{B}_j$  at the contact is

$$\Delta \mathbf{v}_{ij} = \mathbf{v}_i - \mathbf{v}_j + \boldsymbol{\omega}_i \times \mathbf{r}_{ij} - \boldsymbol{\omega}_j \times \mathbf{r}_{ji}.$$

Project  $\Delta \mathbf{v}_{ij}$  onto tangent plane,

$$\Delta \mathbf{v}_{ij\perp} = \Delta \mathbf{v}_{ij} - \Delta \mathbf{v}_{ij} \cdot \hat{\mathbf{n}}_{ij}. \quad (3.18)$$

After simplification, the right hand side of the above equation can be written as linear combinations of  $\Delta I_{ijx}$ ,  $\Delta I_{ijy}$ , and  $\Delta I_{ijz}$ .

The contacts among the  $n$  objects can be either sliding or sticking. We denote the set of sliding contacts as  $\mathbb{S}$ , and the set of sticking contacts as  $\mathbb{T}$ . The elements in each set are the pairs of indices for objects engaged in the corresponding contact mode. Clearly,  $\mathbb{P} = \mathbb{S} \cup \mathbb{T}$ .

### 3.3.2 Sticking mode

If the contact  $\{i, j\}$  sticks, their relative velocities in the tangent plane should all be zero, i.e.,

$$\Delta \mathbf{v}_{ij\perp} = 0, \quad \{i, j\} \in \mathbb{T}. \quad (3.19)$$

Let  $|\mathbb{T}|$  be the size of the set  $\mathbb{T}$ . The above equations form a linear system with  $3|\mathbb{T}|$  equations and  $3|\mathbb{T}|$  variables. Each  $\Delta \bar{\mathbf{v}}_{ij}$  has three components along the  $x$ -,  $y$ - and  $z$ -axes, and also each

equation has  $3|\mathbb{T}|$  variables  $\Delta I_{ijx}$ ,  $\Delta I_{ijy}$ , and  $\Delta I_{ijz}$ ,  $\{i, j\} \in \mathbb{T}$ . The values for  $\Delta I_{ijn}$ ,  $\Delta I_{iju}$ , and  $\Delta I_{ijz}$  can be computed by:

$$\begin{pmatrix} \Delta I_{ijn} \\ \Delta I_{iju} \\ \Delta I_{ijz} \end{pmatrix} = R_{ik}^{-1} \begin{pmatrix} \Delta I_{ijx} \\ \Delta I_{ijy} \\ \Delta I_{ijz} \end{pmatrix} \quad (3.20)$$

After solving the system, one can check the ratio  $\gamma_{ij}$  between the tangential impulse and the normal impulse at the contact  $\{i, j\}$ , that is,

$$\gamma_{ij} = \Delta I_{ij\perp} / \Delta I_{ijn}.$$

Denote  $\mu_{ij}$  as the coefficient of friction between  $\mathcal{B}_i$  and  $\mathcal{B}_j$ . If  $\gamma_{ij} < \mu_{ij}$ , we still have values of  $\Delta I_{iju}$  and  $\Delta I_{ijz}$  as they are solved from the system, and

$$\Delta I_{ij\perp} = \gamma_{ij} \Delta I_{ijn}. \quad (3.21)$$

### 3.3.2.1 Sticking to sliding

If  $\gamma_{ij} \geq \mu_{ij}$ , then sliding happens between  $\mathcal{B}_i$  and  $\mathcal{B}_j$ . According to Coulomb's friction law, we set

$$\Delta I_{ij\perp} = \mu_{ij} \Delta I_{ijn}. \quad (3.22)$$

The values of  $\Delta I_{iju}$  and  $\Delta I_{ijz}$  are modified to be  $\Delta I_{iju} \mu_{ij} / \gamma_{ij}$  and  $\Delta I_{ijz} \mu_{ij} / \gamma_{ij}$ . The sliding direction is opposite to the vector  $(\Delta I_{iju} \mu_{ij} / \gamma_{ij}, \Delta I_{ijz} \mu_{ij} / \gamma_{ij})$ .

### 3.3.3 Sliding mode

Sliding happens when the following holds:

$$\Delta \mathbf{v}_{ij\perp} \neq 0, \quad \{i, j\} \in \mathbb{S}. \quad (3.23)$$

Then,

$$\Delta I_{ij\perp} = \mu_{ij} \Delta I_{ijn}. \quad (3.24)$$

Variables  $\Delta I_{iju}$  and  $\Delta I_{ijz}$  are determined by

$$\begin{aligned} \frac{1}{\|I_{ij\perp}\|} \begin{pmatrix} \Delta I_{iju} \\ \Delta I_{ijz} \end{pmatrix} &= -\Delta \mathbf{v}_{ij} / \|\Delta \mathbf{v}_{ij}\| \\ \Delta I_{iju}^2 + \Delta I_{ijz}^2 &= \Delta I_{ij\perp}^2 \end{aligned} \quad (3.25)$$

### 3.3.3.1 Sliding to sticking

Whenever the relative velocity  $\Delta \mathbf{v}_{ij}$  is small enough, we move the pair  $\{i, j\}$  from  $\mathbb{S}$  to  $\mathbb{T}$ .

### 3.3.4 Algorithm

We perform numerical integration to update all the impulses, energies, velocities, and angular velocities. The computation is described in Algorithm 3. Simulation results of nine-ball break shots will be presented in Section 3.4.2.

---

#### Algorithm 3 Frictional $n$ -body collision

---

**Input:** objects  $\mathcal{B}_i$  with velocities  $\mathbf{v}_i^{(0)}$  and angular velocities  $\boldsymbol{\omega}_i^{(0)}$ ,  $1 \leq i \leq n$ , and contact set  $\mathbb{P}$

- 1: set the active contact set  $\mathbb{A} = \mathbb{P}$ . Compute the initial relative velocity  $\Delta \mathbf{v}_{ij}$  of each  $\{i, j\} \in \mathbb{A}$  to set up the initial sliding set  $\mathbb{S}$  and sticking set  $\mathbb{T}$ . Note  $\mathbb{A} = \mathbb{S} \cup \mathbb{T}$ .
  - 2: **while**  $\mathbb{A} \neq \emptyset$  **do**
  - 3: solve  $\rho_{ij}$  from the system (3.10) according to  $\frac{dE_{ij}}{dI_{ijn}}$  from (3.17), update  $I_{ijn}, E_{ij}$  from (3.12) and (3.13),  $I_{ij\perp}$  from (3.21) or (3.22), also update  $\mathbf{v}_i, \boldsymbol{\omega}_i, 1 \leq i \leq n$  by (3.14) and (3.15) according to set  $\mathbb{S}$  or  $\mathbb{T}$
  - 4: **while**  $\mathbb{A}$  does not change **do**
  - 5: update  $\rho_{ij}, I_{ijn}, E_{ij}$  and  $\mathbf{v}_i, \boldsymbol{\omega}_i, 1 \leq i \leq n$  from (3.11)–(3.15)
  - 6: Check if any of the events happen based on Section 3.3.2 and 3.3.3. Update the sets  $\mathbb{S}$  and  $\mathbb{T}$ , and values of  $I_{iju}$  and  $I_{ijz}$  of each  $\{i, j\} \in \mathbb{A}$
  - 7: execute lines 6–15 in Algorithm 2
  - 8: **end while**
  - 9: **end while**
- 

## 3.4 Simulation and experiment

In this section, we first present simulation of Newton's cradle by applying the frictionless model described in Section 3.2, and compare the results with those from an experiment we

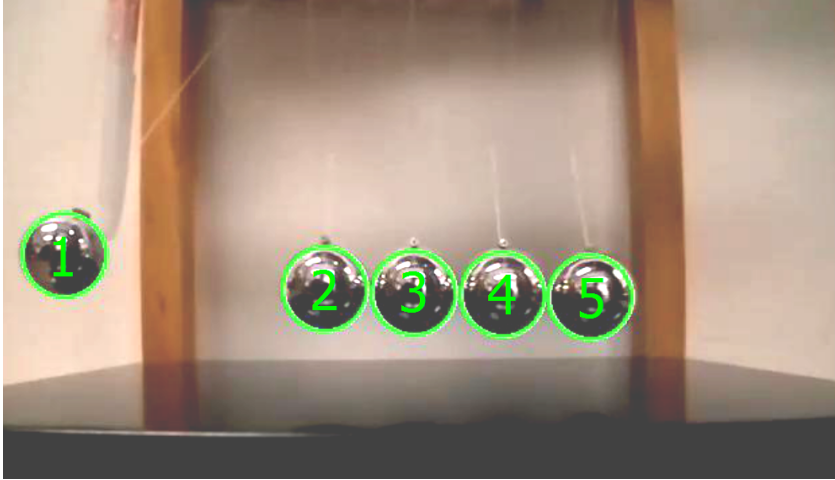


Figure 3.4: Initial State of Newton's cradle. Green circles mark the contours of the five balls, which are number 1 to 5 from left to right.

conducted. Next, we conduct simulation on nine-ball breakshots using the model in Section 3.3.

#### 3.4.1 Newton's cradle

To experimentally validate Algorithm 2, a Newton's Cradle with string length  $l = 0.129\text{m}$  was placed on a horizontal table. The five identical balls of the cradle have radius  $r = 0.011\text{m}$ . The coefficient of restitution between any two balls is  $e = 0.95$ , and the stiffness between them is the same. The leftmost ball was initially raised and held static with oscillation angle  $5\pi/36$  as shown in Fig. 3.4. Started at the release, a video was captured by a Fujifilm FinePix HS10 camera with frame rate 30fps. Hough Circle Transform algorithm Yuen et al. (1990) in Matlab was applied to track the contours of five balls during their motion. Velocities were estimated based on the tracked positions of balls and the frame rate.

Table 3.1 compares the horizontal velocities  $v_x$  and  $\tilde{v}_x$  (m/s) of the five balls right after they were disengaged from the first collision in the experiment and the simulation. Interestingly, ball 1 was moving leftward slightly, and ball 4 was moving rightward with noticeable velocity in both the experiment and simulation. This phenomenon cannot be explained by a simpler model based on conservation of momentum and energy only, and our multi-body collision model can simulate this scenario in a realistic way.



Table 3.1: Comparisons of experimental (second row) and simulation (third row) outcomes from the first collision of the five balls. Listed are the ball velocities in the  $x$ -direction.

ball	1	2	3	4	5
$v_x$	-0.0578	-0.0224	0.0003	0.1322	0.4508
$\tilde{v}_x$	-0.0568	-0.0380	-0.0002	0.1450	0.4401

The experimental and simulation results are also compared along the time axis until no more impact happened and all the balls swung together. Fig. 3.5 compares the time trajectories of the horizontal velocities of ball 1 observed in the experiment and predicted by simulation. The two trajectories match very well, except that during each cycle (shown in the inset) the ball velocity fluctuates slightly more in simulation than in the experiment. This is mainly due to some sticking effect between the balls in the experiment that is not modeled by Algorithm 2.

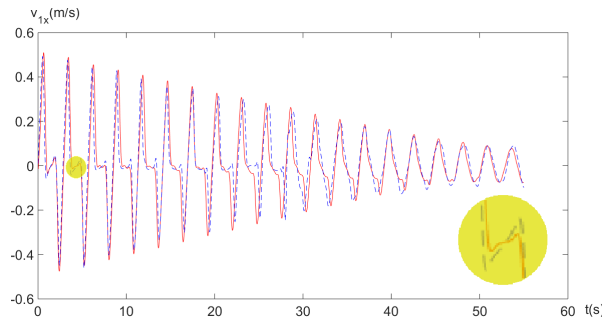


Figure 3.5: Time trajectories of the horizontal velocity of Newton's cradle: experiment (red line) vs. simulation (blue dashed line).

### 3.4.2 Billiard break shots

Nine-ball break shots are a good testbed for Algorithm 3 described in Section 3.3. There are ten identical balls (including a cue ball) on the pool table with radius  $r$  and mass  $m$ . The cue stick shoots the cue ball to generate initial velocity  $\mathbf{v}_0$  and angular velocity  $\boldsymbol{\omega}_0$ . The initial configuration is shown in Fig. 3.6. The coefficient of friction between any two balls is the same, and denoted as  $\mu_{bb}$ . Friction between a ball and the table is ignored during the impact. After the shot, the balls will be moving under sliding or rolling friction with the table. Let  $\mu_{bt}$  and  $\tilde{\mu}_{bt}$  be the coefficients of sliding and rolling friction. We applied the technique in Jia

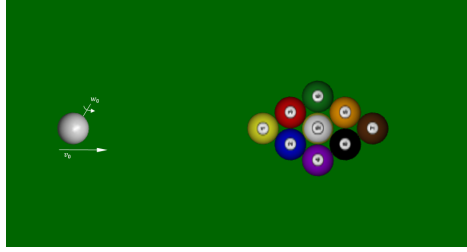


Figure 3.6: Initial state of nine-ball break shot.

(2015) to compute the trajectories of the balls with given velocities and angular velocities in our simulation.

Algorithm 3 is implemented to simulate break shots with parameters listed in Table 3.2. Fig. 3.8 compares the final configurations following three different shots at the cue ball: stop shot, follow shot and draw shot. Immediately after each shot, the cue ball gains the same initial velocity  $(1, 0, 0)$ , but angular velocities  $(0, 0, 0)$ ,  $(0, 20, 0)$ , and  $(0, -20, 0)$ , respectively. The results show that compared to a stop shot, the balls tend to spread out more under a follow shot and less under a draw shot.

Table 3.2: Parameters used for modeling break shots include  $d_b$ : the diameter of the balls;  $m_b$ , the mass of the balls;  $\mu_{bb}$ , the ball-ball coefficient of friction;  $e_{bb}$ , the ball coefficient of restitution;  $\mu_{bt}$ , the ball-table coefficient of friction; and  $\tilde{\mu}_{bt}$ , the ball-table coefficient of rolling resistance.

$d_b$ (m)	$m_b$ (kg)	$\mu_{bb}$	$e_{bb}$	$\mu_{bt}$	$\tilde{\mu}_{bt}$
0.06	0.17	0.03	0.96	0.2	0.01

In order to show the friction effect during a ball-ball impact, we perform a two-ball collision shown in Fig. 3.9 with different  $\mu_{bb}$  values. Table 3.3 lists the results of ball 2 under the same follow shot with initial velocity  $(1, 0, 0)$  and angular velocity  $(0, 40, 0)$ . The table includes only the velocity component along the  $x$ -axis and the angular velocity component along the  $y$ -axis since the other components are zero in this configuration. It can be seen from the table that as  $\mu$  increases, the velocities of the two balls after impact remain the same, since ball-table friction is not modeled during their collision. At the same time, ball 2 gains higher backward angular velocity and thus moves less. The reason is that with ball-ball friction, the top spin of ball 1 caused by the follow shot leads to back spin for ball 2.

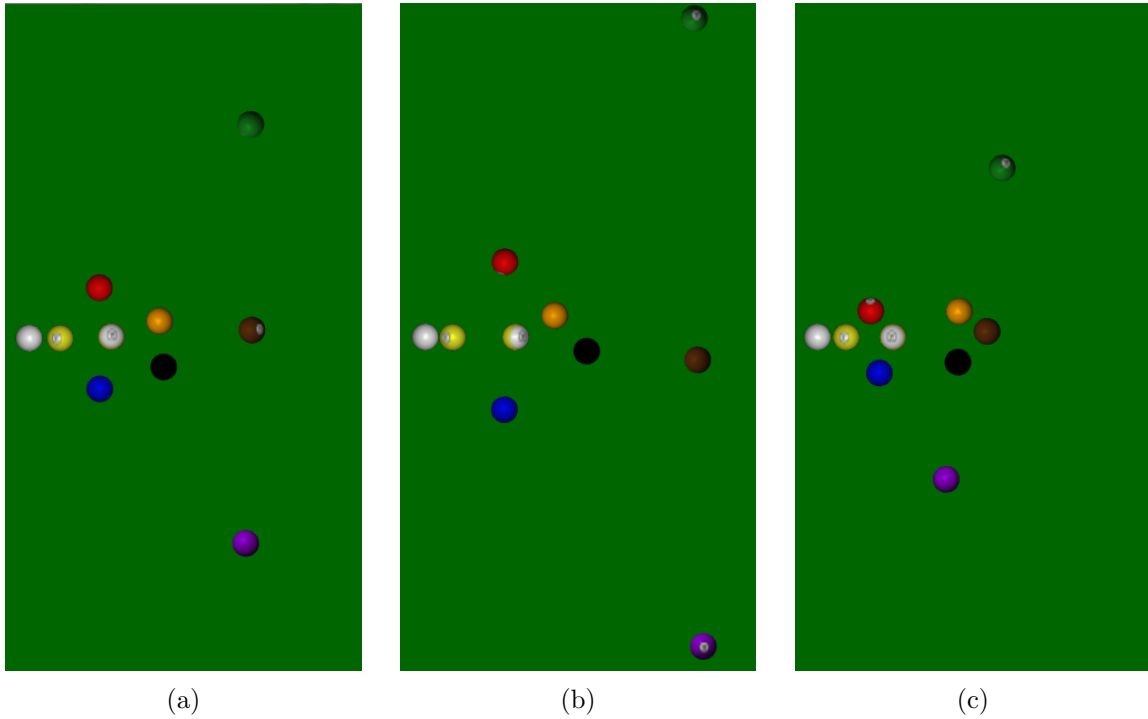


Figure 3.8: Resting configurations of ten balls (leftmost one being the cue ball) after three break shots: (a) stop shot, (b) follow shot, and (c) draw shot.



Figure 3.9: Initial state of two-ball example.

Table 3.3: Effect of ball-ball friction during impact.  $\mu_{bb}$ , the coefficient of ball-ball friction;  $v_{1x}$ ,  $w_{1y}$ ,  $v_{2x}$ , and  $w_{2y}$ , the velocities and angular velocities of ball 1 and 2 after impact, respectively; and  $d_2$ , the displacement of ball 2.

$\mu_{bb}$	0.0	0.5	1.0
$v_{1x}$ (m/s)	0.001742	0.001742	0.001742
$w_{1y}$ (rad/s)	34.96	-8.66742	-52.2949
$v_{2x}$ (m/s)	1.04706	1.04706	0.001742
$w_{2y}$ (rad/s)	0.0	-43.6275	-87.2549
$d_2$ (m)	4.14561	1.25774	0.279677

## CHAPTER 4. PLANNING THE CONTACT VELOCITY FOR ROBOTIC BATTING

Impulsive forces are more efficient than dynamic and static forces, and are used to achieve everyday tasks that would be difficult or impossible using the latter two types of forces. Yet, impact is rarely used in robotic manipulation due to difficulties in modeling, planning, and control. This paper studies the problem of batting a free flying object to a target location, with a focus on computing a contact velocity between the bat and the object to generate needed impact on the latter to alter its trajectory as desired. Based on our recent analysis Jia and Wang (2017) of 3D impact, we will first examine several invariant sliding directions in the contact plane for which the generated impulse has a closed form. In case no contact velocity yielding the initial slip in such a direction achieves the batting task, an iterative algorithm will be employed to perform corrections from how far the resulting object trajectory would off the target. Simulation results will be presented.

### 4.1 Introduction

Impulsive manipulation is challenging for several reasons: extremely short duration (less than 0.1 second) of an action; no feedback until after its completion (when the outcome is usually determined); differential equation based impact modeling subject to friction, compliance, and contact irregularities; and high computational cost to present a huge obstacle for real-time planning. The loads on sensing and state estimation can become very demanding especially when objects moving at fast speeds are involved in such a manipulation task. Simply picture a move, say, in ball sports, such as returning a serve in tennis, bending a soccer ball around a defense, or batting an incoming baseball.

Despite the challenge, research progress in the area has been made on parts positioning Higuchi (1985) and sorting Hirai et al. (1999b), air hockey playing Partridge and Spong (2000) , and parts orienting via a single strike Han and Park (2001), repeated taps Huang and Mason (2000b), or a drop onto certain surface to achieve minimal entropy Moll and Erdmann (2002).

Most of the above works involved impulsive actions performed on objects resting on supporting surfaces. Batting a free flying object, our main interest, is technically more challenging and draws upon computer vision, motion estimation, trajectory analysis, impact planning, and the robot’s own kinematics and dynamics. Analysis was given for the velocity of a ball imparted through batting Kirkpatrick (1963). The work Senoo et al. (2004) decomposed batting into a swing and a hit, and planned the swing trajectory under the guidance of two cameras with pan-tilting capability. Recent work Gardner et al. (2016) involving the co-author reported some initial results on using a 2-DOF robotic arm to bat objects to a target in the vertical plane by combining impact dynamics with manipulator kinematics, planning, and computer vision.

Our goal is to tackle the batting task in full three dimension. A major obstacle for real-time planning is that the 3D impact problem generally does not have a closed-form solution and has to be solved through numerical integration, as analyzed in Jia and Wang (2017). The inverse problem of finding a motion of the bat to impart a desired change to the motion of the object could become prohibitively expensive.

We will focus on finding a contact velocity just before batting happens to cause the desired change in the object’s motion. Two approaches will be proposed. The first one makes use of special contact velocities to generate impulses in closed form. Planning is very fast, but may not find a solution sometimes. The second method uses a triangular bounding box to tackle the general situation, by sacrificing efficiency due to repeated numerical simulations of impact.

## 4.2 Impact Dynamics and Invariant Directions

In this section, we go over the basics of two body impact in 3D. In our context, one of the rigid bodies is a robotic bat, while the other is an object, as shown respectively on the left and right in Fig. 4.1.

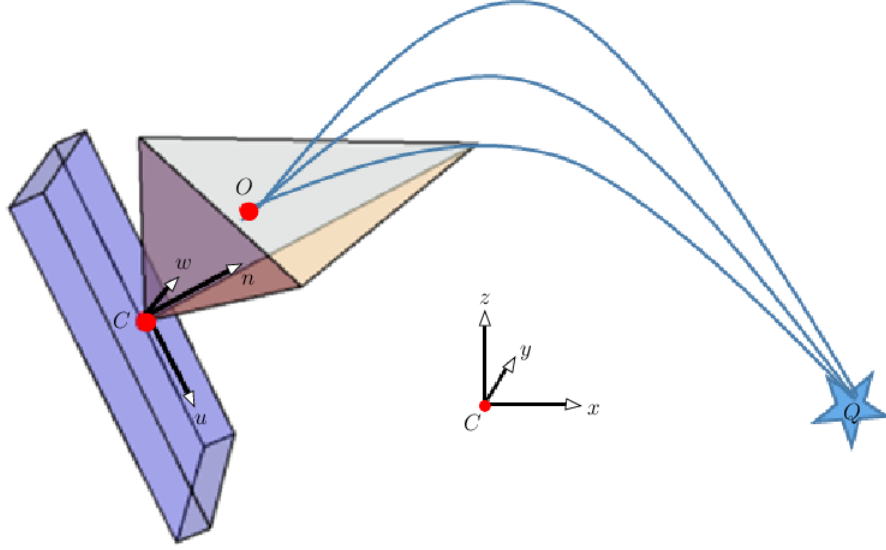


Figure 4.1: Impact between a tetrahedron object and a cuboid bat, both having uniform mass density and unit mass. The target  $Q$  is located at  $(5, -0.2, -2)^T$ . The contact frame  $\mathcal{F}_c$  rotates from the world frame  $\mathcal{F}_w$  about its  $y$ -axis through  $\pi/3$ . The contact point  $C$  as the origin of both frames coincides with one vertex of the tetrahedron, whose other vertices are located at  $(0.433013, -0.5, 0.25)^T$ ,  $(0.866025, 0.5, 0.5)^T$ , and  $(-0.0334936, -0.25, 0.558013)^T$ . The bat has length 1.0, width 1.0 and thickness 0.1. Other geometric and physical parameters include the centers of mass of the object  $O = (0.316386, -0.0625, 0.327003)^T$  and the bat  $O_b = (-0.0433013, 0, -0.025)^T$ , their angular inertia matrices  $M_o = \text{diag}(0.0248286, 0.0401528, 0.0631436)$ , and  $M_b = \text{diag}(0.166667, 0.0841667, 0.0841667)$ , and their rotation matrices  $R_o = \{\{-0.759372, -0.473448, 0.446319\}, \{0.411757, -0.8808 - 0.23377\}, \{0.503796, 0.00625615, 0.8638\}\}$  and  $R_b$  which represents a rotation about the  $y$ -axis through  $-\pi/3$ . The coefficient of friction is  $\mu = 0.5$  and the coefficient of restitution is  $e = 0.95$ . The object has the velocity  $\mathbf{V}_o^- = (-1, 0.6, -0.4)^T$  just before the impact.

Placed at their contact point  $C$  are a world frame  $\mathcal{F}_w$  (with  $x$ -,  $y$ -,  $z$ -axes) and a local frame  $\mathcal{F}_c$  (with  $u$ -,  $w$ -,  $n$ -axes). The  $n$ -axis is along the inward normal  $\hat{n}$  of the object at  $C$ . The matrix  $R$  describes the rotation from  $\mathcal{F}_w$  to  $\mathcal{F}_c$ . Located at the centers of mass of the bat and the object are two principal body frames  $\mathcal{F}_b$  and  $\mathcal{F}_o$ , under which their angular inertia matrices  $M_b$  and  $M_o$  are diagonalized.<sup>1</sup> Also, denote the rotation matrices from  $\mathcal{F}_w$  to  $\mathcal{F}_o$  and  $\mathcal{F}_w$  to  $\mathcal{F}_b$  as  $R_o$  and  $R_b$  respectively. The objective is to bat the object such that its center of mass  $O$  will pass through a target point  $Q$ .

<sup>1</sup>All the terms with the subscript ‘ $o$ ’ are related to the flying object, and with the subscript ‘ $b$ ’ are related to the robotic bat.

Let  $\mathbf{V}_o$  and  $\mathbf{V}_b$  be the velocities of the object and the bat, and  $\boldsymbol{\omega}_o$  and  $\boldsymbol{\omega}_b$  their angular velocities. Based on Newton's and Euler's equations on dynamics,

$$\begin{aligned}\mathbf{F} &= m_o \dot{\mathbf{V}}_o, \\ R_o^{-1}(\mathbf{r}_o \times \mathbf{F}) &= M_o \dot{\boldsymbol{\omega}}_o + \boldsymbol{\omega}_o \times M_o \boldsymbol{\omega}_o,\end{aligned}$$

where the dot '.' denotes differentiation with respect to time. Similar equations hold for the bat. Integrate the above equations with respect to time:

$$\begin{aligned}\Delta \mathbf{V}_o &= \mathbf{V}_o^+ - \mathbf{V}_o^- = \frac{1}{m_o} \mathbf{I}, \quad \Delta \boldsymbol{\omega}_o = M_o^{-1} R_o^{-1}(\mathbf{r}_o \times \mathbf{I}), \\ \Delta \mathbf{V}_b &= \mathbf{V}_b^+ - \mathbf{V}_b^- = -\frac{1}{m_b} \mathbf{I}, \quad \Delta \boldsymbol{\omega}_b = -M_b^{-1} R_b^{-1}(\mathbf{r}_b \times \mathbf{I}).\end{aligned}\tag{4.1}$$

In the above,  $\mathbf{I}$  is the impulse exerted by the bat onto the object;  $\mathbf{V}_o^+$  and  $\mathbf{V}_o^-$  are the post- and pre-impact values of  $\mathbf{V}_o$ ,  $\Delta \boldsymbol{\omega}_o$  is the object's change of angular velocity;  $\mathbf{r}_o$  and  $\mathbf{r}_b$  are the vectors from  $C$  to  $O$  and the bat's center of mass, respectively.

The contact velocity at  $C$  is

$$\mathbf{v} = \mathbf{V}_o + (R_o \boldsymbol{\omega}_o) \times \mathbf{r}_o - \mathbf{V}_b - (R_b \boldsymbol{\omega}_b) \times \mathbf{r}_b.\tag{4.2}$$

From (4.1) and (4.2), the change of  $\mathbf{v}$  during the impact is

$$\begin{aligned}\Delta \mathbf{v} &= \Delta \mathbf{V}_o + (R_o \Delta \boldsymbol{\omega}_o) \times \mathbf{r}_o - \Delta \mathbf{V}_b - (R_b \Delta \boldsymbol{\omega}_b) \times \mathbf{r}_b \\ &= W \mathbf{I},\end{aligned}\tag{4.3}$$

where  $W$  is shown to be a positive definite matrix Jia and Wang (2017).

To describe the impact, picture a virtual spring placed at the contact to store and later release energy  $E$  as the process goes on. The energy derivative is

$$E' = -v_n^- - \left(\frac{1}{m_1} + \frac{1}{m_2}\right) I_n + \hat{\mathbf{n}}^T S \mathbf{I},\tag{4.4}$$

where  $v_n^-$  is the normal component of the initial contact velocity  $\mathbf{v}^-$  in the contact frame  $\mathcal{F}_c$ , and  $I_n$  is the normal impulse. The spring first compresses and then restitutes. Compression ends when  $E' = 0$ . An energy loss by the factor of  $1 - e^2$  then takes place, where  $e$  is the coefficient of restitution. Afterward, the impact goes into restitution to end at  $E = 0$ . The tangential component of  $\mathbf{I}$  can be expressed in terms of  $I_n$ .

The contact velocity  $\mathbf{v}$  has a normal component  $v_n$  and a tangential component  $\gamma_{yz} = (v_u, v_w)^T$ , called the *sliding velocity*. The sliding velocity is governed by the differential equation  $\gamma'_{yz} = -\mu B \hat{\gamma} + \mathbf{d}$  Jia and Wang (2017), where  $B = (\hat{\mathbf{u}}, \hat{\mathbf{w}})^T W(\hat{\mathbf{u}}, \hat{\mathbf{w}})$ ,  $\mathbf{d} = (\hat{\mathbf{u}}, \hat{\mathbf{w}})^T W \hat{\mathbf{n}}$ ,  $\mu$  is the coefficient of friction. Here, the notation  $'$  means differentiation with respect to the normal impulse  $I_n$ .

When  $\gamma_{yz}^- \neq \mathbf{0}$ , sliding happens such that

$$\mathbf{I}' = \boldsymbol{\delta} := \hat{\mathbf{n}} - \mu(\hat{\mathbf{u}}, \hat{\mathbf{w}})\hat{\gamma}. \quad (4.5)$$

When  $\gamma_{yz}^- = \mathbf{0}$  or  $\gamma_{yz}$  becomes zero later, either sticking or resumed sliding will happen with Jia and Wang (2017)

$$\mathbf{I}' = \boldsymbol{\sigma} := \begin{cases} \hat{\mathbf{n}} - (\hat{\mathbf{u}}, \hat{\mathbf{w}})B^{-1}\mathbf{d}, & \text{if } \|B^{-1}\mathbf{d}\| \leq \mu \text{ (sticking);} \\ \hat{\mathbf{n}} - \mu(\hat{\mathbf{u}}, \hat{\mathbf{w}})\hat{\mathbf{s}}, & \text{if } \|B^{-1}\mathbf{d}\| > \mu \\ & \text{(resumed sliding).} \end{cases} \quad (4.6)$$

In the above,  $\hat{\mathbf{s}}$  is the unique direction in the  $u$ - $w$  plane, existing only when  $\|B^{-1}\mathbf{d}\| > \mu$ , to satisfy

$$-\mu B \hat{\mathbf{s}} + \mathbf{d} = \lambda \hat{\mathbf{s}}, \quad (4.7)$$

for some  $\lambda$ , and  $\hat{\mathbf{s}}^T(-\mu B \hat{\mathbf{s}} + \mathbf{d}) > 0$ . It is called *centrifugal invariant* Elkaranshawy (2007). According to the impact analysis in Jia and Wang (2017), up to four directions  $\hat{\mathbf{s}}$  exist in the  $u$ - $w$  plane to satisfy (4.7), namely,

$$(-\mu B \hat{\mathbf{s}} + \mathbf{d}) \times \hat{\mathbf{s}} = 0. \quad (4.8)$$

Those also satisfying  $\hat{\mathbf{s}}^T(-\mu B \hat{\mathbf{s}} + \mathbf{d}) \leq 0$  are called *centripetal invariant*.

If  $\gamma_{yz}^-$  is in an invariant direction  $\hat{\mathbf{s}}$ , then  $\gamma_{yz}$  satisfies

$$\gamma_{yz}(I_n) = \gamma_{yz}^- + \lambda I_n \hat{\mathbf{s}}^-, \quad (4.9)$$

and  $\mathbf{I}' = \boldsymbol{\delta}$  before  $\gamma_{yz}$  reaches zero and  $\mathbf{I}' = \boldsymbol{\sigma}$  after  $\gamma_{yz}$  reaches zero. A closed form of the impulse  $\mathbf{I}$  thus exists. Consequently, the impact problem has a closed form solution.



### 4.3 Solution Impulse

Given the impact configuration, the impulse is completely determined by the initial contact velocity  $\mathbf{v}^-$ , so we can write the total impulse as a function of initial contact velocity as  $\mathbf{I}(\mathbf{v}^-)$ . We assume that the object's pre-impact velocity  $\mathbf{V}_o^-$  and pre-impact angular velocity  $\boldsymbol{\omega}_o^-$  are known. We would like to find one value of  $\mathbf{v}^-$ , realizable by controlling the bat's pre-impact velocity  $\mathbf{V}_b^-$  and angular velocity  $\boldsymbol{\omega}_b^-$  via (4.3), to impart a velocity change  $\Delta\mathbf{V}_o$  that will take the object to the target  $Q$ . Note that every  $\mathbf{v}^-$  can be realized by a three-dimensional set of  $(\mathbf{V}_b, \boldsymbol{\omega}_b)$  values.

We approach the problem in two steps. This section will characterize the set of impulses that will change the object's velocity so it will go to  $Q$ . Such a impulse is called a *solution impulse*. In the next section, we will look at how to find a value of  $\mathbf{v}^-$  to generate a solution impulse.

After the impact, the object's flight will be along a parabola if we consider only gravity and ignore air effects such as drag and the Magnus. Let the time  $t = 0$  correspond to the moment right after the impact, and  $g$  be the gravitational acceleration. Let the subscripts  $x, y, z$  denote the corresponding components in the world frame  $\mathcal{F}_w$ . Then

$$\begin{pmatrix} V_{ox}^+ \\ V_{oy}^+ \\ V_{oz}^+ \end{pmatrix} t + \begin{pmatrix} 0 \\ 0 \\ -\frac{1}{2}g \end{pmatrix} t^2 = Q - O := \begin{pmatrix} \alpha_x \\ \alpha_y \\ \alpha_z \end{pmatrix}, \quad (4.10)$$

which, after elimination of  $t$ , leads to

$$\begin{cases} V_{oy}^+ = \alpha_y V_{ox}^+ / \alpha_x, \\ V_{oz}^+ = \left( \alpha_z + \frac{1}{2}g \left( \frac{\alpha_x}{V_{ox}^+} \right)^2 \right) V_{ox}^+ / \alpha_x. \end{cases} \quad (4.11)$$

Expand the first equation in (4.1)

$$\begin{pmatrix} V_{ox}^+ \\ V_{oy}^+ \\ V_{oz}^+ \end{pmatrix} = \begin{pmatrix} V_{ox}^- \\ V_{oy}^- \\ V_{oz}^- \end{pmatrix} + \frac{1}{m_o} \begin{pmatrix} I_x \\ I_y \\ I_z \end{pmatrix}. \quad (4.12)$$

Without loss of generality, we assume the target to be on the right hand side. Thus,  $\alpha_x > 0$  and  $V_{ox}^+ > 0$ . Obtain  $I_y$  and  $I_z$  in terms of  $I_x$ :

$$\begin{cases} I_y &= (\alpha_y I_x + \alpha_y m_o V_{ox}^- - \alpha_x m_o V_{oy}^-) / \alpha_x, \\ I_z &= \frac{2\alpha_z (I_x + m_o V_{ox}^-)^2 + \alpha_x m_o (\alpha_x g m_o - 2(I_x + m_o V_{ox}^-) V_{oz}^-)}{2\alpha_x (I_x + m_o V_{ox}^-)}. \end{cases} \quad (4.13)$$

**Proposition 8** *All the impulses satisfying the constraints (4.13) form a quadratic plane curve.*

**Proof** To show that the curve is 2D, we arbitrarily pick any 4 different points on the curve, namely  $P_1 = (I_{x_1}, I_y(I_{x_1}), I_z(I_{x_1}))$ ,  $P_2 = (I_{x_2}, I_y(I_{x_2}), I_z(I_{x_2}))$ ,  $\dots$ ,  $P_4 = (I_{x_4}, I_y(I_{x_4}), I_z(I_{x_4}))$ , and establish the proposition by verifying  $(\overrightarrow{P_1 P_2} \times \overrightarrow{P_1 P_3}) \cdot \overrightarrow{P_1 P_4} = 0$ . The steps are rather mechanical and thus skipped.  $\square$

We denote the plane curve (4.13) by  $\alpha$  and refer to it as the *impulse solution curve*. For the batting task in Fig. 4.1, the solution impulse curve is  $(I_x, -0.573171 - 0.0268293I_x, (24.2369 + 1.35122I_x - 0.47561I_x^2)/(-1.0 + I_x))$ .

## 4.4 Finding an Initial Contact Velocity

The total impulse has a closed form when the initial sliding velocity  $\gamma_{yz}^-$  is along an invariant direction. This would simplify the planning problem to one of solving linear and quadratic equations with a case-by-case analysis. We will start with an effort to find such a solution. In case the effort fails, we will employ an iterative algorithm that relies on trajectory bounding.

### 4.4.1 Cone of Impulses from Sticking and Straight Sliding

As discussed earlier, all the impulses to achieve the batting task constitute a quadratic curve described by (4.13). Planning is successful as long as we can construct  $\mathbf{v}^-$  such that the total impulse  $\mathbf{I}(\mathbf{v}^-)$  lies on this curve. We would like to first understand what impulses can be generated by  $\mathbf{v}^-$  if its tangential component  $\gamma_{yz}^-$  assumes an invariant direction.

**Theorem 9** *All the possible impulses that can be generated by some  $\mathbf{v}^-$  with  $\gamma_{yz}^-$  in an invariant direction form a cone  $\mathcal{C}$  positively spanned by the vectors  $\delta$  and  $\sigma$  defined in (4.5) and (4.6), respectively. The cone  $\mathcal{C}$  thus generated is referred to as the impulse cone of straight sliding.*

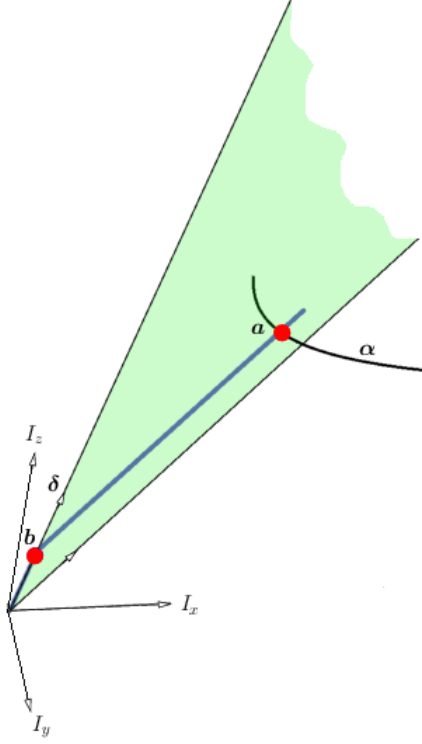


Figure 4.2: The 2D cone contains all the total impulses that can be generated by  $\mathbf{v}^-$  when its tangential component is in one invariant direction for the impact configuration in Fig. 4.1. Here,  $\boldsymbol{\delta} = (0.644738, -0.232654, 0.883281)^T$  and  $\boldsymbol{\sigma} = (0.775021, -0.0875276, 0.657624)^T$ .

**Proof** Suppose  $\gamma_{yz}^-$  is in an invariant direction. From the analysis in Section 4.2, then the sliding velocity  $\gamma_{yz}$  maintains that direction until it becomes zero (only possible if the direction is centripetal). Afterward, it will either stay zero or take on the unique centrifugal direction. As a result, the impulse  $\mathbf{I}$  accumulates along either one line segment (in the direction of  $\boldsymbol{\delta}$  or  $\boldsymbol{\sigma}$ ) or two line segments (in the directions of  $\boldsymbol{\delta}$  and  $\boldsymbol{\sigma}$ , sequentially). The ending point of the impulse accumulation, representing the total impulse generated by the impact, is therefore positively spanned by  $\boldsymbol{\delta}$  and  $\boldsymbol{\sigma}$ .

That  $\mathbf{I}$  accumulates in only one direction happens in exactly one of the following three situations: a)  $\gamma_{yz}^- = \mathbf{0}$ ; b)  $\gamma_{yz} \neq \mathbf{0}$  throughout the impact; and c)  $\gamma_{yz}^- \neq \mathbf{0}$  but  $\gamma_{yz} = \mathbf{0}$  later on, and  $\boldsymbol{\sigma} \times \boldsymbol{\delta} = \mathbf{0}$ . □

#### 4.4.2 Solution Contact Velocity in an Invariant Direction

Following Theorem 9, if the solution impulse curve  $\boldsymbol{\alpha}$  intersects the impulse cone  $\mathcal{C}$  of impulses from sticking and straight sliding, then the intersection point  $\boldsymbol{a}$  is a total impulse that can accomplish the batting task. See Fig. 4.2.

The cone  $\mathcal{C}$  contains the origin, since impulse always starts accumulating from zero. The vector  $\boldsymbol{N} = \boldsymbol{\delta} \times \boldsymbol{\sigma} = (N_x, N_y, N_z)^T$  is normal to the plane containing  $\mathcal{C}$ . To determine  $\boldsymbol{a}$ , substitute  $\boldsymbol{I} = (I_x, I_y, I_z)$ , where  $I_y$  and  $I_z$  are given by (4.13), into  $\boldsymbol{I}^T \boldsymbol{N} = 0$ , and solve the resulting quadratic equation in  $I_x$ .

The found solution  $\boldsymbol{a}$  is uniquely written as  $\boldsymbol{a} = t_1 \boldsymbol{\delta} + t_2 \boldsymbol{\sigma}$ ,  $t_1, t_2 \geq 0$ . Solve the following system of equations for  $t_1$  and  $t_2$ :

$$\begin{aligned} (\boldsymbol{\delta}^T \boldsymbol{\delta})t_1 + (\boldsymbol{\delta}^T \boldsymbol{\sigma})t_2 &= \boldsymbol{\delta}^T \boldsymbol{a}, \\ (\boldsymbol{\sigma}^T \boldsymbol{\delta})t_1 + (\boldsymbol{\sigma}^T \boldsymbol{\sigma})t_2 &= \boldsymbol{\sigma}^T \boldsymbol{a}. \end{aligned}$$

The point  $\boldsymbol{b} = t_1 \boldsymbol{\delta}$  represents the impulse value at the end of the initial sliding during the same impact that generates the total impulse  $\boldsymbol{a}$ .

Let  $\hat{\boldsymbol{s}} = (s_u, s_w)^T$  be one of the invariant directions solved from (4.8) in the local frame  $\mathcal{F}_c$ . The initial contact velocity along this invariant direction can be expressed as

$$\boldsymbol{v}^- = R(\rho s_u, \rho s_w, v_n^-)^T \quad (4.14)$$

in the world frame  $\mathcal{F}_w$ , with two unknowns  $\rho$  and  $v_n^-$ .

#### 4.4.3 Closed-Form Solution

The initial sliding velocity  $\gamma_{yz}^- = \rho(s_u, s_w)^T$  affects if and when  $\gamma_{yz}$  will decrease to zero, thus the location of  $\boldsymbol{b}$  on the ray in the direction of  $\boldsymbol{\delta}$ . The initial normal contact velocity  $v_n^-$  affects how long the impact will last, and thus, where  $\boldsymbol{a}$  is from  $\boldsymbol{b}$  in the direction of  $\boldsymbol{\sigma}$ . The impulse values  $\boldsymbol{a}$  and  $\boldsymbol{b}$  are found in Section 4.4.2. Write  $a_n = \hat{\boldsymbol{n}}^T \boldsymbol{a}$  and  $b_n = \hat{\boldsymbol{n}}^T \boldsymbol{b}$ . Two steps below will be carried out to determine  $\rho$  and  $v_n^-$ .

**Step 1** Solve for  $\rho$ . From (4.9),

$$\begin{aligned}\gamma_{yz}(I_n) &= \rho(s_u, s_w)^T + \lambda I_n(s_u, s_w)^T \\ &= (\rho + \lambda I_n)(s_u, s_w)^T.\end{aligned}$$

At the impulse value  $\mathbf{b}$ ,  $\gamma_{yz}(I_n) = \mathbf{0}$ . This implies  $\rho = -\lambda b_n = -\lambda t_1$ , where  $\lambda$  is easily evaluated from (4.7).

**Step 2** Solve for  $v_n^-$ . The idea is to express the energy  $E$  in terms of  $v_n$  in a closed form, via integrating (4.4) and accounting for the loss by the factor of  $1 - e^2$  at the end of compression. Solve  $E(v_n^-) = 0$ , which holds at the end of restitution for  $v_n^-$ . Below we will apply the analysis given in Jia and Wang (2017) for closed form computation of  $v_n^-$ .

**Case 1** The final impulse  $\mathbf{a}$  is inside the cone  $\mathcal{C}$  as shown in Fig. 4.2.

**Case 1a** Compression finishes before sliding ends. Integrate (4.4) to yield the energy function

$$\Phi_1(v_n^-, I_n) = -v_n^- I_n - \frac{1}{2m_\delta} I_n^2, \quad (4.15)$$

where  $m_\delta = (\frac{1}{m_1} + \frac{1}{m_2} - \hat{\mathbf{n}}^T S \boldsymbol{\delta})^{-1}$ . Solve  $E'(v_n^-) = 0$  to obtain the normal impulse  $\zeta_c$  and energy at the end of compression:

$$\begin{aligned}\zeta_c(v_n^-) &= -v_n^- m_\delta, \\ E_c(v_n^-) &= \Phi_1(v_n^-, \zeta_c(v_n^-)).\end{aligned} \quad (4.16)$$

Apply the energy loss by multiplying  $E_c(v_n^-)$  with  $e^2$ , where  $e$  is the coefficient of restitution. The energy during restitution has the form

$$E_r(v_n^-) = e^2 E_c(v_n^-) + \Phi_1(v_n^-, a_n) - \Phi_1(v_n^-, \zeta_c(v_n^-)).$$

Setting  $E_r(v_n^-) = 0$ , we solve for  $v_n^-$ . There are at most two real roots. Throw away the positive root, since the two objects cannot penetrate into each other during the impact. If there is still one root left, check if the condition

$$0 \leq \zeta_c(v_n^-) \leq b_n \quad (4.17)$$

holds to satisfy the precedence of compression to restitution. If not, disregard this root, and move on to case 1b to continue the checking. If yes, the value of  $v_n^-$  is found. Together with  $\rho$  computed earlier, the initial contact velocity is  $\mathbf{v}^-$  is determined.

**Case 1b** Compression finishes after sliding ends. During the sliding, the energy function is  $\Phi_1$  given in (4.15). The energy accumulated during sliding is

$$E_s(v_n^-) = \Phi_1(v_n^-, b_n).$$

After the contact mode turns into stick or resumed slip, it assumes a new form:

$$\Phi_2(v_n^-, I_n) = (-v_n^- + \hat{\mathbf{n}}^T S(\mathbf{b} - b_n \boldsymbol{\sigma})) I_n - \frac{1}{2m_\sigma} I_n^2,$$

where  $m_\sigma = (\frac{1}{m_1} + \frac{1}{m_2} - \hat{\mathbf{n}}^T S \boldsymbol{\sigma})^{-1}$ . The normal impulse and energy at the end of compression are

$$\begin{aligned} I_{nc}(v_n^-) &= m_\sigma (-v_n^- + \hat{\mathbf{n}}^- S(\mathbf{b} - b_n \boldsymbol{\sigma})), \\ E_c(v_n^-) &= E_s(v_n^-) + \Phi_2(v_n^-, I_{nc}(v_n^-)) - \Phi_2(b_n, v_n^-). \end{aligned} \quad (4.18)$$

The energy during the restitution is expressed as

$$E_r(v_n^-) = e^2 E_c(v_n^-) + \Phi_2(v_n^-, a_n) - \Phi_2(I_{nc}(v_n^-)).$$

Set  $E_r(v_n^-) = 0$  to solve for  $v_n^-$ . There are at most two real roots. Again, throw away any positive root to disallow penetration. If there is still one root left, plug into (4.18) and check if the following condition

$$b_n \leq I_{nc}(v_n^-) \leq a_n \quad (4.19)$$

holds. If not, disregard this root, and use a numerical method to be presented later. If yes, the value of  $v_n^-$  is found successfully, so is the initial velocity  $\mathbf{v}^-$  given in (4.14) to achieve the batting task.

**Case 2** The point  $\mathbf{a}$  lies on the ray from the origin and in the direction of  $\boldsymbol{\delta}$ . Namely,  $\mathbf{a} = \mathbf{b}$ . This case can be solved exactly the same as **Case 1a**.

**Case 3** The point  $\mathbf{a}$  lies on the ray from the origin and in the direction of  $\boldsymbol{\sigma}$ . Namely,  $\mathbf{b}$  is at the origin. This case can be solved exactly the same as **Case 1b**, under the condition  $\mathbf{b} = \mathbf{0}$ .

---

**Algorithm 4** Closed-form computation of initial contact velocity
 

---

**Input:** roots  $\hat{\mathbf{s}}_1, \hat{\mathbf{s}}_2, \dots, \hat{\mathbf{s}}_n$ ,  $n \leq 4$ , of (4.8)

- 1: construct the solution impulse curve  $\alpha$  according to (4.13)
  - 2: **for** each  $\hat{\mathbf{s}}_k$  **do**
  - 3:   **if**  $\delta \times \sigma \neq \mathbf{0}$  **then**
  - 4:     compute  $\delta$  according to (4.5)
  - 5:     compute  $\sigma$  according to (4.6)
  - 6:     obtain the cone  $\mathcal{C}$  spanned by  $\delta$  and  $\sigma$
  - 7:     intersect  $\alpha$  and  $\mathcal{C}$  as described in Section 4.4.2
  - 8:     **for** each found intersection  $\beta_k$  **do**
  - 9:        $\mathbf{a} \leftarrow \beta_k$
  - 10:       (Case 1a) obtain the roots for  $v_n^-$
  - 11:       **if** one such root satisfies (4.17) **then**
  - 12:         **return**  $\rho$  and  $v_n^-$  computed in Section 4.4.3
  - 13:       **end if**
  - 14:       (Case 1b) obtain the roots for  $v_n^-$
  - 15:       **if** one such root satisfies (4.19) **then**
  - 16:         **return**  $\rho$  and  $v_n^-$  computed in Section 4.4.3
  - 17:       **end if**
  - 18:       **if**  $\mathbf{a} \times \delta = \mathbf{0}$  **then**
  - 19:         repeat the **if** statement of lines 11–13
  - 20:       **else if**  $\mathbf{a} \times \sigma = \mathbf{0}$  **then**
  - 21:         repeat the **if** statement of lines 15–17
  - 22:       **end if**
  - 23:     **end for**
  - 24:   **else**
  - 25:     intersect  $\mathcal{C}$  with the ray from the origin and in the direction of  $\delta$
  - 26:     **for** each intersection repeat the **if** statement of lines 18–22
  - 27:   **end if**
  - 28: **end for**
-

Algorithm 4 finds a closed form solution whenever it exists. There is no solution when the curve  $\alpha$  lies outside all the cones defined by the invariant directions of the impact instance. An example is given in Fig. 4.3 for the same impact configuration in Fig. 4.1 but a different destination point.

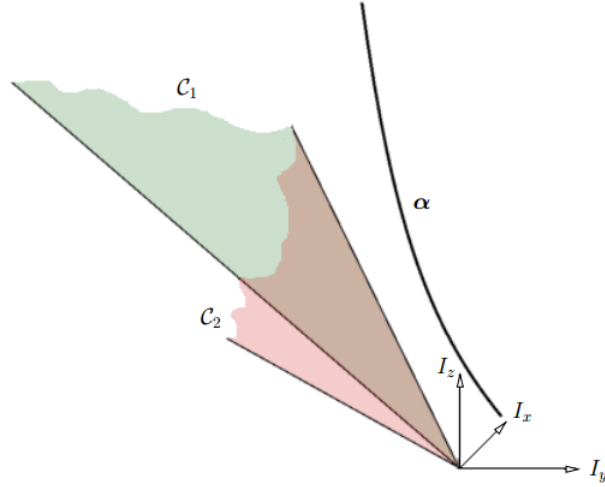


Figure 4.3: Solution impulse curve  $(I_x, -0.686376 + 0.0863761I_x, (21.9385 + 1.62241I_x - 0.611205I_x^2)/(-1 + I_x))$  for  $Q = (5, 0.342052, -2.53565)^T$  lies outside the cones  $\mathcal{C}_1$  and  $\mathcal{C}_2$  defined by only two invariant directions for the impact configuration in Fig. 4.1. The shared edge by  $\mathcal{C}_1$  and  $\mathcal{C}_2$  has the direction  $\sigma = (0.76538, -0.0959546, 0.674322)^T$ . The second edges of the two cones are in the directions  $(0.645227, -0.234504, 0.882434)^T$  and  $(1.10631, -0.138026, 0.0838131)^T$ , which are different values assumed by  $\delta$ .

#### 4.4.4 Bounding Triangle Method

When Algorithm 4 finds no solution, the batting task cannot be achieved by a  $\mathbf{v}^-$  whose tangential component is in an invariant direction. In such a case, we use a numerical method based on the (assumed) continuity of the impulse function  $\mathbf{I}(\mathbf{v}^-)$  describing the physical impact process.

We guess a value  $\mathbf{v}^{-(0)}$  of  $\mathbf{v}^-$ , and set up a projection plane  $\Pi$  to contain the target  $Q$  and perpendicular to  $OQ$ . The object's post-impact flying trajectory will have an intersection  $P$  with this plane. The steps that lead to this projection are illustrated by the diagram in Fig. 4.4. An example is shown in Fig. 4.5. There are three consecutive mappings: from  $\mathbf{v}^-$



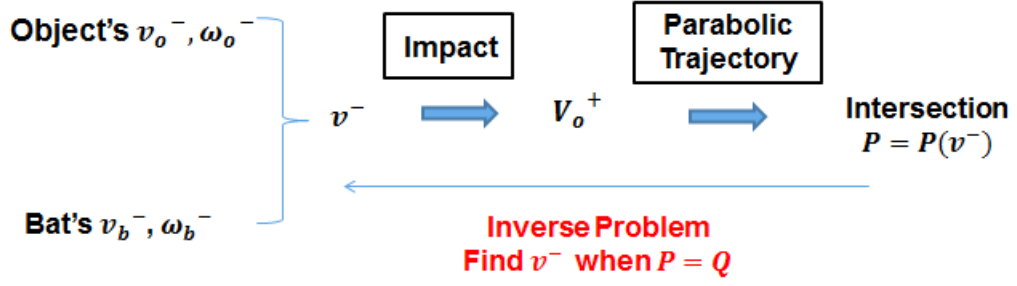


Figure 4.4: Relationship between  $v^-$  and the projection on the plane.

to the impulse  $I$ , from  $I$  to the flight trajectory  $\mathcal{T}$ , and from  $\mathcal{T}$  to its intersection  $P$  with the projection plane  $\Pi$ . Their composite mapping is highly nonlinear that no closed form solution can be derived based on the position of  $Q$  within the bounding triangle in  $\mathcal{P}$ .

Thus, an iterative method is considered. We hypothesize that if  $Q$  is contained in the triangle formed by the intersections of three trajectories with the plane, then a solution value of  $v^-$  is contained in the triangle defined by the values of  $v^-$  generating these trajectories.

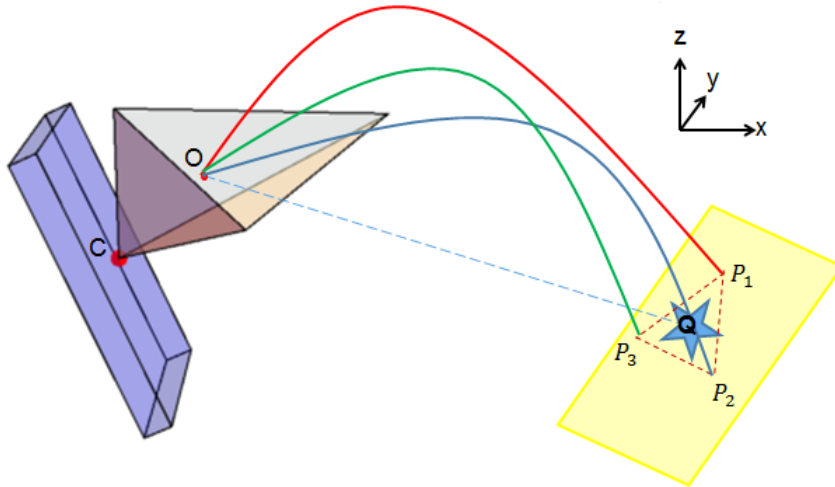


Figure 4.5: Projection plane and bounding box demonstration.

First, find three initial contact velocities  $\mathbf{v}_1^{-(0)}$ ,  $\mathbf{v}_2^{-(0)}$ ,  $\mathbf{v}_3^{-(0)}$  such that the projection  $\triangle P_1^{(0)}P_2^{(0)}P_3^{(0)}$  bounds the target  $Q$ . Then, update the initial contact velocity guesses to shrink the triangle to  $Q$ .

#### 4.4.4.1 Initialization

The goal is to find three values  $\mathbf{v}_1^-$ ,  $\mathbf{v}_2^-$ , and  $\mathbf{v}_3^-$  of  $\mathbf{v}^-$  such that  $\triangle P_1 P_2 P_3$  bounds the target  $Q$ , where  $P_1 = P(\mathbf{v}_1^-)$ ,  $P_2 = P(\mathbf{v}_2^-)$ , and  $P_3 = P(\mathbf{v}_3^-)$ . Start with three random guesses, repeatedly update one of the guesses based on which edge of  $\triangle P_1 P_2 P_3$  is closer to the target, until the projected triangle completely bounds the target  $Q$ . This is detailed in Algorithm 5.

---

#### Algorithm 5 Bounding Triangle Initialization for $\mathbf{v}^-$

---

- 1: take three random guesses  $\mathbf{v}_1^-$ ,  $\mathbf{v}_2^-$ , and  $\mathbf{v}_3^-$
  - 2: apply the impact algorithm in Jia and Wang (2017) to compute their generated impulses  $\mathbf{I}_1$ ,  $\mathbf{I}_2$ , and  $\mathbf{I}_3$
  - 3: **for** each  $\mathbf{I}_k$  **do**
  - 4: obtain the object's post-impact velocity  $\mathbf{V}_o^+$  according to (4.1)
  - 5: construct its post-impact trajectory
  - 6: compute its intersection  $P_k$  with the project plane  $\Pi$
  - 7: **end for**
  - 8: **while**  $Q \notin \triangle P_1 P_2 P_3$  **do**
  - 9: let  $\overline{P_i P_j}$  be the closest edge to  $Q$
  - 10:  $P_k$ ,  $k \neq i, j$ , must be on the edge's other side
  - 11: in the plane containing  $\mathbf{v}_1^-$ ,  $\mathbf{v}_2^-$ , and  $\mathbf{v}_3^-$ , pick a new  $\mathbf{v}_k^-$  to be on the opposite side of  $\overline{\mathbf{v}_i^- \mathbf{v}_j^-}$  to the current  $\mathbf{v}_k^-$
  - 12: recompute  $P_k$
  - 13: **end while**
  - 14: **return**  $\mathbf{v}_1^-$ ,  $\mathbf{v}_2^-$ , and  $\mathbf{v}_3^-$
- 

Once  $\mathbf{v}_1^-$ ,  $\mathbf{v}_2^-$ , and  $\mathbf{v}_3^-$  are obtained, iteratively one of them will be replaced by either their centroid or the midpoint of two of them, until one of the projected point  $P(\mathbf{v}_i^-)$ ,  $i \in \{1, 2, 3\}$  is close enough to the target  $Q$ .

#### 4.4.4.2 Centroid-based Update

In the current iteration,  $\mathbf{v}_1^{-(i)}$ ,  $\mathbf{v}_2^{-(i)}$ ,  $\mathbf{v}_3^{-(i)}$  have their projection triangle  $P_1 P_2 P_3$  containing  $Q$ . Always set  $\mathbf{v}_4^{-(i)} = \frac{1}{3} (\mathbf{v}_1^{-(i)} + \mathbf{v}_2^{-(i)} + \mathbf{v}_3^{-(i)})$ . The projection  $P_4$  of  $\mathbf{v}_4^{-(i)}$  splits the triangle into three subtriangles, as shown in Fig. 4.6. We determine the subtriangle containing  $Q$ , and use  $\mathbf{v}_4^{-(i)}$  to replace  $\mathbf{v}_k^{-(i)}$ , where  $P_k$  is not a vertex of the subtriangle. In Fig. 4.6, since  $\triangle P_2 P_3 P_4$  contains  $Q$ , the next iteration will begin with obtain  $\mathbf{v}_1^{-(i+1)} = \mathbf{v}_4^{-(i)}$ ,  $\mathbf{v}_2^{-(i+1)} = \mathbf{v}_2^{-(i)}$ ,  $\mathbf{v}_3^{-(i+1)} = \mathbf{v}_3^{-(i)}$ .

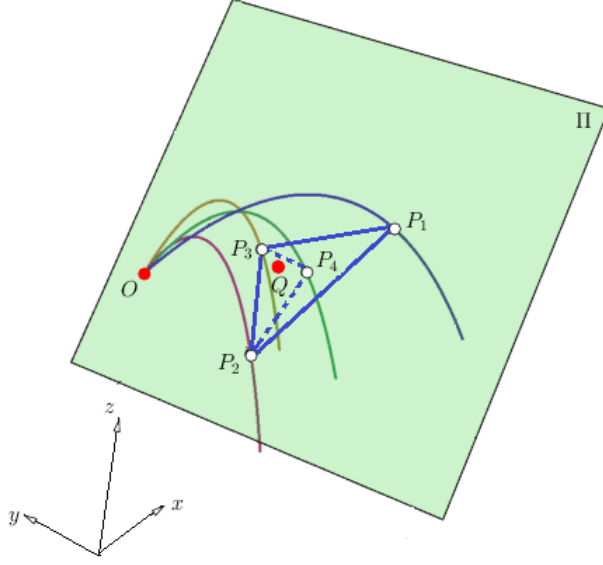


Figure 4.6: Centroid-based updates over trajectories in order to pass through  $Q$ .

#### 4.4.4.3 Midpoint-based Update

Repeated centroid-based updates could make the projection triangle too slim to contain  $Q$ . We can prevent such degeneration using the midpoint of two of  $\mathbf{v}_1^{-(i)}$ ,  $\mathbf{v}_2^{-(i)}$ ,  $\mathbf{v}_3^{-(i)}$  and  $\mathbf{v}_4^{-(i)}$ . At one iteration, suppose that the initial contact velocities  $\mathbf{v}_1^{-(i)}$ ,  $\mathbf{v}_2^{-(i)}$ ,  $\mathbf{v}_3^{-(i)}$  and  $\mathbf{v}_4^{-(i)}$  lead to the projection triangle  $P_1P_2P_3$  and point  $P_4$  ( $P_4$  may not necessarily lie on one of the edges due to the non-linearity of impact mapping). More specifically, suppose  $Q$  is in the projection new subtriangle  $\triangle P_iP_jP_k$ , and  $P_h$  is the only other vertex. Let  $\mathbf{v}_h^{-(i+1)} = \mathbf{v}_4^{-(i)}$ . In  $\triangle P_iP_jP_k$ , identify the farthest vertex, say,  $P_j$ , from  $Q$ . Between the two edges incident on  $P_j$ , choose the one closer one to  $Q$ , say  $P_jP_k$ . Then update  $\mathbf{v}_4^{-(i+1)}$  as midpoint of  $\mathbf{v}_j^{-(i+1)}$  and  $\mathbf{v}_k^{-(i+1)}$ .

Fig. 4.7 shows an example, using the same instance and initial guesses as Fig. 4.6. The target  $Q$  is contained in  $\triangle P_1P_3P_4$ . It turns out that  $P_1$  is the farthest vertex from  $Q$  in this subtriangle, and of its two incident edges,  $\overline{P_1P_3}$  is closer to  $Q$  than  $\overline{P_1P_4}$ . Thus, in the next iteration, let  $\mathbf{v}_1^{-(i+1)} = \mathbf{v}_1^{-(i)}$ ,  $\mathbf{v}_2^{-(i+1)} = \mathbf{v}_4^{-(i)}$ ,  $\mathbf{v}_3^{-(i+1)} = \mathbf{v}_3^{-(i)}$ , and  $\mathbf{v}_4^{-(i+1)} = \frac{1}{2}(\mathbf{v}_1^{-(i+1)} + \mathbf{v}_3^{-(i+1)})$ .

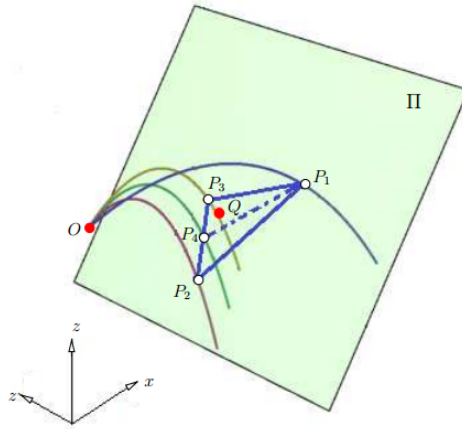


Figure 4.7: Midpoint-based updates over trajectories in order to pass through  $Q$ .

## 4.5 Simulation Results

### 4.5.1 Comparisons Among Three Algorithms

The batting configuration shown in Fig. 4.1 with given parameters can be solved using Algorithm 4 and the numerical method (centroid/midpoint). Fig. 4.2 shows the existence of a closed-form solution. Fig. 4.8 displays several iterations of the bounding triangle method using centroid-based updates.

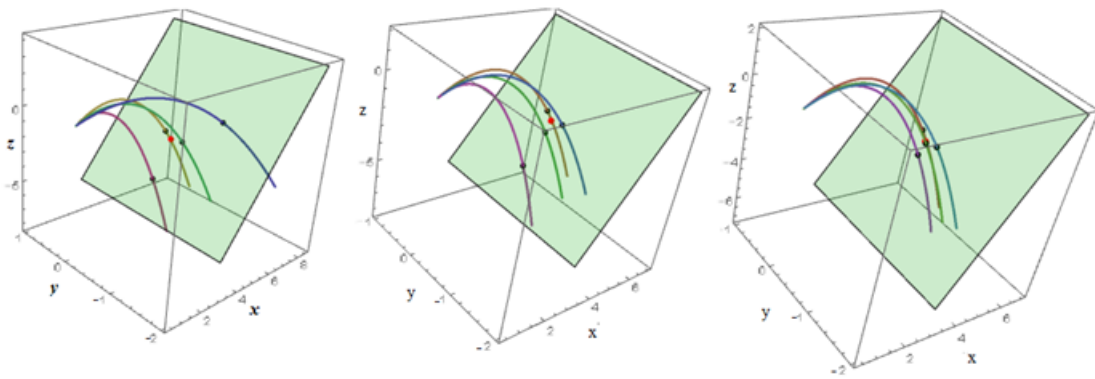


Figure 4.8: Centroid algorithm iterations.

The performances of Algorithm 4 and the bounding triangle method (with two types of updates) are compared in Table 4.1. The computed results of initial contact velocities are

$(-5.3166, 0.6038, -4.3826)^T$ ,  $(-5.1451, 0.6370, -4.3476)^T$ ,  $(-5.1405, 0.6475, -4.3463)^T$  respectively. Both versions of the bounding triangle method used the same initialized contact velocity with values  $(-6.1782, 4.8004, -5.2990)^T$ ,  $(-3.3301, 2.0125, -4.2320)^T$ ,  $(-5.0622, 1.0023, -5.2320)^T$ .

Table 4.1: Comparison among the three different algorithms.

	closed form	centroid	mid point
# rounds	—	3	5
running time (s)	0.00000156	2.18	4.00285
error dist from $Q$ to solution	0	0.15	0.15

From the table, it is not hard to see that Algorithm 4 has the best performance (provided a closed-form solution exists). It takes almost no time to compute and also gives the exact solution without error. The actual total running times for centroid-based and midpoint-based updates are longer than listed in the table, which does not include the time for initialization. The bounding triangle initialization is quite tricky, due to random guessing and the nonlinearity of the projection. In reality, the time for initialization can range from a split second to many seconds or even longer.

#### 4.5.2 Success Rate

To gauge how likely an closed-form solution exists, we have generated 10 random target points in the plane of  $x = 5$ ,  $-4 \leq y \leq 4$  and  $-4 \leq z \leq 4$  as shown in Fig. 4.9. The figure also shows the solved flying trajectories to reach these points. The three blue trajectories are found in closed forms. The six green trajectories are found numerically with distances up to 0.15 from  $Q = (5, -0.2, -2)$ . (Note that the target is at a distance around 5 from the position  $O$  of the object’s center of mass at the time of batting.) The black trajectory is the situation when bounding triangle algorithm does not converge. We changed to a bigger error 0.85 in order to return a solution in this case. This could be caused by the non-linearity of impact. For example, at one iteration step, the centroid/midpoint guess can no long lead to the projection inside the bounding triangle, and the algorithm could not converge after that.

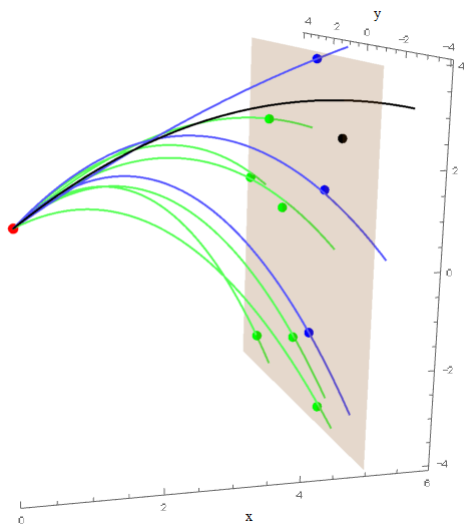


Figure 4.9: Finding solutions of 10 random target points.

In summary, closed form solution exists for 3 out of 10 instances, and solutions are found for 9 out of 10 within the small error of 0.15 either exactly or numerically.

## 4.6 Discussion and Future Work

A feasible value of  $\mathbf{v}^-$  in closed form, whenever exists, can be found much more efficiently by Algorithm 4 than by the bounding triangle method. Further investigation is needed to understand the conditions under which Algorithm 4 succeeds, that is, straight slip or stick happens at the contact during a success batting action. If Algorithm 4 fails, we need to know how to change the batting configuration to generate a closed-form solution. In other words, how to rotate or translate the robot bat to make sure the impulse constraint curve would have intersections with impulse cone of straight sliding.

For example, when rotating the bat, we observe that the two impulse cones sweeping out a big volume as shown in Fig. 4.10. It would be interesting to continue studying how to rotate the bat or change the initial configuration, such that the constraint impulse curve would have intersections with the impulse cones. In other words, when closed form solution exists.

The bounding triangle method can be slow, and it fails sometimes, Even though this numerical method works most of the time, a more robust and efficient numerical algorithm will

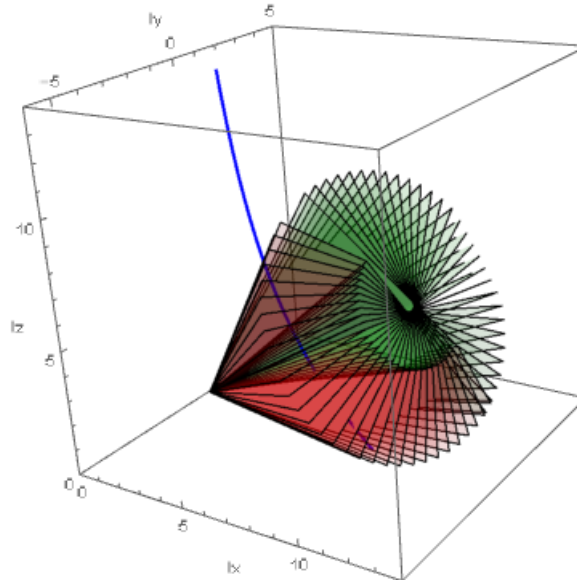


Figure 4.10: When rotating the bat, the volume swept out by the impulse cones.

be needed as a backup in case a closed-form solution does not exist.

Suppose a value of  $\mathbf{v}^-$  is found to carry out the task. By (4.2), the pre-impact bat motions  $(\mathbf{V}^-, \boldsymbol{\omega}^-)$  generating  $\mathbf{v}^-$  form a three-dimensional set. Which motion to use is subject to many factors including, to name a few, easiness to realize, energy consumption, time and kinematic constraints, etc.

The co-author's team has made significant progress, both algorithmically and experimentally (with a WAM arm), on batting objects flying in the vertical plane. This can be viewed as a 2D version of the problem. The next step is to realize batting in 3D, drawing upon the work reported in this paper.

## CHAPTER 5. EXPLICIT SOLUTIONS AND COEFFICIENT OF RESTITUTION FOR AN ELASTIC ROD WITH VISCOUS DAMPING

A damped one-dimensional wave equation is used to model an elastic rod that bounces off the ground with a given initial velocity, under the influence of gravity. An explicit solution is derived, based on the Method of Descent and D'Alembert's formula. The time of contact with the ground is determined in terms of the initial velocity, damping coefficient and gravitational constant. We obtain expressions for the motion of the center of mass for the duration of the impact and are able to determine the internal vibrational energy present at the end of the contact time. A corresponding definition of a "coefficient of restitution" is proposed and analyzed.

### 5.1 Introduction

The classical problem of determining the height of rebound of a bouncing object has been investigated in a huge number of works going back Newton (1687) who defined the *coefficient of restitution* (COR) as a ratio of relative velocities after and before a collision, Hertz (1882), who developed the foundations of contact mechanics (see e.g., Johnson and Johnson (1987)) based on stresses in spherical elastic bodies, and Love (1905) who investigated the dynamics of colliding elastic rods governed by one-dimensional wave equations.

Although there are numerous applications where impact problems are studied; e.g., sports science, robotics and earthquake dynamics (see e.g., Cross (2009), Jia et al. (2009), Liu et al. (2007), Walker (1994), Wang and Mason (1987), Wang et al. (2015), Zhang et al. (2014), Lipscombe and Pellegrino (1993)), there are very few situations where a precise knowledge of motion during the impact has been determined. Consequently in most applications, an impact



is modeled using a COR. While this methodology has become quite developed, (see e.g., Stronge Stronge (2004a) for a detailed description of various theories of COR and application), there are numerous drawbacks and inconsistencies with this approach, some of which are described in Stewart (2000).

A COR less than 1 describes an inelastic collision, and hence describes some amount of dissipation (at least in terms of velocity) that occurs during the impact. It has long been thought Stewart (2000) that dissipation during an impact results from 1) localized plastic deformation; 2) viscous damping in the material; and 3) energy transfer to vibrational energy. Therefore a better knowledge (even in specialized situations) of the portion of translational kinetic energy that is transferred to vibrational energy during the impact, could improve how the COR approach is applied.

One situation where it is possible to write down an explicit solution formula (see e.g., Love Love (1905)) for an impact is the one-dimensional elastic rod

$$\rho v_{tt} - \sigma v_{xx} = f. \quad (5.1)$$

In the above,  $u(x, t)$  is the longitudinal displacement at position  $x$  and time  $t$ ;  $f$  is an external applied force,  $\rho$  is the linear density, and  $\sigma$  is the longitudinal elastic modulus.

The main motivation of this paper is to determine for an elastic rod, possibly a viscous damping term as in (C.1) below, the proportion of vibrational energy in the elastic rod at the end of the impact.

Some results in this direction were obtained by Shi (1998a) who considered the impact of an elastic rod dropped from a specific height to a rigid foundation, and determined the time of impact and rebound velocity of the bottom of the rod. He also obtained a formula for a COR based on the change in velocity of the bottom of the rod.

Here we consider the following constant coefficient elastic rod with viscous damping:

$$v_{tt} + 2rv_t - c^2 v_{xx} = -g \quad x \in \Omega_L := (0, L), \quad t \in (0, +\infty), \quad (5.2)$$

where in comparison to (5.1), we have divided the equation by  $\rho$  so that  $g \geq 0$  is proportional to the gravitational constant, and the wave speed  $c = \sqrt{\frac{\sigma}{\rho}}$  is positive. The viscous damping term  $2rv_t$  ( $r \geq 0$ ) describes a frictional force proportional to the velocity.

The rod is assumed to be stress-free at the end  $x = L$  and we impose Signorini boundary conditions at the end  $x = 0$ :

$$v_x(L, t) = 0, \quad t \in (0, +\infty), \quad (5.3)$$

$$v_x(0, t) \leq 0, \quad t \in (0, +\infty), \quad (5.4)$$

$$v(0, t) \geq 0, \quad t \in (0, +\infty), \quad (5.5)$$

$$v(0, t)v_x(0, t) = 0, \quad t \in (0, +\infty). \quad (5.6)$$

In our formulation of this problem, we assume that the rod impacts the ground at time 0 with constant initial velocity  $-\mu$ :

$$v(x, 0) = 0, \quad x \in \Omega_L, \quad (5.7)$$

$$v_t(x, 0) = -\mu, \quad x \in \Omega_L, \quad (5.8)$$

and with zero displacement from the reference configuration

$$X(x, 0) = x, \quad x \in [0, L],$$

thus the deformed position at time  $t$  is given by

$$X(x, t) = x + v(x, t). \quad (5.9)$$

The Signorini boundary conditions (C.3)–(C.5) (also called unilateral constraints) essentially state that the bottom of the rod should be stress-free while not in contact with the ground and the Dirichlet condition  $v(0, t) = 0$  should be imposed when in contact with the ground.

Signorini problems have been considered in a wide variety of contact problems for plates, beams, strings etc., see e.g., Ahn and Stewart (2009), Shi (1998b), Ahn (2007), and can be expressed as a variational inequality, for which there is a corresponding definition of a weak solution. For the damped problem (C.1)–(C.5), but with general initial conditions of finite energy, Rivera and Oquendo Rivera and Oquendo (1999) proved global existence of weak solutions and obtained asymptotic decay results. Lebeau and Schatzman Lebeau and Schatzman (1984) studied an analogous multidimensional undamped wave equation on a half space, and proved existence and uniqueness of solutions in a suitably defined functions space.

Details of controllability studies in the context of a string equation was considered in Ammar-Khodja et al. (2010).

For the present paper, we only need to consider the time interval  $[0, t_b + \epsilon)$ , where  $[0, t_b]$  is the contact interval and  $\epsilon$  is sufficiently small so that there is at most one bounce. In this situation, solutions are classical except for jumps in the derivatives along certain characteristic rays due to the bounce. Here  $t_b$  (possibly  $= \infty$ ) is defined by

$$t_b = \sup\{t > 0 : v(0, \tau) = 0, \quad 0 \leq \tau < t\}. \quad (5.10)$$

Based on the Method of Descent and D'Alembert's formula, we obtain explicit solution formulas for  $v(x, t)$  over the contact interval  $[0, t_b]$ . The contact time  $t_b$  is determined in terms of a computable formula in Theorem 13. In particular, we show  $t_b \geq t_1 := 2L/c$ . In the case  $r = 0$ , an explicit formula in terms of parameters  $\mu$ ,  $L$ ,  $c$ , and  $g$  for  $t_b$  is derived, which in particular shows that  $t_1 \leq t_b \leq 2t_1$ . We also find expressions for the motion of the center of mass over the time interval  $[0, t_b + \epsilon]$  for small  $\epsilon$ . At the time  $t_b$ , the energy of the elastic rod has an orthogonal decomposition into *translational energy*, corresponding to the motion of the center of mass and *vibrational energy*, corresponding to energy of vibrations. We are able to calculate this decomposition at the time of impact, and define an associated COR based on the ratio of translational energy after and before the collision. Based on this definition of COR, we are able to make some observations about the dependence of internal vibrational energy as a function of the  $\mu$ , the velocity of impact; see Section 4.

## 5.2 Explicit integral representation of solution

During the time interval  $[0, t_b]$ , (C.1)–(C.7) can be written as:

$$\begin{cases} v_{tt} + 2rv_t - c^2v_{xx} = -g, & (x, t) \in \Omega_L \times (0, t_b), \\ v(x, 0) = 0, \quad v_t(x, 0) = -\mu, & x \in \Omega_L, \\ v(0, t) = 0, \quad v_x(L, t) = 0, & t \in (0, t_b). \end{cases} \quad (5.11)$$

It is easy to see that solutions of (C.10) coincide with solutions  $\hat{v}$  of

$$\begin{cases} \hat{v}_{tt} + 2r\hat{v}_t - c^2\hat{v}_{xx} = -g, & (x, t) \in \Omega_{2L} \times (0, t_b), \\ \hat{v}(x, 0) = 0, \hat{v}_t(x, 0) = -\mu, & x \in \Omega_{2L}, \\ \hat{v}(0, t) = 0, \hat{v}(2L, t) = 0, & t \in (0, t_b). \end{cases} \quad (5.12)$$

Setting  $\hat{v}(x, t) = e^{-rt}w(x, t)$  in (5.12) results in

$$\begin{cases} w_{tt} - c^2w_{xx} - r^2w = -ge^{rt}, & (x, t) \in \Omega_{2L} \times (0, t_b), \\ w(x, 0) = 0, w_t(x, 0) = -\mu, & x \in \Omega_{2L}, \\ w(0, t) = 0, w(2L, t) = 0, & t \in (0, t_b). \end{cases} \quad (5.13)$$

We see below that (C.10) can be solved explicitly using the method of descent together with the reflection principle. For a first step, consider the homogeneous problem on the infinite domain:

$$\begin{cases} u_{tt} - c^2u_{xx} - c^2\lambda^2u = 0, & x \in \mathbb{R}, t \in (0, +\infty), \\ u(x, 0) = 0, u_t(x, 0) = \varphi(x). & x \in \mathbb{R}. \end{cases} \quad (5.14)$$

**Lemma 10** *Assume  $\varphi$  is  $C^2$  on  $\mathbb{R}$ . Then the classical solution to (5.14) is given by*

$$u(x, t) = \frac{1}{2c} \int_{x-ct}^{x+ct} I_0(\lambda s) \varphi(y) dy, \quad (5.15)$$

where  $s = \sqrt{c^2t^2 - (x - y)^2}$  and

$$I_0(z) = \frac{2}{\pi} \int_0^{\pi/2} \cosh(z \sin \theta) d\theta, \quad (5.16)$$

is the modified Bessel function of the second kind.

**Proof:** We apply the “method of descent”; see e.g., John (1982). Let  $u$  be the solution of (5.14) and define  $\hat{u}(x_1, x_2, t) = \cosh(\lambda x_2)u(x_1, t)$ . Then it is easy to verify that

$$\begin{cases} \hat{u}_{tt} - c^2(\hat{u}_{x_1x_1} + \hat{u}_{x_2x_2}) = 0 & x_1, x_2 \in \mathbb{R}, t \in (0, +\infty), \\ \hat{u}(x_1, x_2, 0) = 0, \hat{u}_t(x_1, x_2, 0) = \cosh(\lambda x_2)\varphi(x_1), & x_1, x_2 \in \mathbb{R}. \end{cases} \quad (5.17)$$

On the other hand  $\hat{u}$  is also given by the spherical means formula

$$\hat{u}(x_1, x_2, t) = \frac{1}{2\pi c} \iint_{r < ct} \frac{\cosh(\lambda y_2)\varphi(y_1)}{\sqrt{c^2t^2 - r^2}} dy_1 dy_2,$$

where  $r^2 = (y_1 - x_1)^2 + (y_2 - x_2)^2$ . It follows that

$$\begin{aligned}
u(x_1, t) &= \hat{u}(x_1, 0, t) \\
&= \frac{1}{2\pi c} \int_{x_1-ct}^{x_1+ct} \int_{-\sqrt{c^2t^2-(y_1-x_1)^2}}^{\sqrt{c^2t^2-(y_1-x_1)^2}} \frac{\varphi(y_1) \cosh(\lambda y_2)}{\sqrt{c^2t^2 - (y_1 - x_1)^2 - y_2^2}} dy_2 dy_1 \\
&= \frac{1}{2\pi c} \int_{x_1-ct}^{x_1+ct} \varphi(y_1) \int_{-s}^s \frac{\cosh(\lambda y_2)}{\sqrt{s^2 - y_2^2}} dy_2 dy_1; \quad (s = \sqrt{c^2t^2 - (y_1 - x_1)^2}) \\
&= \frac{1}{2\pi c} \int_{x_1-ct}^{x_1+ct} \varphi(y_1) \int_{-\pi/2}^{\pi/2} \cosh(\lambda s \sin \theta) d\theta dy_1 \\
&= \frac{1}{2c} \int_{x_1-ct}^{x_1+ct} \varphi(y_1) I_0(\lambda s) dy_1,
\end{aligned}$$

as claimed. The proof is complete.

For the moment, consider problem (5.13) in the more general form:

$$\begin{cases} u_{tt} - c^2 u_{xx} - r^2 u = h(x, t), & x \in \Omega_{2L}, t \in (0, +\infty), \\ u(x, 0) = 0, u_t(x, 0) = \varphi(x), & x \in \Omega_{2L}, \\ u(0, t) = u(2L, t) = 0 & t \in (0, +\infty). \end{cases} \quad (5.18)$$

We will use symmetry to extend the data in (C.12) to all of  $\mathbb{R}$ . To this end, given a function  $f : (0, 2L) \rightarrow \mathbb{R}$ , let  $\tilde{f} : (-2L, 2L) \setminus \{0\} \rightarrow \mathbb{R}$  be the odd extension of  $f$ . Then define the *symmetric extension*  $f^e : \mathbb{R} \setminus 2L\mathbb{Z} \rightarrow \mathbb{R}$  as the periodic extension of  $\tilde{f}$ .

**Proposition 11** *Assume that  $\varphi \in C[0, 2L]$ ,  $h$  and  $h_t \in C([0, 2L] \times [0, T])$ . Then (C.12) has a unique weak solution  $u$  in  $C([0, T]; H_0^1[0, 2L])$ , and  $u_t$  in  $C([0, T]; L^2(0, 2L))$ , which is given pointwise by*

$$\begin{aligned}
u(x, t) &= \frac{1}{2c} \int_{x-ct}^{x+ct} I_0(r\sqrt{t^2 - (x-y)^2/c^2}) \varphi^e(y) dy \\
&\quad + \frac{1}{2c} \int_0^t \int_{x-c\tau}^{x+c\tau} I_0(r\sqrt{\tau^2 - (x-y)^2/c^2}) h^e(y, t-\tau) dy d\tau.
\end{aligned} \quad (5.19)$$

The solution above is continuous and continuously differentiable except on the characteristics  $ct = \pm(x - 2kL)$ ,  $k \in \mathbb{Z}$ , where the partial derivatives  $u_x$  and  $u_t$  could have jump discontinuities.

**Proof:** Under the assumptions on  $\varphi$  and  $h$ , it is well known that (C.12) has a unique weak solution as described in Proposition 19. Let  $u_1$  denote solution to the problem (C.12) with

$h = 0$ . It is easily verified that the reflection principle applies to formula (5.15) and problem (5.14) exactly the same way that D'Alembert's formula applies to the undamped ( $r = 0$ ) wave equation (C.12). Hence by the reflection principle  $u_1$  coincides with the solution  $u_1^e$  of the problem (5.14) with initial velocity  $\varphi^e$  (and  $h \equiv 0$ ). Thus

$$u_1(x, t) = \frac{1}{2c} \int_{x-ct}^{x+ct} I_0(r\sqrt{t^2 - (x-y)^2/c^2}) \varphi^e(y) dy. \quad (5.20)$$

On the other hand, by Duhamel's principle the solution  $u_2$  of (C.12) with  $\varphi = 0$  is

$$\begin{aligned} u_2(x, t) &= \frac{1}{2c} \int_0^t \int_{x-c(t-\tau)}^{x+c(t-\tau)} I_0(r\sqrt{(t-\tau)^2 - (x-y)^2/c^2}) h^e(y, \tau) dy d\tau \\ &= \frac{1}{2c} \int_0^t \int_{x-c\tau}^{x+c\tau} I_0(r\sqrt{\tau^2 - (x-y)^2/c^2}) h^e(y, t-\tau) dy d\tau. \end{aligned} \quad (5.21)$$

The solution  $u$  is the superposition of  $u_1, u_2$ .

From the solution formula, it is clear that  $u$  is continuous for all  $x$  and  $t$  and the first derivatives  $u_x, u_t$  are piecewise continuous with possible discontinuities along the characteristics  $ct = \pm(x - 2kL)$ ,  $k \in \mathbb{Z}$ . This completes the proof.

### 5.2.1 Calculation of jumps along characteristics

Let  $u(x, t)$  be the solution of (C.12) as given by (C.13) with  $\lambda = r/c$ . A calculation gives

$$\begin{aligned} u_x(x, t) &= \frac{1}{2c} (\varphi^e(x+ct) - \varphi^e(x-ct)) \\ &\quad - \frac{1}{2c} \int_{x-ct}^{x+ct} I_1(\lambda s(t, x-y)) \frac{(x-y)\lambda}{s(t, x-y)} \varphi^e(y) dy \\ &\quad + \frac{1}{2c} \int_0^t (h^e(x+c\tau, t-\tau) - h^e(x-c\tau, t-\tau)) d\tau \\ &\quad + \frac{1}{2c} \int_0^t \int_{x-c\tau}^{x+c\tau} \lambda I_1(\lambda s(\tau, x-y)) \frac{-(x-y)}{s(\tau, x-y)} h^e(y, t-\tau) dy d\tau, \end{aligned} \quad (5.22)$$

$$\begin{aligned} w_x(x, t) &= \frac{1}{2c} (\varphi^e(x+ct) - \varphi^e(x-ct)) \\ &\quad - \frac{1}{2c} \int_{x-ct}^{x+ct} I_1(\lambda s(t, x-y)) \frac{(x-y)\lambda}{s(t, x-y)} \varphi^e(y) dy \\ &\quad + \frac{1}{2c} \int_0^t (h^e(x+c\tau, t-\tau) - h^e(x-c\tau, t-\tau)) d\tau \\ &\quad + \frac{1}{2c} \int_0^t \int_{x-c\tau}^{x+c\tau} \lambda I_1(\lambda s(\tau, x-y)) \frac{-(x-y)}{s(\tau, x-y)} h^e(y, t-\tau) dy d\tau, \end{aligned} \quad (5.23)$$

where  $s(t, r) = \sqrt{c^2 t^2 - r^2}$ , and

$$I_1(z) = I_0'(z) = \frac{1}{\pi} \int_0^\pi \cos \theta e^{z \cos \theta} d\theta$$

is the first order modified Bessel function.

Let  $\Xi^\pm$  denote the set of points  $(x, t)$  that are on the characteristics  $ct = \pm(x - x_0)$  emanating from points  $(x_0, 0)$  with  $x_0 \in 2L\mathbb{Z}$ , and let  $\Xi = \Xi^+ \cup \Xi^-$ . If  $\varphi$  is continuous on  $(0, 2L)$  but  $\varphi^e$  has jump discontinuities, then (C.14) remains valid for points  $(x, t) \notin \Xi$ . Let  $[\psi(x)] = \psi(x^+) - \psi(x^-)$  denote the jump of function  $\psi$  at  $x$ . For functions  $\beta(x, t)$  with jump discontinuities on the characteristics  $\Xi$ , define  $[\beta(x, t)]$  to be the jump of  $\beta$  at  $(x, t)$ , as a function of  $t$ , with  $x$  fixed.

Consider the case where  $(x, t) = (x_0 - ct, t) \in \Xi^- \setminus \Xi^+$ . Since the only contributions to  $[u_x(x, t)]$  are due to terms in the first line of (C.14), we have

$$[u_x(x, t)] = [u_x(x_0 - ct, t)] = \frac{1}{2c}([\varphi^e(x_0)] - [\varphi^e(x_0 - 2ct)]) = \frac{1}{2c}[\varphi^e(x_0)].$$

If instead,  $(x, t) = (x_0 + ct, t) \in \Xi^+ \setminus \Xi^-$ , noting that along these characteristics, crossing a characteristic in the  $t$  direction corresponds to the negative jump in the  $x$  direction. Hence

$$[u_x(x, t)] = [u_x(x_0 + ct, t)] = \frac{-1}{2c}([\varphi^e(2ct + x_0)] - [\varphi^e(x_0)]) = \frac{1}{2c}[\varphi^e(x_0)].$$

Similarly,

$$\begin{aligned} u_t(x, t) &= \frac{1}{2}(\varphi^e(x + ct) + \varphi^e(x - ct)) \\ &+ \frac{1}{2} \int_{x-ct}^{x+ct} \frac{rt I_1(\lambda s(t, x-y))}{s(t, x-y)} \varphi^e(y) dy \\ &+ \frac{1}{2c} \int_{x-ct}^{x+ct} I_0(\lambda s(t, x-y)) h^e(y, 0) dy \\ &+ \frac{1}{2c} \int_0^t \int_{x-c\tau}^{x+c\tau} I_0(\lambda s(\tau, x-y)) h_t^e(y, t-\tau) dy d\tau \end{aligned} \quad (5.24)$$

We again can easily calculate  $[u_t]$ , the jump in  $u_t$  along the characteristics. If  $(x, t) \in \Xi^- \setminus \Xi^+$ , then

$$[u_t(x, t)] = [u_t(x_0 - ct, t)] = \frac{1}{2}([\varphi^e(x_0 - 2ct)] + [\varphi^e(x_0)]) = \frac{1}{2}[\varphi^e(x_0)].$$

If  $(x, t) \in \Xi^+ \setminus \Xi^-$ , then

$$[u_t(x, t)] = [u_t(x_0 + ct, t)] = \frac{-1}{2}([\varphi^e(x_0)] + [\varphi^e(x_0 + 2ct)]) = -\frac{1}{2}[\varphi^e(x_0)].$$

We now summarize the results of calculations of jumps along characteristic lines in the following proposition.

**Proposition 12** *The solutions  $u(x, t)$  given in Proposition 19 satisfy the following properties:*

(i) *If  $(x, t) = (x_0 - ct, t) \in \Xi^- \setminus \Xi^+$ , then*

$$[u_x(x, t)] = \frac{1}{2c}[\varphi^e(x_0)], \quad [u_t(x, t)] = \frac{1}{2}[\varphi^e(x_0)].$$

(ii) *If  $(x, t) = (x_0 + ct, t) \in \Xi^+ \setminus \Xi^-$ , then*

$$[u_x(x, t)] = \frac{1}{2c}[\varphi^e(x_0)], \quad [u_t(x, t)] = -\frac{1}{2}[\varphi^e(x_0)].$$

(iii) *If  $(x, t) = (x_0 + ct, t) = (x_1 - ct, t) \in \Xi^+ \cap \Xi^-$ , then*

$$[u_x(x, t)] = \frac{[\varphi^e(x_0)] + [\varphi^e(x_1)]}{2c}, \quad [u_t(x, t)] = \frac{[\varphi^e(x_1)] - [\varphi^e(x_0)]}{2}.$$

### 5.2.2 Calculation of contact time

In the case of interest, namely  $\varphi(x) = -\mu$  is a constant and  $h(x, t) = -ge^{rt}$  with  $x \in \Omega_{2L}$ . Therefore  $\varphi^e(x) = -\mu(x)^e$  and  $h(x, t)^e = -g(x)^e e^{rt}$ , where  $g(x)^e$  and  $\mu(x)^e$  denote the symmetric extensions defined on  $\mathbb{R} \setminus 2L\mathbb{Z}$  of the constant functions  $g, \mu$  (originally defined on  $(0, 2L)$ ). With  $\lambda = \frac{r}{c}$ , we see from (5.13) and Proposition 19 that the solution to the original problem (C.10) is

$$\begin{aligned} v(x, t) &= e^{-rt}u(x, t) = e^{-rt}w(x, t), \quad \text{where} & (5.25) \\ w(x, t) &= \frac{1}{2c} \int_{x-ct}^{x+ct} I_0(\lambda s(t, (x-y)))(-\mu^e(y)) dy; \quad (s(t, r) := \sqrt{c^2t^2 - r^2}), \\ &+ \frac{1}{2c} \int_0^t \int_{x-c\tau}^{x+c\tau} I_0(\lambda s(\tau, x-y))(-g^e(y)e^{r(t-\tau)}) dy d\tau. \end{aligned}$$

Since  $v_x(0, t) = e^{-rt}w_x(0, t)$ , the boundary condition (C.3) holds if and only if  $w_x(0, t) \leq 0$ . Therefore, we compute  $w_x(0, t) = u_x(0, t)$  where  $u(x, t)$  is given by (C.13) with  $\varphi^e = -\mu^e$  and



$h^e = -g^e e^{rt}$ . We obtain

$$\begin{aligned}
w_x(0, t) &= \frac{1}{2c}(\varphi^e(ct) - \varphi^e(-ct)) \\
&\quad - \frac{1}{2c} \int_{-ct}^{ct} I_1(\lambda s(t, y)) \frac{(-y)\lambda}{s(t, y)} \varphi^e(y) dy \\
&\quad + \frac{1}{2c} \int_0^t h^e(c\tau, t - \tau) - h^e(-c\tau, t - \tau) d\tau \\
&\quad + \frac{1}{2c} \int_0^t \int_{-c\tau}^{c\tau} \lambda I_1(\lambda s(\tau, y)) \frac{y}{s(\tau, y)} h^e(y, t - \tau) dy d\tau. \tag{5.26}
\end{aligned}$$

Assume for some  $k = k(t) \in \mathbb{N}_0 = \{0, 1, 2, \dots\}$  that

$$2Lk < ct < 2L(k+1),$$

or equivalently

$$t_1 k < t < t_1(k+1). \tag{5.27}$$

Using that (i)  $s(t, r)$  is even with respect to  $r$ , (ii)  $\phi^e = -\mu^e$  is an odd function that is constant on  $(2jL, 2(j+1)L), \forall j \in \mathbb{Z}$ , (iii)  $s(t, \pm ct) = 0$ , (iv)  $\lambda = r/c$ , we compute the first two terms in (C.17),

$$\begin{aligned}
&\frac{1}{2c}(\varphi^e(ct) - \varphi^e(-ct)) - \frac{1}{2c} \int_{-ct}^{ct} I_1(\lambda s(t, y)) \frac{(-y)\lambda}{s(t, y)} \varphi^e(y) dy \\
&= \frac{1}{2c}(2\varphi^e(ct)) - \frac{1}{2c} \int_{-ct}^{ct} \left( \frac{d}{dy} I_0(\lambda s(t, y)) \right) \varphi^e(y) dy \\
&= \frac{\varphi^e(ct)}{c} - \frac{1}{2c} \sum_{j=-k}^{k-1} \int_{2Lj}^{2L(j+1)} \left( \frac{d}{dy} I_0(\lambda s(t, y)) \right) \phi^e(y) dy \\
&\quad - \frac{1}{2c} \left( \int_{-ct}^{-2Lk} + \int_{2Lk}^{ct} \right) \left( \frac{d}{dy} I_0(\lambda s(t, y)) \right) \phi^e(y) dy \\
&= \frac{\varphi^e(ct)}{c} - \frac{1}{2c} \left\{ \sum_{j=-k}^{k-1} \left( I_0(\lambda s(t, y)) \phi^e(y) \Big|_{2Lj}^{2L(j+1)} \right) + I_0(\lambda s(t, y)) \phi^e(y) \Big|_{-ct}^{-2Lk} \right. \\
&\quad \left. + I_0(\lambda s(t, y)) \phi^e(y) \Big|_{2Lk}^{ct} \right\} \\
&= \frac{1}{2c} 2\varphi^e(0^+) \{ I_0(\lambda s(t, 0)) - ( I_0(\lambda s(t, 2L)) + I_0(\lambda s(t, -2L)) ) \\
&\quad + ( I_0(\lambda s(t, 4L)) + I_0(\lambda s(t, -4L)) ) - \dots - (-1)^k ( I_0(\lambda s(t, 2kL)) + I_0(\lambda s(t, -2kL)) ) \} \\
&= \begin{cases} \frac{1}{2c} (2\varphi^e(0^+) I_0(rt)) & k = 0, \\ \frac{1}{2c} \left( 2\varphi^e(0^+) \left( I_0(rt) + 2 \sum_{j=1}^k (-1)^j I_0(r \sqrt{t^2 - (jt_1)^2}) \right) \right) & k \geq 1. \end{cases} \\
&= \frac{-\mu}{c} H_r(t), \tag{5.28}
\end{aligned}$$

where on each interval  $t \in (t_1 k, t_1(k+1))$ ,

$$H_r(t) := \begin{cases} I_0(rt), & t \in (0, t_1 := \frac{2L}{c}), \\ I_0(rt) + 2 \sum_{j=1}^k (-1)^j I_0(r\sqrt{t^2 - (jt_1)^2}) & t \in (kt_1, (k+1)t_1). \end{cases}$$

and  $k$  is defined in terms of  $t$  as in (C.18). Similar calculations can be used to simplify the last two terms in (C.17). Hence we obtain

$$w_x(0, t) = \Psi_r(t) := \frac{-\mu}{c} H_r(t) - \frac{g}{c} \int_0^t e^{r(t-\tau)} H_r(\tau) d\tau. \quad (5.29)$$

Returning to the original system (C.1)–(C.7), we see that inequality (C.3) is maintained if and only if  $\Psi_r(t) \leq 0$ . Therefore, we have the following result that defines time  $t_b$  of the first bounce in equation (C.9).

**Theorem 13** *Let set  $S = \{t : \Psi_r(t) > 0\}$ , where  $\Psi_r(t)$  is defined by (C.20).*

- (i) *If  $S = \emptyset$ , there is no bounce.*
- (ii) *If  $S \neq \emptyset$ , then the first bounce is given by  $t_b = \inf S \geq t_1 = 2L/c$ .*
- (iii)  *$t_b = t_1$  if and only if  $\Psi_r(t_1^-) + 2\mu/c > 0$ , i.e.*

$$-\mu I_0(rt_1) + 2\mu - g \int_0^{t_1} e^{r(t_1-\tau)} I_0(r\tau) d\tau > 0, \quad (5.30)$$

**Proof** Part (i) is clear. Hence assume  $S$  is not empty, and  $t_b \in \mathbb{R}$ . Note that  $\Psi_r(0) < 0$  and is strictly decreasing for  $t \in (0, t_1)$ . Therefore  $t_b \geq t_1$ , which proves part (ii). For part (iii), in order for a bounce to occur at time  $t_1$ , the stress function  $\Psi_r(t)$  has to change sign at time  $t_1$ . By Proposition 20,  $[u_x(0, t_1)] = 2\mu/c$ . Hence, the condition for a bounce is  $\Psi_r(t_1^-) + 2\mu/c > 0$ , which simplifies to (5.30).  $\square$

We examine the condition (5.30) in more details below:

**General case  $r \neq 0$  and  $g \neq 0$ :** The condition (5.30) simplifies to

$$\mu(2 - I_0(rt_1)) > g \int_0^{t_1} e^{r(t_1-\tau)} I_0(r\tau) d\tau. \quad (5.31)$$

Since the right hand side is positive, a necessary condition for solving (5.31) is

$$2 - I_0(rt_1) > 0.$$

Since the graph of  $I_0(z)$  is monotonically increasing for  $z \geq 0$ , the above condition is equivalent to the following condition

$$rt_1 < I_0^{-1}(2) \simeq 1.8. \quad (5.32)$$

Then (5.31) can be simplified as

$$\mu/g > \frac{\int_0^{t_1} e^{r(t_1-\tau)} I_0(r\tau) d\tau}{2 - I_0(rt_1)}. \quad (5.33)$$

Therefore, in order for a bounce to occur at time  $t_1$ ,  $r$  must be sufficiently small so that (5.32) holds. If also  $\mu/g$  is large enough such that (5.33) holds, then there will be a bounce at time  $t_1$ .

We examine in further details for two special cases.

**The case  $r = 0$  and  $g > 0$ :** To apply Theorem 13, in case of  $r = 0$ , we know that the stress function  $\Psi_r(t)$  becomes

$$\Psi_0(t) = -\frac{\mu}{c} H_0(t) - \frac{g}{c} \int_0^t H_0(\tau) d\tau,$$

where

$$H_0(t) := \begin{cases} 1, & t \in (0, t_1), \\ 1 + 2 \sum_{j=1}^k (-1)^j & t \in (kt_1, (k+1)t_1). \end{cases}$$

Set  $S$  in Theorem 13 is defined by  $t$  for which  $\Psi_0(t) > 0$ .

The function  $\Psi_0(t)$  is piecewise linear and  $2t_1$ -periodic. One easily deduces the following, which is more precise than Theorem 13.

**Corollary 14** *Assume  $r = 0$  and  $g > 0$  and  $\mu > 0$ . There is a first bounce at time  $t_b \geq t_1$  for which*

- (i) if  $\mu \geq gt_1$ , the first bounce time is  $t_b = t_1$
- (ii)  $0 < \mu < gt_1$ , the first bounce time is  $t_b = 2t_1 - \frac{\mu}{g}$ .

**Remark 15** *If  $r = 0$ ,  $g = 0$ , then  $t_1 = t_b$  for all  $\mu > 0$ , since hypothesis in (ii) is vacuous and only (i) applies.*

We mention that Corollary 21 was also obtained in Shi (1998a), although his formulation is different than ours.

**The case  $g = 0, r \geq 0$ :** The condition (5.30) for a bounce at time  $t_b = t_1 = 2L/c$  reduces to

$$I_0(rt_1) < 2;$$

or equivalently,

$$rt_1 < I_0^{-1}(2) \simeq 1.8. \quad (5.34)$$

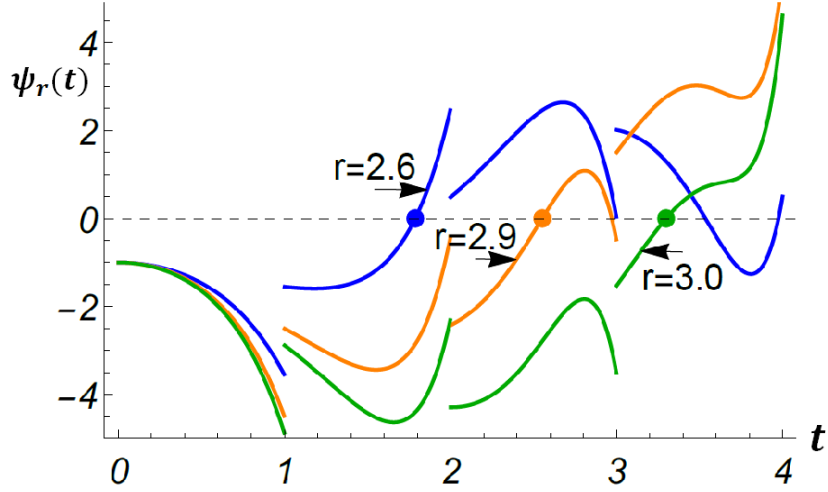


Figure 5.1: Plot for  $\Psi_r(t)$  with different  $r$  values of 2.6, 2.9 and 3.0, when  $g = 0, t_1 = 1, \mu = 1$ , and  $c = 1$ , the time  $t_b$  of first bounce for each case is indicated by a dot.

Hence for  $0 \leq r \leq I_0^{-1}(2)/t_1$ , we have  $t_b = t_1 = 2L/c$ . Mathematica computations indicate that for slightly larger values  $r$ , the bounce can occur at later times. Figure 5.1 shows a plot of the function  $\Psi_r(t)$  on the interval  $(0, 4t_1)$  in the case when  $g = 0, t_1 = 1, \mu = 1, c = 1$ , with values of  $r$  varying as 2.6, 2.9 and 3.0. For each case, the bounce time  $t_b$  occurs when the graph of  $\Psi_r(t)$  crosses the  $t$ -axis. The graph indicates the bounce time  $t_b$  at various positions within the interval  $(t_1, 2t_1)$ ,  $(2t_1, 3t_1)$  and  $(3t_1, 4t_1)$ .

### 5.3 Momentum, Center of Mass, and Energy

In this section, we will discuss the derivations and definitions of momentum, center of mass and energy. First we derive formulas for the center of mass and momentum of the rod.

#### 5.3.1 Momentum and Center of Mass

We consider the system (C.10). The momentum of the rod for  $t \geq 0$  is given by

$$P(t) = \int_0^L v_t(x, t) dx. \quad (5.35)$$

Integration of both sides of equation (C.10) with respect to  $x$  on  $[0, t_b]$  results in

$$P'(t) + 2rP(t) = \int_0^L c^2 v_{xx}(x, t) - g dx \quad (5.36)$$

$$= -c^2 v_x(0, t) - gL \quad (5.37)$$

Therefore since  $P(0) = \int_0^L (-\mu) dx = -\mu L$  and  $v_x(0, t) = e^{-rt} \Psi_r(t)$ , where  $\Psi_r(t)$  is defined in (C.20),  $P$  satisfies

$$P'(t) + 2rP(t) = -c^2 e^{-rt} \Psi_r(t) - gL, \quad 0 \leq t \leq t_b; \quad P(0) = -\mu L. \quad (5.38)$$

We solve the ODE on  $[0, t_b]$  and get

$$P(t) = -c^2 e^{-2rt} \int_0^t e^{r\tau} \Psi_r(\tau) d\tau - \frac{gL}{2r} (1 - e^{-2rt}) - \mu L e^{-2rt}. \quad (5.39)$$

Let  $h(t)$  denote the position at time  $t$  of center of mass of the rod relative to the midpoint of the rod at time 0. Thus  $h(0) = 0$ . For any  $t \geq 0$ ,  $h(t) = \frac{1}{L} \int_0^L X(x, t) dx - L/2$ , where  $X(x, t)$  denotes the position of the point with reference position  $x$  at time  $t$  defined in (C.8).

Then  $h(t)$  is given by

$$\begin{aligned} h(t) &= \frac{1}{L} \int_0^L X(x, t) dx - L/2 = \frac{1}{L} \int_0^L v(x, t) dx \\ &= \frac{1}{L} \int_0^L \left( v(x, 0) + \int_0^t v_t(x, \tau) d\tau \right) dx \\ &= \frac{1}{L} \int_0^t \int_0^L v_t(x, \tau) dx d\tau \\ &= \frac{1}{L} \int_0^t P(\tau) d\tau. \end{aligned} \quad (5.40)$$

Define

$$v^0(x) = \lim_{t \rightarrow t_b^-} v(x, t), \quad v^1(x) = \lim_{t \rightarrow t_b^-} v_t(x, t).$$

These limits exist since by Proposition 19,  $v(x, t_b)$  is continuous and  $v_t(x, t_b)$  is piecewise continuous for  $0 < x < L$ . Let

$$h^0 = h(t_b) = \frac{1}{L} \int_0^L v^0(x) dx = \frac{1}{L} \int_0^{t_b} P(\tau) d\tau, \quad (5.41)$$

$$h^1 = h'(t_b) = \frac{1}{L} \int_0^L v^1(x) dx = \frac{1}{L} P(t_b). \quad (5.42)$$

Note that  $v^0(x)$  and  $v^1(x)$  do not need to be known in order to compute  $h^0$  and  $h^1$  since  $P(t)$  is given explicitly by equation (5.39).

Let  $t_2 = \sup \{t : v(0, t) > 0 \text{ on } (t_b, t)\}$ . We can also solve  $h(t)$  and  $P(t)$  on time interval  $(t_b, t_2)$ . The PDE on this interval is:

$$\begin{cases} v_{tt} + 2rv_t - c^2 v_{xx} = -g, & (x, t) \in \Omega_L \times (t_b, t_2), \\ v(x, t_b) = v^0(x), \quad v_t(x, t_b) = v^1(x), & x \in \Omega_L, \\ v_x(0, t) = v_x(L, t) = 0, & t \in (t_b, t_2). \end{cases} \quad (5.43)$$

Since the bottom of the rod is stress free on this interval, it follows that  $\Psi_r(t) = 0$  on  $(t_1, t_b)$ .

Thus (5.36) changes to

$$P'(t) + 2rP(t) = -gL \quad P(t_b) = Lh^1.$$

Solving this ODE, one obtains

$$P(t) = -\frac{gL}{2r} + (h^1 L + \frac{gL}{2r}) e^{-2r(t-t_b)}, \quad t_b \leq t \leq t_2. \quad (5.44)$$

From  $(t_b, t_2)$ , using (5.41) and (5.44),  $h(t)$  is given by

$$\begin{aligned} h(t) &= h^0 + \frac{1}{L} \int_{t_b}^t P(\tau) d\tau \\ &= \frac{A - g(t-t_b) - h^1 e^{-2r(t-t_b)}}{2r} + \frac{g}{(2r)^2} (1 - e^{-2r(t-t_b)}), \end{aligned} \quad (5.45)$$

where  $A = h^1 + 2rh^0$ . In summary,

$$h(t) = \begin{cases} \frac{1}{L} \int_0^t P(\tau) d\tau, & t \in [0, t_b], \\ \frac{A - g(t-t_b) - h^1 e^{-2r(t-t_b)}}{2r} + \frac{g}{(2r)^2} (1 - e^{-2r(t-t_b)}), & t \in [t_b, t_2], \end{cases} \quad (5.46)$$

where

$$P(t) = \begin{cases} -c^2 e^{-2rt} \int_0^t e^{r\tau} \Psi(\tau) d\tau - \frac{gL}{2r} (1 - e^{-2rt}) - \mu L e^{-2rt}, & t \in [0, t_b], \\ -\frac{gL}{2r} + (h^1 L + \frac{gL}{2r}) e^{-2r(t-t_b)}, & t \in [t_b, t_2], \end{cases} \quad (5.47)$$

and  $h^0$  and  $h^1$  are defined in (5.41) and (5.42).

**The case  $r = 0$ :** In the undamped case, the center of mass and momentum can be determined in a more explicit form. We consider the following cases

(i) for  $r = 0$ ,  $g \geq 0$ ,  $\mu \geq gt_1$ , i.e.  $t_b = t_1$ :

Since now  $\Psi_0(t) = -\frac{\mu}{c} - \frac{g}{c}t$ , from (5.39):

$$P(t) = \mu(ct - L) + gt(ct/2 - L), \quad t \in [0, t_1]. \quad (5.48)$$

Consequently

$$h(t) = \frac{1}{L} \int_0^t P(\tau) d\tau = \frac{1}{L} (gct^3/6 + (\mu c - gL)t^2/2 - \mu Lt), \quad t \in [0, t_1]. \quad (5.49)$$

Therefore

$$h^0 = h(t_1) = -\frac{2gL^2}{3c^2}, \quad h^1 = \frac{P(t_1)}{L} = \frac{\mu L}{L} = \mu. \quad (5.50)$$

Thus, in the pure elastic case without damping, the momentum immediately after the collision is the same in magnitude as before the collision. However, when  $g > 0$ , internal stresses remain present.

For  $t \in (t_1, t_2)$ : Take limit as  $r \rightarrow 0^+$  from equation (5.44) and (5.45), one obtains

$$P(t) = \mu L - Lgt + 2L^2 g/c, \quad h(t) = -\frac{8gL^2}{3c^2} + \mu t - \frac{gt^2}{2} - \frac{2L(\mu - gt)}{c}.$$

In summary, if  $r = 0$ ,  $g \geq 0$ ,  $\mu \geq gt_1$ , then

$$P(t) = \begin{cases} \mu(ct - L) + gt(ct/2 - L), & t \in [0, t_1], \\ \mu L - Lgt + 2L^2 g/c. & t \in [t_1, t_2]. \end{cases} \quad (5.51)$$

and

$$h(t) = \begin{cases} \frac{1}{L} (gct^3/6 + (\mu c - gL)t^2/2 - \mu Lt), & t \in [0, t_1], \\ -\frac{8gL^2}{3c^2} + \mu t - \frac{gt^2}{2} - \frac{2L(\mu - gt)}{c}, & t \in [t_1, t_2]. \end{cases} \quad (5.52)$$

(ii) for  $r = 0$ ,  $g > 0$ ,  $0 < \mu/g < t_1$ , i.e.  $t_b > t_1$ :

Solving for  $P(t)$  on the intervals  $[0, t_1]$ ,  $(t_1, t_b]$  and  $(t_b, t_2)$  separately using  $\Psi_0(t) = -\frac{\mu}{c} - \frac{gt}{c}$ ,  $\Psi_0(t) = \frac{\mu}{c} - \frac{g}{c}(2t_1 - t)$ ,  $\Psi_0(t) \equiv 0$  on each respective interval. One obtains:

$$P(t) = \begin{cases} \mu(ct - L) + gt(ct/2 - L), & t \in [0, t_1], \\ -\frac{4gL^2}{c} + (\mu + gt)(3L - \frac{ct}{2}) - \frac{\mu ct}{2}, & t \in [t_1, t_b], \\ \frac{4gL^2}{c} + \frac{\mu^2 c}{2g} - L(\mu + gt), & t \in [t_b, t_2], \end{cases} \quad (5.53)$$

and

$$h(t) = \begin{cases} -\mu t - \frac{gt^2}{2} + \frac{\mu ct^2}{2L} + \frac{gct^3}{6L}, & t \in [0, t_1], \\ \frac{(4L-ct)(3\mu c(-2L+ct)+g(4L^2-5cLt+c^2t^2))}{6c^2L}, & t \in [t_1, t_b], \\ \frac{\mu^3 c^3 + (ct-4L)(3c^2 g\mu^2 - 6cg^2 L\mu) - 3g^3 L(ct-4L)^2}{6c^2 g^2 L}, & t \in [t_b, t_2]. \end{cases} \quad (5.54)$$

**Remark 16** One can use (5.51)-(5.54) to compute the maximum height  $h_{max} = h(t^*)$  by setting  $P(t^*) = 0$ . One obtains

$$t^* = \begin{cases} t_b + \frac{1}{2r} \ln(1 + \frac{2rh^1}{g}), & r \neq 0, \quad t^* < t_2, \\ \frac{2gL + \mu c}{cg}, & r = 0, \quad \mu \geq gt_1, \\ \frac{8g^2 L^2 - 2cgL\mu + c^2 \mu^2}{2cg^2 L}, & r = 0, \quad 0 < \mu < gt_1, \end{cases}$$

Therefore, if  $g > 0$ , and  $t^* \in [t_b, t_2]$ , one finds

$$h_{max} = h(t^*) = \begin{cases} \frac{h^1 + 2rh^0}{2r} - \frac{g}{4r^2} \ln(1 + \frac{2rh^1}{g}), & r \neq 0, \quad t^* < t_2, \\ \frac{\mu^2}{2g} - \frac{2gL^2}{3c^2}, & r = 0, \quad \mu \geq gt_1, \\ \frac{\mu^2(12g^2 L^2 - 8cgL\mu + 3c^2 \mu^2)}{24g^3 L^2}, & r = 0, \quad 0 < \mu < gt_1. \end{cases}$$

### 5.3.2 Energy decomposition

The energy of the rod consists of the sum of the kinetic energy, the strain energy and the gravitational potential energy and is given by

$$\mathcal{E}(t) = \frac{1}{2} \int_0^L ((v_t)^2 + c^2 v_x^2) dx + Lgh(t), \quad (5.55)$$



for any  $t \in (0, t_2)$ . At points where  $\mathcal{E}$  is differentiable one finds

$$\begin{aligned}
\frac{d}{dt}\mathcal{E}(t) &= \int_0^L (v_t v_{tt} + c^2 v_x v_{xt}) dx + Lgh'(t) \\
&= c^2 v_x v_t|_0^L + \int_0^L v_t (v_{tt} - c^2 v_{xx}) dx + P(t)g \\
&= \int_0^L v_t (-2rv_t - g) dx + P(t)g \\
&= -2r \int_0^L v_t^2 dx.
\end{aligned} \tag{5.56}$$

The boundary value problem satisfied on  $(t_b, t_2)$  is (5.43). Due to the stress free boundary conditions in (5.43), for  $t \in (t_b, t_2)$ , the eigenfunctions corresponding to (5.43) are  $\{\cos k\pi x/L\}_{k=0}^\infty$ . In particular the constant component is orthogonal to all other eigenfunctions. Hence if we decompose the initial data:

$$v^0(x) = \frac{1}{L} \int_0^L v^0(s) ds + z^0(x) = h^0 + z^0(x); \quad \int_0^L z^0(s) ds = 0 \tag{5.57}$$

$$v^1(x) = \frac{1}{L} \int_0^L v^1(s) ds + z^1(x) = h^1 + z^1(x); \quad \int_0^L z^1(s) ds = 0, \tag{5.58}$$

where  $h^0$  and  $h^1$  are given in (5.41) and (5.42), then the solution  $v(x, t)$  of (5.43) on  $[t_b, t_2]$  has the orthogonal decomposition

$$v(x, t) = z(x, t) + h(t), \quad t \in [t_b, t_2] \tag{5.59}$$

where the constant component  $h$  satisfies

$$\begin{cases} h'' + 2rh' = -g, & t \in (t_b, t_2), \\ h(t_b) = h^0, & h'(t_b) = h^1, \end{cases} \tag{5.60}$$

and  $z$  satisfies

$$\begin{cases} z_{tt} + 2rz_t - c^2 z_{xx} = 0, & (x, t) \in \Omega_L \times (t_b, t_2), \\ z(x, t_b) = z^0, \quad z_t(x, t_b) = z^1, & x \in \Omega_L, \\ z_x(0, t) = z_x(L, t) = 0, & t \in (t_b, t_2). \end{cases} \tag{5.61}$$

The solution of (5.60) was discussed in the previous subsection.

Due to the orthogonality of the solutions  $z$  and  $h$  on  $L^2(0, L)$ , the total energy  $\mathcal{E}$  has the decomposition

$$\mathcal{E}(t) = \mathcal{E}_h(t) + \mathcal{E}_z(t), \tag{5.62}$$

where for  $t \in [t_b, t_2]$ ,

$$\mathcal{E}_z(t) = \frac{1}{2} \int_0^L z_t^2 + c^2 z_x^2 dx \quad (5.63)$$

$$\mathcal{E}_h(t) = \frac{1}{2} \int_0^L (h'(t))^2 dx + Lgh(t) = \frac{1}{2L} P^2(t) + Lgh(t). \quad (5.64)$$

$\mathcal{E}_z(t)$  is the *vibrational energy*, and  $\mathcal{E}_h(t)$  is the energy corresponding to the motion of the center of mass, which we refer to as the *translational energy*.

The goal of this subsection is to determine or approximate this decomposition at the time of bounce  $t_b$ . From equation (5.56), (5.59), (5.63), and (5.64), these energies have respective decay rates given by (for  $t \in [t_b, t_2]$ )

$$\frac{d}{dt} \mathcal{E}_h(t) = -2r \int_0^L (h')^2 dx = -\frac{2r}{L} P(t)^2, \quad (5.65)$$

$$\frac{d}{dt} \mathcal{E}_z(t) = -2r \int_0^L (z_t)^2 dx. \quad (5.66)$$

Note in particular that when  $r = 0$ ,  $\mathcal{E}_h$  and  $\mathcal{E}_z$  are conserved on  $[t_b, t_2]$ .

### 5.3.2.1 The undamped case $r = 0$

When  $r = 0$ , one can use the conservation of energy law on  $[0, t_2]$  to obtain

$$\mathcal{E}(t) = \mathcal{E}(0) = \frac{1}{2} \int_0^L (v_t(x, 0)^2 + c^2 v_x(x, 0)^2) dx + Lgh(0) = \frac{\mu^2 L}{2} := \mathcal{E}_{tot}. \quad (5.67)$$

Furthermore,  $\mathcal{E}_h(t)$  can be computed with (5.51)-(5.54) and (5.64). Explicitly, one obtains for the case  $\mu \geq \mu_0$  (thus  $t_1 = t_b$ ), for  $t \in [t_1, t_2]$

$$\begin{aligned} \mathcal{E}_h(t) &= \frac{1}{2L} L^2 (-g(t - 2L/c) + \mu)^2 + Lgh(t) \\ &= \frac{L}{2} \left( -g(t - \frac{2L}{c}) + \mu \right)^2 + Lg \left( -\frac{8gL^2}{3c^2} + \mu t - \frac{gt^2}{2} - \frac{2L(\mu - gt)}{c} \right) \\ &= -\frac{2g^2 L^3}{3c^2} + \frac{L\mu^2}{2} \\ &= \frac{L}{2} \left( \mu^2 - \frac{\mu_0^2}{3} \right) \quad \left( \mu_0 = \frac{2gL}{c} \right). \end{aligned} \quad (5.68)$$

Similarly, one can compute for  $t \in [0, t_1]$ ,

$$\begin{aligned} \mathcal{E}_h(t) &= \frac{(\mu(ct - L) + gt(ct/2 - L))^2}{2L} + Lg \frac{gct^3/6 + (\mu c - gL)t^2/2 - \mu Lt}{L} \\ &= \frac{12L^2 \mu^2 + 3c^2 t^2 (2\mu + gt)^2 - 8cLt(3\mu^2 + 3g\mu t + g^2 t^2)}{24L}. \end{aligned}$$

By similar computation, for the case  $0 < \mu < \mu_0$  (thus  $t_b > t_1$ ), using (5.53), (5.54) and (5.67), one obtains

$$\mathcal{E}_h(t) = \begin{cases} \frac{12L^2\mu^2 + 3c^2t^2(2\mu + gt)^2 - 8cLt(3\mu^2 + 3g\mu t + g^2t^2)}{24L}, & t \in [0, t_1], \\ \frac{g^2(4L - 3ct)(4L - ct)^3 + 12c^2\mu^2(ct - 3L)^2 + 12c g\mu(ct - 4L)^2(ct - 2L)}{24c^2L}, & t \in [t_1, t_b], \\ \frac{1}{24}\mu^2\left(12L - \frac{8c\mu}{g} + \frac{3c^2\mu^2}{g^2L}\right) = \frac{L\mu^2(3\mu^2 - 4\mu\mu_0 + 3\mu_0^2)}{6\mu_0^2}, & t \in [t_b, t_2]. \end{cases} \quad (5.69)$$

Using the energy decomposition (5.62), conservation of energy (5.67), together with previous expressions for  $\mathcal{E}_h$ , we have the following result.

**Theorem 17** *Let  $r = 0$  and bounce time  $t_b$  as defined in Corollary 21. At time  $t_b$ , the internal energy satisfies*

$$\mathcal{E}_z(t_b) = \begin{cases} -\frac{L\mu^3(3\mu - 4\mu_0)}{6\mu_0^2}, & 0 < \mu < \mu_0 = 2gL/c, \\ \frac{\mu_0^2L}{6}, & \mu \geq \mu_0. \end{cases} \quad (5.70)$$

Thus,

$$\mathcal{E}_z(t_b)/\mathcal{E}_{tot} = \begin{cases} -\frac{\mu(3\mu - 4\mu_0)}{3\mu_0^2}, & 0 < \mu < \mu_0 = 2gL/c, \\ \frac{\mu_0^2}{3\mu^2}, & \mu \geq \mu_0. \end{cases} \quad (5.71)$$

A typical graph of  $\mathcal{E}_z(t_b)$  as a function of  $\mu$  is given in Figure 5.2. Corresponding graphs of  $\mathcal{E}_z(t_b)/\mathcal{E}_{tot}$  and  $\mathcal{E}_h(t_b)/\mathcal{E}_{tot}$  are given in Figure 5.3. We note the following observations:

- (i)  $\mathcal{E}_z(t_b)/\mathcal{E}_{tot}$  as a function of  $\mu$  is maximized at  $\mu = 2\mu_0/3$ .
- (ii)  $\mathcal{E}_z(t_b)/\mathcal{E}_{tot}$  is a continuously differentiable function of  $\mu$  for  $\mu > 0$ .
- (iii)  $\mathcal{E}_z(t)$  is constant with respect to  $\mu$  for  $\mu \geq \mu_0$ .
- (iv)  $\lim_{\mu \rightarrow \infty} \frac{\mathcal{E}_z(t_b)}{\mathcal{E}_{tot}} = 0$  for  $\mu \geq \mu_0$ .

#### 5.4 Coefficient of restitution

The standard definition for a coefficient of restitution (COR) for an impact of a particle against a fixed surface normal to the motion of the particle is the ratio of velocities, or equivalently ratio of momenta, immediately after impact ( $v_1$  or  $P_1$ ) to the immediately before the impact ( $v_0$  or  $P_0$ ) i.e,

$$e = -\frac{P_1}{P_0} = -\frac{v_1}{v_0}.$$

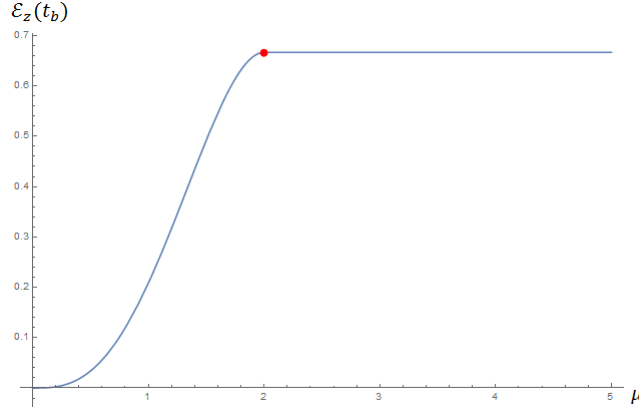


Figure 5.2: Plot for  $\mathcal{E}_z(t_b)$  when  $r = 0, c = 1.0, L = 1.0, g = 1.0$  change with  $\mu$ , the red dot corresponds to  $\mu = \mu_0$ .

Thus a purely elastic collision is described by  $e = 1$  and purely inelastic, where the motion of the particle stops at impact is described by  $e = 0$ . Intermediate values of  $e$  describe the degree of inelasticity of the impact. The idea of applying a COR to bouncing objects goes back to Isaac Newton, who suggested (see Stronge (2004a)) for example that glass should have  $e = 15/16$  and steel should have  $e = 5/9$ .

#### 5.4.1 Momentum coefficient of restitution

Analogously, we can define a momentum coefficient of restitution for the bouncing elastic rod as the ratio of momenta after and before the impact:

$$e_P = -\frac{P(t_b)}{P(0)},$$

where  $t_b$  is the bounce time. Equivalently,  $e_P = -v_{CM}(t_b)/v_{CM}(0)$ , where  $v_{CM}$  denotes the velocity of the center of mass.

**The undamped case  $r = 0$ :** From equations (5.51)-(5.54), one obtains

$$P(0) = -\mu L, \quad P(t_b) = \begin{cases} \mu L, & \mu > gt_1, \\ \frac{c\mu^2}{2g}, & 0 < \mu < gt_1. \end{cases}$$

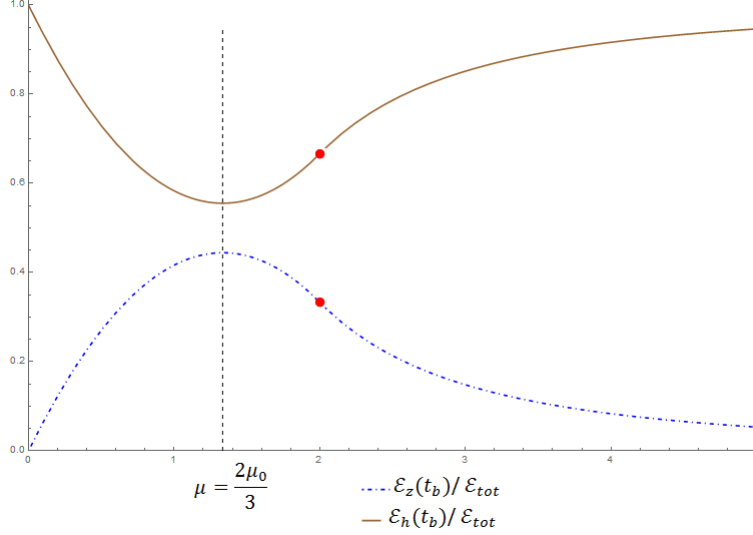


Figure 5.3: Plot for  $\mathcal{E}_h(t_b)/\mathcal{E}(0)$  and  $\mathcal{E}_z(t_b)/\mathcal{E}(0)$ , when  $r = 0, c = 1.0, L = 1.0, g = 1.0$  change with  $\mu$ , the red dot corresponds to  $\mu = \mu_0$ .

Thus, we have

$$e_P = \begin{cases} 1, & \mu > gt_1, \\ \frac{\mu c}{2gL} = \frac{\mu}{\mu_0}, & 0 < \mu < gt_1. \end{cases}$$

A flaw in this definition is that when  $g > 0$ , the position of center of mass at the end of collision is lower than the initial center of mass. Hence, even when  $e_P = 1$ , the elastic rod will not bounce as high as it was dropped from (to generate the initial momentum  $P(0)$ ). Conservation of energy is not violated since after the bounce, internal energy remains within the rod. This suggests an adjustment of the definition of COR based on translational energy  $\mathcal{E}_h$  which we propose next.

#### 5.4.2 Energetic coefficient of restitution

Since the internal energy  $\mathcal{E}_z$  of the flexible rod does not contribute to the motion of the center of mass, we define the *energetic coefficient of restitution*  $e_{\mathcal{E}}$  as the square root of the ratio of the energies  $\mathcal{E}_h$  after, and before the impact:

$$e_{\mathcal{E}} = \left( \frac{\mathcal{E}_h(t_b)}{\mathcal{E}_h(0)} \right)^{\frac{1}{2}}. \quad (5.72)$$

**The undamped case  $r = 0$ :** From (5.67) and Theorem 17

$$\mathcal{E}_h(0) = \frac{\mu^2 L}{2} = \mathcal{E}_{tot}, \quad \mathcal{E}_h(t_b) = \begin{cases} \frac{L\mu^2(3\mu^2 - 4\mu\mu_0 + 3\mu_0^2)}{6\mu_0^2}, & 0 \leq \mu < \mu_0, \\ \frac{L}{2}(\mu^2 - \frac{\mu_0^2}{3}), & \mu \geq \mu_0. \end{cases}$$

Thus,

$$e_{\mathcal{E}}^2 = \frac{\mathcal{E}_h(t_b)}{\mathcal{E}_h(0)} = \begin{cases} \frac{3\mu^2 - 4\mu\mu_0 + 3\mu_0^2}{3\mu_0^2}, & 0 \leq \mu < \mu_0, \\ 1 - \frac{\mu_0^2}{3\mu^2}, & \mu \geq \mu_0. \end{cases} \quad (5.73)$$

In fact, a typical graph of  $e_{\mathcal{E}}^2 = \frac{\mathcal{E}_h(t_b)}{\mathcal{E}_{tot}}$  as a function of  $\mu$  is given in Fig. 3 (the upper curve).

In the general undamped case ( $r = 0$ ) we can make the following observations:

- (i)  $\lim_{\mu \rightarrow 0} e_{\mathcal{E}} = 1$ ;  $\lim_{\mu \rightarrow \infty} e_{\mathcal{E}} = 1$ .
- (ii)  $e_{\mathcal{E}}$  as a function of  $\mu$  is minimized  $\mu = 2\mu_0/3$ .
- (iii)  $e_{\mathcal{E}}$  is a continuously differentiable function of  $\mu$  for  $\mu > 0$ .

Thus the relative amount of internal energy in the bouncing elastic rod is maximized at the intermediate value  $\mu = 2\mu_0/3$  and as  $\mu$  increases to infinity, the impact approaches perfectly elastic.

A limitation in application of this definition of COR is that when one attempts to apply this definition to repeated bounces, subsequent initial conditions of the impact would include some internal vibrations, and hence would not be of the same form (uniform velocity) as considered here. On the other hand, for some applications it could be appropriate to assume that any internal vibrations remaining after an impact are converted to heat, or otherwise dissipated before the next impact.

**The damped case  $r \neq 0$ :** Determination of the COR (using either the momentum or energy definition) is much more complex in the damped case since all formulas involve computing the complicated stress function  $\Psi_r(t)$  from (C.20). Therefore we focus on the energy COR  $e_{\mathcal{E}}$ .

The energy COR  $e_{\mathcal{E}}$  can be computed numerically by the following steps:

1. Compute the stress function  $\Psi_r(t)$  using (C.20);
2. Determine the bounce time  $t_b$  from Theorem 13. This involves finding the first root of the stress function  $\Psi_r(t)$ , as in Figure 5.1.

3. Calculate  $P(t_b)$  and  $h(t_b)$  from (5.39) and (5.40).
4. Calculate  $e_{\mathcal{E}}$  using (5.72),  $\mathcal{E}_h(0) = \mu^2 L/2$ , and (5.64).

For the parameters we considered, we were able to compute  $e_{\mathcal{E}}$  and related graphs using Mathematica (with about 100 time steps) in about 2 minutes computational time.

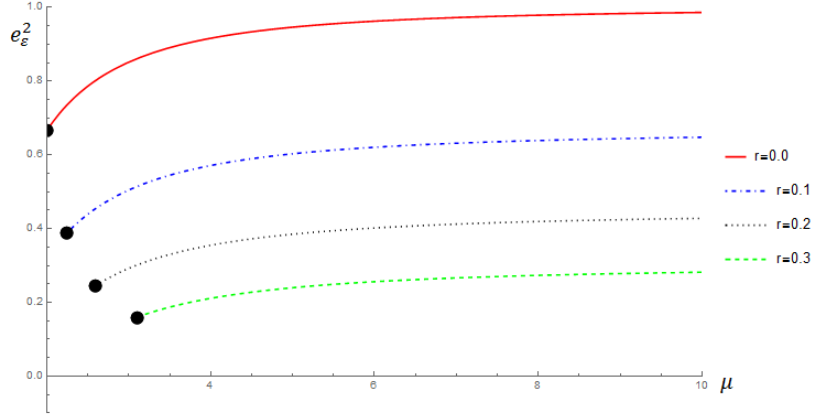


Figure 5.4: Plot for  $e_{\mathcal{E}}^2 = \frac{\mathcal{E}_h(t_1)}{\mathcal{E}_h(0)}$  with  $c = 1$ ,  $L = 1$ ,  $g = 1$ ,  $r = 0, 0.1, 0.2, 0.3$  as a function of  $\mu$ .

For the parameters considered in Figure 5.4, the two conditions (5.32) and (5.33) are satisfied for values of  $\mu$  to the right of the black dot in each of the cases  $r = 0, 0.1, 0.2, 0.3$ . (These values of  $\mu$  correspond to those for which  $t_b = t_1$ . In each case the curves continue to the left of the black dots, but are significantly more difficult to compute since  $t_b$  depends on  $\mu$  and  $r$  in a more complicated way.) Thus in each case  $t_b = t_1 = 2$ . The red curve is the undamped case  $r = 0$  and coincides with the right-most portion of the graph of the corresponding function in Figure 5.3.

We mention that when  $r > 0$ , it is possible that  $\mathcal{E}_h(t_b)$  can become negative. This happens when at the time of the bounce,  $h(t_b) < 0$  and the kinetic energy  $P(t_b)^2/2L$  is smaller in magnitude than the drop in potential energy  $|Lgh(t_b)|$ ; see eq. (5.64). This implies that the center of mass can never return to the initial value of  $L/2$  (corresponding to  $h = 0$ ) and thus in terms of the center of mass, there is not really a “bounce”. Therefore we leave  $e_{\mathcal{E}}$  undefined in these cases.

In the case  $r = 0$  we noted earlier that  $\lim_{\mu \rightarrow \infty} e_{\mathcal{E}} = 1$ . For  $r > 0$  however the graph suggests a different limit as  $\mu$  tends to infinity. In order to numerically investigate this limiting behavior more systematically, we note that

$$e_{\mathcal{E}}^2 = \frac{\mathcal{E}_h(t_b)}{\mathcal{E}(t_b)} \cdot \frac{\mathcal{E}(t_b)}{\mathcal{E}(0)}. \quad (5.74)$$

The quantity  $\frac{\mathcal{E}_h(t_b)}{\mathcal{E}(t_b)}$  is the ratio of translational energy to total energy at time  $t_b$ , and can be viewed as a form of COR that is does not depend (directly) on the viscous damping. The second is a ratio of energy at time  $t_b$  to the initial energy, hence is directly related to the decay rate of energy.

In order to analyze the terms  $\frac{\mathcal{E}_h(t_b)}{\mathcal{E}(t_b)}$  and  $\frac{\mathcal{E}(t_b)}{\mathcal{E}(0)}$  separately, it is necessary to compute  $\mathcal{E}(t_b)$ . Unfortunately there is no simple way to compute this and one must directly compute  $\mathcal{E}(t_b)$  from (5.55) by computing  $v_t(x, t_b)$  and  $v_x(x, t_b)$  for  $0 < x < L$ . This computation is described in the Appendix B.

The ratios  $\mathcal{E}_h(t_1)/\mathcal{E}(t_1)$  and  $\mathcal{E}(t_1)/\mathcal{E}(0)$  versus  $\mu$  are graphed separately in Figures 5.5 and 5.6 below. We picked the same parameter values that were used in Figure 5.4; i.e.,  $g = 1.0$ ,  $L = 1.0$ ,  $c = 1.0$ . The four curves correspond to the  $r$  values as 0.0, 0.1, 0.2 and 0.3. The values of  $\mu$  changes from 3.2 to 13.2.

The graphs are linear interpolations of data based on 25  $mu$  values, using 50 time steps for each integration (This computation took about half an hour to run).

Figure 5.5 indicates a very similar behavior with respect to  $\mu$  of the ratio  $\mathcal{E}_h(t_1)/\mathcal{E}(t_1)$  compared to the undamped case, where energy is conserved, and hence  $\mathcal{E}_h(t_1)/\mathcal{E}(t_1) = \mathcal{E}_h(t_1)/\mathcal{E}(0) = e_{\mathcal{E}}^2$ . Since  $\lim_{\mu \rightarrow \infty} e_{\mathcal{E}} = 1$ . Figure 5.5 suggests that

$$\lim_{\mu \rightarrow \infty} \frac{\mathcal{E}_h(t_1)}{\mathcal{E}(t_1)} = 1. \quad (5.75)$$

Figure 5.6 suggests that the ratios  $\mathcal{E}(t_1)/\mathcal{E}(0)$  are nearly constant functions of  $\mu$  for large values of  $\mu$ . This nearly constant value varies with respect to the damping  $r$  in a way that is related to the behavior of the decay rate of the Fourier series solution corresponding to the given initial data. This involves infinitely many modes since the initial data does not correspond to a finite combination of eigenfunctions for boundary conditions  $v(0, t) = 0$ ,  $v_x(L, t) = 0$ . However



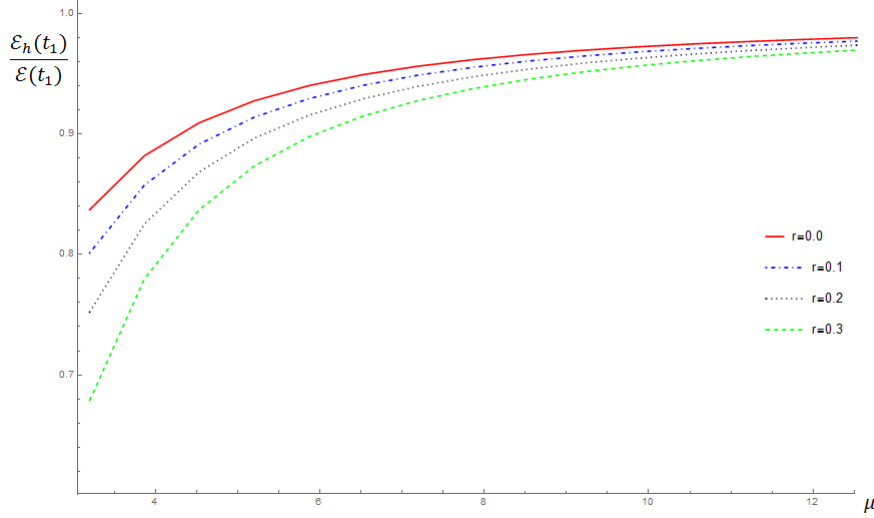


Figure 5.5: Plot for  $\mathcal{E}_h(t_1)/\mathcal{E}(t_1)$  when  $c = 1.0$ ,  $L = 1.0$ ,  $g = 1.0$  change with  $\mu$ .

the energy decay in (5.56) suggests that the ratios  $\mathcal{E}(t_1)/\mathcal{E}(0)$  might be proportionate to  $e^{-2rt_b}$ . This suggests investigating the quantity  $\frac{\mathcal{E}(t_1)/\mathcal{E}(0)}{e^{-2rt_1}}$  which is graphed in Figure 5.7.

Figure 5.7 indicates that the quantity  $\frac{\mathcal{E}(t_1)/\mathcal{E}(0)}{e^{-2rt_1}}$  tends to a common limit (approximately  $C_0 = 1$  up to numerical error) for the different values of  $r$  considered.

Thus combining this with the previous observation in (5.75) and (5.74) suggest that

$$\lim_{\mu \rightarrow \infty} e_{\mathcal{E}} \simeq e^{-rt_b}. \quad (5.76)$$

We were able to verify this numerically for the curves in Figure 5.4 to within 0.001 for each curve. This required 100 time steps in the numerical integrations.

## 5.5 Conclusion

In this chapter we have analyzed the motion of a linear elastic rod with viscous damping over the duration of an impact with the ground, which is assumed to be rigid.

First, we derived an explicit solution formula (C.13) for the motion of a bouncing elastic rod during the impact. Based on this formula we were able to find an expression for the stress function  $\Psi(t)$  at the bottom of the rod during the impact, and correspondingly obtain a characterization of the bounce time  $t_b$  in Theorem 13. In the undamped case ( $r = 0$ ), there

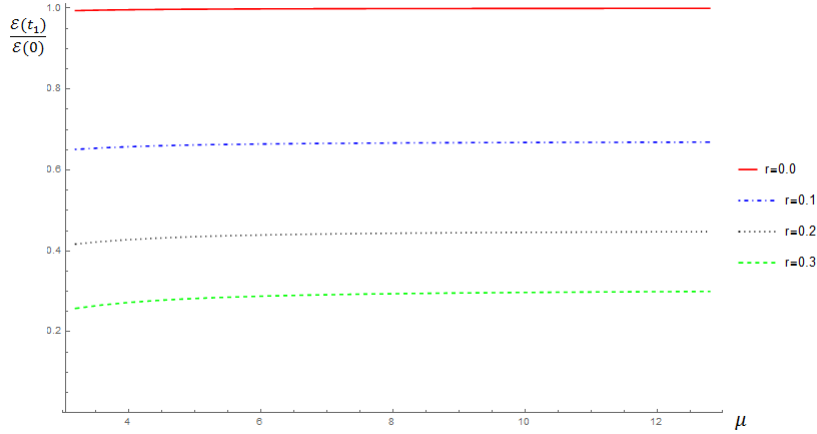


Figure 5.6: Plot for  $\mathcal{E}(t_1)/\mathcal{E}(0)$  when  $c = 1.0$ ,  $L = 1.0$ ,  $g = 1.0$  change with  $\mu$ .

is a closed form expression for  $t_b$  described in Corollary 21, where in particular,  $t_1 := 2L/c \leq t_b < 2t_1$ . In the damped case we were not able to prove that  $\Psi$  must have a root (so that there is a bounce), but were able to show that if there is a root, then  $t_b \geq t_1$ , and moreover found examples where  $t_b > 3t_1$  (see Fig. 1).

We also obtained closed form expressions (5.46), (5.47) in terms of  $\Psi(t)$  and physical constants  $c$ ,  $\mu$ ,  $g$ ,  $L$  for the relative center of mass  $h(t)$  and momentum  $P(t)$  for the time interval  $[0, t_2]$ . If  $r = 0$ , these expressions become explicit in terms parameters  $c$ ,  $\mu$ ,  $g$ ,  $L$ ; see (5.51)-(5.54).

At the time  $t_b$ , the total energy  $\mathcal{E}(t)$  has an orthogonal decomposition into translational energy  $\mathcal{E}_h(t)$  and vibrational energy  $\mathcal{E}_z(t)$ . Since  $\mathcal{E}_h$  can be expressed in terms of  $h$  and  $P$ , we obtained explicit expressions in terms of  $\Psi(t)$  for  $\mathcal{E}_h(t)$  for  $t \in [0, t_2]$ . This led to a natural energy-based definition for the COR  $e_{\mathcal{E}}$  defined in (5.72). With this definition,  $e_{\mathcal{E}} = .9$ , for example, would indicate that 81 percent of the original energy was in translational form at the end of the impact, and 19 percent was either dissipated by damping or in vibrational form. In the undamped case,  $e_{\mathcal{E}}$  is given explicitly in terms of parameters  $c$ ,  $\mu$ ,  $g$ ,  $L$  in (5.73) and is graphed as a function of  $\mu$  in Fig. 3.

In the damped case, the expression for  $e_{\mathcal{E}}$  depends on the stress function  $\Psi(t_b)$ , and hence the behavior with respect to  $\mu$  is more complex when bounce times need to be calculated.

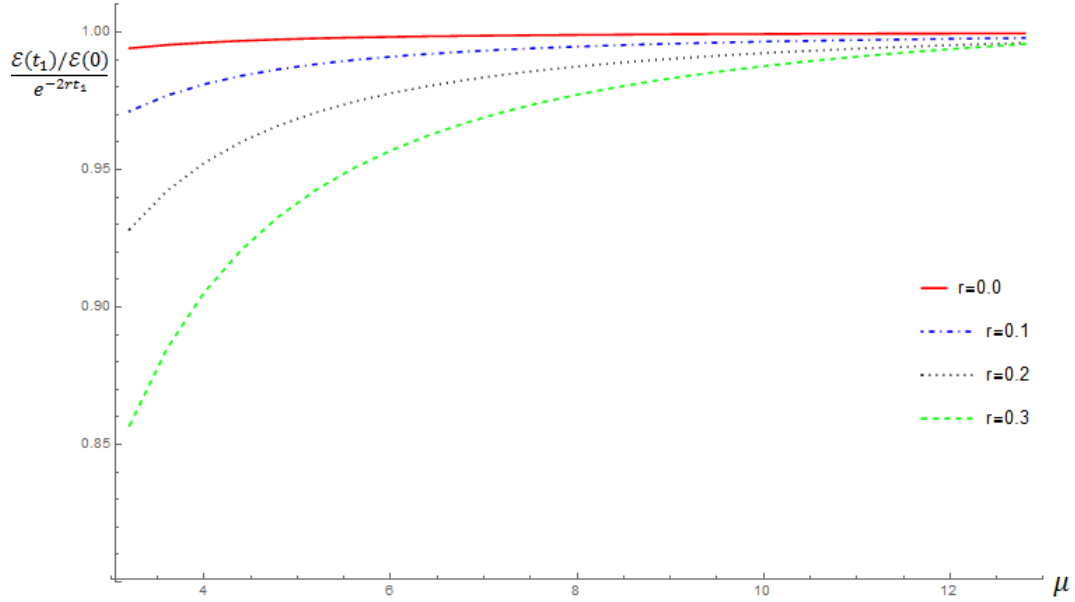


Figure 5.7: Plot for  $\frac{\mathcal{E}(t_1)/\mathcal{E}(0)}{e^{-2rt_1}}$  when  $c = 1.0$ ,  $L = 1.0$ ,  $g = 1.0$  change with  $\mu$ .

Figure 4 describes the behavior with respect to  $\mu$  when  $\mu$  is large enough so that by Theorem 13,  $t_b = t_1$ . This simplifies the numerical computations. Part of the value of  $e_{\mathcal{E}}$  is due to damping and part is due to the ratio of vibrational energy to total energy at the end of the contact period, as indicated in (5.74). Figures 5, 6, 7 characterize, up to numerical error, the behavior with respect to  $\mu$  of the decomposition (5.74) of  $e_{\mathcal{E}}$ . Based on these graphs, we suspect that the limiting behavior with respect to  $\mu$  is described by (5.76), which at least for the examples considered, seems to be correct. More discussions on structural damping can be found in Appendix C.

## CHAPTER 6. PICKING UP SOFT OBJECTS AND RECOVERING GRAVITY FREE SHAPE IN 3D

The rationale for studying how to pick up soft objects is inspired by the human behaviour. In our daily life, when we grasp an object, we always try to figure out the comfortable direction and try to save some effort by our tactile feelings. Therefore, it is an interesting topic for us to perform some theoretical analysis. Later, we can apply the result to a robot hand in grasping.

The stiffness matrix of an object is based on the shape of it, which helps describe the displacement under certain forces and study the deformation of the object. Basically, a stiffness matrix reflects the geometric and material property of an object. When we construct the stiffness matrix based on the finite element method, we already neglect the fact that the object is already under gravity force and has some deformation based on the gravitational force. However, to get the accurate model, we require the exact shape of the object in a gravity free situation. Hence, it is interesting for us in gravity-free situation to explore and know the information of the original shape of an object.

### 6.1 Introduction

In this section, some simple strategies of picking up soft objects will be introduced. Discussions are also on different events, including sliding and sticking which happened during the picking up process. The problem focused on at the end will be picking up soft 3D objects with two spherical robot fingers. It is not simply one more dimension added on to the previous problem, but there are more technical issues coming up and it is a much more difficult problem. FEM is the major tool applied here for the analysis. We will firstly discuss about strategy of picking up soft 3D objects.

Next, a series of analysis of recovering gravity free shape of 3D objects will be conducted. An iterative method was proposed to recover the displacement based on revising the stiffness matrix through the iterations.

## 6.2 Picking up soft 3D objects with two fingers

In this section, we will discuss a simple strategy of picking up a 3D soft object by two fingers. The idea is inspired by human being behaviour. In our daily life, when we try to pick up an object, we usually squeeze a little bit, and feel if we can lift the object up. If the squeeze depth is not big enough, we may need to squeeze a little bit more until it is enough to hold the weight and finally lift up the object. The paper written by Lin et al. (2014) described the details about the topic.

### 6.2.1 Theoretical background

In fact, the 2D case and 3D case have similar aspects in analysis with each other. However, there also exists a huge difference between them. To study the 3D case, it is not simply to add one more dimension. Due to the third dimension, we have to consider the effect of the gravity on the shape of the object, which was ignored in the 2D planar object case. Here is a picture [6.1](#)<sup>1</sup> simulates picking up a soft object. We will begin with a brief review of linear elasticity applied in 3D situation. In the previous section, I have presented the terminologies in 2D case. Consider ever point in the 3D case moves from  $(x, y, z)^T$  to  $(x + u, y + v, z + w)^T$ . Similarly, we have the normal strains and the shear strains denoted as follows:

$$\epsilon_x = \partial u / \partial x$$

$$\epsilon_y = \partial v / \partial y$$

$$\epsilon_z = \partial w / \partial z$$

$$\gamma_{xy} = \partial u / \partial y + \partial v / \partial x$$

$$\gamma_{yz} = \partial v / \partial z + \partial w / \partial y$$

$$\gamma_{zx} = \partial w / \partial x + \partial u / \partial z$$

---

<sup>1</sup>Courtesy of Huan Lin.

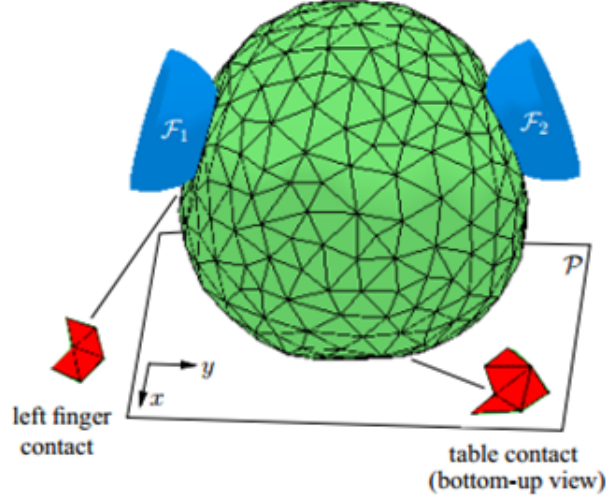


Figure 6.1: Lifting up a 3D object

The strain energy in the 3D case is

$$U_0 = \frac{E}{2(1+\nu)} \int_V \left[ \frac{\nu}{1-2\nu} (\epsilon_x + \epsilon_y + \epsilon_z)^2 + (\epsilon_x^2 + \epsilon_y^2 + \epsilon_z^2) + \frac{1}{2} (\gamma_{xy}^2 + \gamma_{yz}^2 + \gamma_{zx}^2) \right] dV. \quad (6.1)$$

Compared to the 2D case, we have a similar theorem:

**Theorem 18** *Under linear elasticity, any displacement field  $\boldsymbol{\delta} = (u(x, y, z), v(x, y, z), w(x, y, z))^T$  that yields zero strain energy is linearly spanned by the following three fields:  $(1, 0, 0)^T$ ,  $(0, 1, 0)^T$ ,  $(0, 0, 1)^T$ ,  $(0, -z, y)^T$ ,  $(z, 0, x)^T$ , and  $(-y, x, 0)^T$ .*

The potential energy in 3D case is

$$\Pi = U - W = \frac{1}{2} \boldsymbol{\Delta}^T K \boldsymbol{\Delta} - \boldsymbol{\Delta}^T (\mathbf{F} + \mathbf{G}). \quad (6.2)$$

It reaches the minimum value with the constitutive equation

$$K \boldsymbol{\Delta} = \mathbf{F} + \mathbf{G}. \quad (6.3)$$

After the preview of the math and physics background, let now move back to focus on the strategy of picking up the object. The idea is not hard to understand. First first compute the object's initial configuration of lying on the table by iterative procedure. Then during the process of squeezing the object by two fingers, we will do the lift test simultaneously. If the

object finally past the lift test, then it means we can successfully lift it up. Otherwise, if the squeeze depth is too big such that it is over the range of the linear elasticity, then the lift test failed.

Let us start by constructing the initial configuration of the soft object lying on a plane using algorithm 6. Here, we denote the indices of the nodes that are in contact with the two fingers and the plane to be  $\mathbb{I}$ ,  $\mathbb{J}$ , and  $\mathbb{K}$ . Denote  $\mathbb{P}$  to be the set that collects the indices of sliding nodes.

---

**Algorithm 6** Compute initial resting configuration.

---

- 1:  $\mathbb{P} \rightarrow \emptyset$ .
  - 2: Compute the change displacement vector  $\Delta'$  from the displacement vector  $\Delta$ . Correspondingly compute the change force  $F'$  from the contact force  $F$ .
  - 3:  $\Delta \rightarrow \Delta + \Delta'$  and  $F \rightarrow F + F'$ .
  - 4: If there is no new contact node and  $f_k$  lies in side the friction cone for every  $k \in \mathbb{K}$ , then STOP.
  - 5: Otherwise deal with the new contact.
  - 6: Find sliding nodes and add the corresponding indices into  $\mathbb{P}$ .
  - 7: Recompute the sliding nodes' displacements.
- 

Briefly, the algorithm can be summarized as first evaluate the displacement without considering sliding. If there is some new contact node, add the furthest displacement below plane and scale down displacements, and identify sliding nodes and recompute displacements, go back to the iterations. If there is no new contact points and no sliding point, that means we have successfully computed the initial configuration and we can stop.

After we finish computing the initial resting configuration, the two fingers will be translating in a constant direction step by step. During the process, we will do the lift test to see if the forces are big enough to lift the object. The lift test is about the liftable weight  $w$  during the process of lifting. Liftable weight is the weight that the finger forces can hold until one of the fingers almost starts to slide. Originally we suppose the liftable weight is zero. As the squeeze step increases, the liftable weight also goes up. Once the liftable weight reaches the object's weight, the lift test is passed. The algorithm is as follows.

There will also be four events happen during the process. The contact sets  $\mathbb{I}$ ,  $\mathbb{J}$ , and  $\mathbb{K}$  will not change until the next event happen. The definition of these four events are exactly the

---

**Algorithm 7** Pick up 3D deformable object by two fingers.

---

- 1: Input tetrahedron mesh of the object, initial table contact triangle with vertices  $\mathbf{p}_q, \mathbf{p}_r, \mathbf{p}_s$ . Finger contacts  $\mathbf{p}_i, \mathbf{p}_j$ , squeeze  $(\mathbf{d}_1, \mathbf{d}_2)$ .
  - 2: Check if  $\mathbf{p}_i, \mathbf{p}_j$  with the initial triangle forms a force closure. If not, return FAIL. Otherwise, continue to the next step.
  - 3: Use algorithm 6 to compute the initial resting configuration.
  - 4: Squeeze the object by translating the two fingers with the forces  $\mathbf{F}_1, \mathbf{F}_2$ .
  - 5: Do lift test during the squeezing process.
  - 6: If so, stop squeezing object and change to lifting the object. Record the squeeze depth.
  - 7: If enough squeeze depth has been applied but still cannot be picked up, return FAIL. Else go back to step 4.
- 

same as previous section: (A) contact establishment, (B) contact break, (C) stick to slip and (D) slip to stick.

During the process, it is important for us to track the movements of all the sliding nodes. Remember their indices are collected in the set  $\mathbb{P}$ . The sliding can happen in the contact plane or the semi spherical fingers. Thus, we will have two different equations to solve the sliding variable  $d_k$ .

First, for the sliding points happen in the contact plane, the force  $\mathbf{f}_k$ ,  $k \in \mathbb{P}$  has to lie on the edge of the friction cone. What's more, each  $\mathbf{f}_k$  is a linear function of all the variables  $d_l$ ,  $l \in \mathbb{P}$ . Suppose the friction coefficient between the object and the table is  $\mu_p$ , then we will have the system of  $|\mathbb{P}|$  quadratic equations:

$$(1 + \mu_p^2)(\mathbf{f}_k \cdot \mathbf{z})^2 = \mathbf{f}_k \cdot \mathbf{f}_k. \quad (6.4)$$

Here the  $\mathbf{z}$  is the normal of the plane, which is  $(0, 0, 1)$ . Then suppose the friction coefficient between the finger and the object is  $\mu_F$ . Assume  $\tilde{\mathbf{p}}_k$  is the position before slip, and reach some point  $\mathbf{q}_k$ . The contact force has the tangential component as

$$\mathbf{f}_{i\perp} = \mathbf{f}_k - (\mathbf{f}_k \cdot \mathbf{n}_k)\mathbf{n}_k. \quad (6.5)$$

The sliding will be along the opposite direction of  $\mathbf{f}_{k\perp}$ . Denote the sliding angle along the great circle of the finger to be  $\theta_k$ , and  $c_k = \cos \theta_k$ ,  $s_k = \sin \theta_k$ . The equations will be:

$$(1 + \mu_F^2)(\mathbf{f}_k \cdot \mathbf{n}_k)^2 = \mathbf{f}_k \cdot \mathbf{f}_k, \quad (6.6)$$

$$c_k^2 + s_k^2 = 1. \quad (6.7)$$



Figure 6.2 shows a spherical robot finger tip that we use in the model of picking up soft object. It helps us understanding the situation happens on a finger.

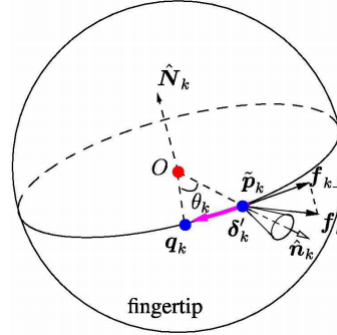


Figure 6.2: Sliding of a node on the hemispherical finger

After every  $\mathbf{f}_k$  is written as linear combinations of the variables  $d_l$ , a large system of quadratic equations is attained. To store those quadratic equations, pull out the coefficients to be a coefficient matrix. Since it is a very complicated system, we can only solve it by numerical methods. Here, the homotopy continuation method is used to solve it. This method is also used in the function "RootFinding" in a mathematics software called "Maple". Homotopy method is used to find the isolated root of the system of polynomial equations with the same number of variables in each of the equations. This method is a continuous map from a set of constructed known solutions to the solutions of the input system. The map function is constructed as

$$\mathbf{H}(\mathbf{x}, t) = \{(1-(1-t)^2)p_1(x_1, \dots, x_n) - (1-t)^2q_1(x_1), \dots, (1-(1-t)^2)p_n(x_1, \dots, x_n) - (1-t)^2q_n(x_n)\}. \quad (6.8)$$

Here,  $q_1(x_1), \dots, q_n(x_n)$  are a sequence of generated random polynomials, and they are called the generated starting system. It is not hard for us to notice that when  $t = 0$ , the solution of  $\mathbf{H}(\mathbf{x}, 0) = 0$  will be the solution of the generated starting system. When  $t = 1$ ,  $\mathbf{H}(\mathbf{x}, 1) = 0$  gives us the solution of the input system. We start from the following way.

Here, we need further explanation on step 4. Since  $\mathbf{H}(\mathbf{x}, t) = 0$ , we can do the partial differentiation with it and get:

$$\frac{\partial \mathbf{H}}{\partial \mathbf{x}} \cdot \frac{d\mathbf{x}}{dt} + \frac{d\mathbf{H}}{dt} = 0. \quad (6.9)$$

---

**Algorithm 8** Homotopy continuation method.

---

- 1: Input the system of polynomials  $p_1(x_1, x_2, \dots, x_n), \dots, p_n(x_1, x_2, \dots, x_n)$ .
  - 2: Generate a start system  $q_1(x_1), \dots, q_n(x_n)$ .
  - 3: Construct the map function as equation (6.8).
  - 4: Differentiate the system and turn it into an ODE problem. Time  $t$  changes from 0 to 1. The path will be followed by discrete steps.
  - 5: At each step, using an ODE solution method as a predictor, then use the Newton's numerical method to polish the root to ensure the computed root stay on the path.
  - 6: iterate enough steps and output the result.
- 

Then we can get:

$$\frac{d\mathbf{x}}{dt} = -\left(\frac{\partial \mathbf{H}}{\partial \mathbf{x}}\right)^{-1} \frac{d\mathbf{H}}{dt}. \quad (6.10)$$

Then change from  $\mathbf{x}(0) \rightarrow \mathbf{x}(h)$ , we can use the following to compute:

$$\mathbf{x}(h) = \mathbf{x}(0) + h \frac{d\mathbf{x}}{dt}(0). \quad (6.11)$$

The general iterations will be,

$$\mathbf{x}_{n+1} = \mathbf{x}_n + h \frac{d\mathbf{x}}{dt}(\mathbf{x}_n). \quad (6.12)$$

After each iteration, polishing of the values is needed by using Newton's method,

$$\mathbf{x}_{n+1}^* = \mathbf{x}_{n+1} - \left(\frac{\partial \mathbf{H}}{\partial \mathbf{x}}(\mathbf{x}_{n+1})\right)^{-1} \mathbf{H}(\mathbf{x}_{n+1}). \quad (6.13)$$

We choose homotopy method to solve the roots instead of Newton's reason. The reason is that homotopy method is a global convergent method. However, Newton's method only converge when you star with a very close initial guess to the real solution.

### 6.2.2 Simulations and experiments

We have done the simulations and experiments on four different objects: tomato, orange, steam bun and toy football. Their data is listed as below in Table(6.1).

The simulations and experiments figures is in Figure (6.3).

It would be an interesting topic for us to study about how the softness of an object affects the grasping and lifting up of this object. Young's modulus affects the softness of an object. If the number is bigger, it means the object's material is harder. When Young's modulus goes to infinity, that means the object is close to a rigid body.

Table 6.1: Information of the objects

	<b>tomato</b>	<b>orange</b>	<b>steam bum</b>	<b>football</b>
vertices	490	600	658	875
surface facets	498	564	646	782
tetrahedra	2129	2692	2941	4058
weight $w$	1.246	1.868	0.467	0.489
Young's modulus $E$	$1.0 \times 10^5$	$1.4 \times 10^5$	$2.0 \times 10^3$	$6.0 \times 10^3$
Poisson's ratio $\nu$	0.4	0.4	0.2	0.3
friction coefficient $\mu$	0.32	0.34	0.4	0.5

To figure out how Young's modulus affect the grasping and lifting, I have conducted several simulation examples. I took down the data of the total work the finger did during the process of squeezing until the object is liftable. The study object is in the same shape as the football. There are in total 332 grid points on the surface of the football. The Poisson's ratios is 0.3, density of the object is  $2 \times 10^2$ . Here, we fix all the other parameters, and let the Young's modulus change from  $1.0 \times 10^3$  to  $6.0 \times 10^4$ , part of the data of total work is shown in Table(6.2).

Table 6.2: Young's modulus with total work

$E$	<b>total work</b>
$1.0 \times 10^3$	0.000862824
$4.0 \times 10^3$	0.00150976
$9.0 \times 10^3$	0.00342252
$3.0 \times 10^4$	0.00475993
$6.0 \times 10^4$	0.00770573

The plot data of the relationship between Young's modulus and fingers total work is in Figure(6.4).

From the data, we can preliminary get the result that to pick up a harder objects seems to cost more work. However, this topic still needs further understanding since we don't have the theoretical result currently. The little discontinuous jump in the picture is caused by the discretization of the object, and also the squeeze depth.





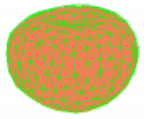
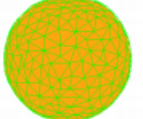
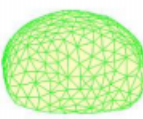
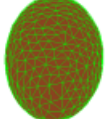




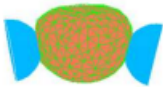
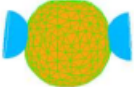
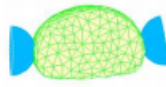
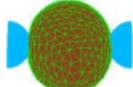
			
			
			
			
(11, 0.018, 1.86)	(15, 0.025, 2.75)	(8, 0.010, 2.41)	(10, 0.011, 3.12)

Figure 6.3: Picking up objects successfully. An entry in the last row lists the number of contact nodes, the squeeze depth, and the running time

### 6.3 Recovering the gravity-free shape of a 3D deformable object

Everywhere people's daily life is affected by gravity. For example, when you place an animal organ on a plate, it will change the shape due to the different positions and faces you put it in. The same thing will happen to a tomato. When you put it upside down, it looks very different from when you put it face up. However strictly speaking, a solid deformable object setting on a plane will change shapes due to gravity, this is not equivalent to any kind of rigid body transformation. To pick up a soft solid object, not only does the force have to balance the gravity, but also the change of geometry and contact areas have to be considered.

The gravitational force acts throughout the solid relative to its volume. To obtain the deformed shape we need to get the minimized potential energy, which equals the body's strain energy minus the external forces related work. The finite element method gives us instruction

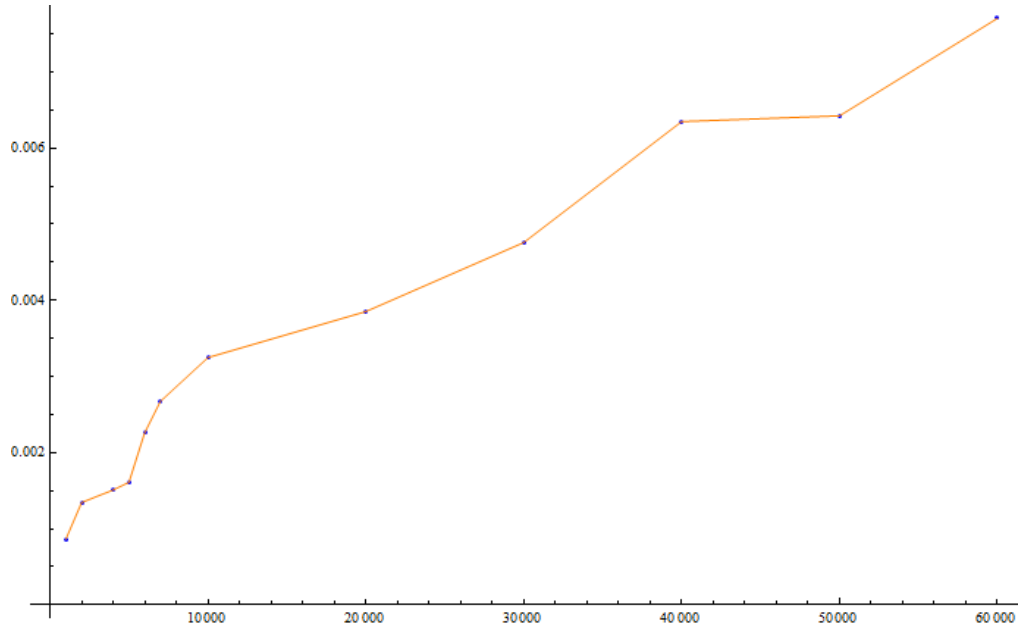


Figure 6.4: Relations between the Young's modulus and total work

to discretize the object body into meshes. Then based on the corresponding forces applied on the body mesh to construct the stiffness matrix, displacement vector and the force vector can be set up as a linear system of equations. This solves the unknown displacement variables. Here, the equation is called the constitutive equation, which is a very classical result in mechanics and physics. It has the form of the product of stiffness matrix and displacement vector on the left, and the force vector on the right side of the equation.

Usually, when we construct the stiffness based on FEM theory, the shape we use is based on the observed shape, which is under gravity. However, the gravity affects the elements inside the matrix in nonlinear sense, and it's not simply a coefficient multiplied by the matrix due to the nonlinearity. To treat the gravity force, it's in a similar way to treat the body force that is applied on an object. It's not appropriate to simply exempt the gravitational force on both sides of the constitutive equation since the property of stiffness matrix is nonlinear to the gravity term. But in many situations, people use the shape under gravity to construct the stiffness matrix; this won't give them too much error in the situations like light object or perhaps there is so much body force that gravity force's effect can be ignored. However, in other situations, the effect of this error can be crucial, such as during surgeries.

To get a more precise model when the gravity effect can't be ignored, the idea is to restore the original shape of the object, then construct the stiffness matrix based on a more accurate shape. With the gravity-free model, we can continue to calculate more body force effect applied on the object and obtain a more precise result. In the next several sections, we will review the method of FEM applying on computing the deformation of solid object sitting on a plane. Then describe the fixed point iteration method which we used to solve for the model in single tetrahedron and normal objects separately. Also, I will provide the related experiment about applying the gravity free model to calculate the deformation of an object and compare with the old method, which is using the under gravity model.

Metric system is applied everywhere in the discussion, e.g., for length we use meter, for mass we use kilogram, for force we use Newton, and for pressure we use Pascal and so on. We will not mention the units again during the discussion. When a vector is mentioned, we usually mean it is a column vector. Some other math notations, for example, a vector  $\mathbf{v} = (v_1, v_2, \dots, v_n)^T$  is a row vector, to calculate the derivative of the scalar  $u$  with respect to vector  $\mathbf{v}$  will be  $\partial u / \partial \mathbf{v} = (\frac{\partial u}{\partial v_1}, \dots, \frac{\partial u}{\partial v_n})$ . The derivative of a vector  $\mathbf{u} = (u_1, u_2, \dots, u_m)^T$  with respect to another vector  $\mathbf{v} = (v_1, v_2, \dots, v_n)^T$  will be a matrix:

$$\frac{\partial \mathbf{u}}{\partial \mathbf{v}} = \begin{pmatrix} \partial u_1 / \partial v_1 & \dots & \partial u_1 / \partial v_n \\ \dots & \dots & \dots \\ \partial u_m / \partial v_1 & \dots & \partial u_m / \partial v_n \end{pmatrix}, \quad (6.14)$$

### 6.3.1 FEM applied in computing the deformation

For a soft solid object sitting on a plane like a table, it deforms under gravity force and also the supporting force from the plane. The gravity force is usually ignored based on the traditional FEM application models. By using the 3D scanner, we can generate the triangulated 3D mesh of the object under gravity. We call those points on the mesh to be  $\mathbf{p}_1, \dots, \mathbf{p}_n$ , and the corresponding displacement vectors with respect to those points will be  $\boldsymbol{\delta}_1, \dots, \boldsymbol{\delta}_n$ . The stiffness matrix constructed over the current under gravity mesh will be called  $K'$ . The constitutive equation we have mentioned before for computing the deformation of the object is:

$$K'(\delta_1^T, \dots, \delta_n^T)^T = \mathbf{F} \quad (6.15)$$

Although the total gravitational force and supporting force will be balanced, it's easy to be seen that the  $\mathbf{F}$  in the equation is not a simple zero, since there are still internal forces to balance each other. There seems to exist a contradiction at first glance of the equation, since the object is already balanced by the forces, where should the deformations come from. This is result by the inaccurate model that FEM usually used, because it doesn't concern the deformation caused by the gravitational force. However, in the real situation, it happened that we can't ignore the result by gravity when there is not a negligible amount of effect on the shape of the object. When the mass of the object is small, usually the gravity won't cause much deformation, thus using the inaccurate model won't give us much error. However, if we still use the old model, when the mass of the object is large enough so that the gravity effect can't be ignored, there can be some non negligible error evolved.

To fix this issue, we will compute the stiffness matrix of the object under gravity free shape, then apply this stiffness matrix to calculate further deformations of the object with other body forces. Here are some notations: we denote  $\mathbf{p}_1, \dots, \mathbf{p}_n$  to be the gravity free locations of the points on the mesh, and denote  $\tilde{\mathbf{p}}_1, \dots, \tilde{\mathbf{p}}_n$  to be the locations of the points under gravity (also observed shape). Each of them is a point with  $x, y, z$  coordinates. For  $1 \leq i \leq n$ ,  $\mathbf{p}_i = (x_i, y_i, z_i)^T$  and  $\tilde{\mathbf{p}}_i = (\tilde{x}_i, \tilde{y}_i, \tilde{z}_i)^T$ . Define the nodal displacement  $\delta_i = \tilde{\mathbf{p}}_i - \mathbf{p}_i = (u_i, v_i, w_i)^T$ . We assume that the gravitational force is uniformly applied on the object. Thus, for each of the triangulated tetrahedron in the mesh, each of the vertices takes one fourth of the the corresponding tetrahedron's gravity force. During the process of deformation under gravity, we assume that all of the vertices that contact the plane will still stick to the plane due to the large enough friction. Let those sticking points' index be from  $n - s + 1, \dots, n$ , which are  $\mathbf{p}_{n-s+1}, \dots, \mathbf{p}_n$ . Then correspondingly, since they are sticking to the plane, there is no changing position for them, so  $\delta_{n-s+1} = \dots = \delta_n = \mathbf{0}$ . After which, to completely describe the problem, we will need the vector  $\mathbf{P} = (\mathbf{p}_1^T, \dots, \mathbf{p}_{n-s}^T)^T$ , the vector  $\tilde{\mathbf{P}} = (\tilde{\mathbf{p}}_1^T, \dots, \tilde{\mathbf{p}}_{n-s}^T)^T$ , and  $\Delta = (\delta_1^T, \dots, \delta_{n-s}^T)^T$ . We still have  $\mathbf{P} = \tilde{\mathbf{P}} - \Delta$ .

For the gravitational force exerted on the points  $\mathbf{p}_1, \dots, \mathbf{p}_{n-s}$ , call it  $\mathbf{G}$ , which is a  $m$

dimensional vector,  $m = 3(n - s)$ . Due to the reason that the last  $s$  positions of points on the mesh are fixed, we will only be interested in the reduced stiffness matrix  $K$ , which is eliminated the last  $3s$  rows and columns. The reduced stiffness matrix will be symmetric and positive definite. It will depends on  $\mathbf{P}$ , which is essentially depends on the solution corresponds to  $\mathbf{\Delta}$  and  $\tilde{\mathbf{P}}$ . So we can rewrite the constitutive equation as:

$$K(\mathbf{\Delta})\mathbf{\Delta} = \mathbf{G} + \mathbf{F} \quad (6.16)$$

### 6.3.2 The case of one tetrahedron

Given a single tetrahedron with four vertices  $(\tilde{x}_i, \tilde{y}_i, \tilde{z}_i)$ ,  $i = 1, 2, \dots, 4$ , lying on a table under gravity, we want to recover its shape in the situation without gravity. Suppose the coordinates of the vertices in the original shape are  $(x_i, y_i, z_i)$ ,  $i = 1, 2, \dots, 4$ . When we apply the gravity to the object, the displacement of each of the vertices will be  $(u_i, v_i, w_i) = (\tilde{x}_i, \tilde{y}_i, \tilde{z}_i) - (x_i, y_i, z_i)$ ,  $i = 1, 2, \dots, 4$ . In our model, we fix the bottom three points of the tetrahedron. Hence,  $(u_i, v_i, w_i) = (0, 0, 0)$ ,  $i = 2, 3, 4$ . In order to solve for the displacement vector of  $\mathbf{\Delta} = (u_1, v_1, w_1, 0, \dots, 0)^T$ , we will start from the constitutive equation:

$$K\mathbf{\Delta} = \mathbf{F} + \mathbf{G}, \quad (6.17)$$

where  $K$  is the  $12 \times 12$  stiffness matrix of the original shape, which is constructed based on the displacement variables  $u_i, v_i, w_i$  and data of the current shape  $\tilde{x}_i, \tilde{y}_i, \tilde{z}_i$ , and

$$\mathbf{F} = (0, 0, 0, f_{2x}, f_{2y}, f_{2z}, \dots, f_{4x}, f_{4y}, f_{4z})^T, \quad (6.18)$$

$$\mathbf{G} = (0, 0, -G/4, \dots, 0, 0, -G/4)^T. \quad (6.19)$$

Here,  $G$  is the gravity of the tetrahedron. We apply the gravity force equally on the four vertices, which means  $G/4$  along  $-z$  direction for each.

Below, Figure 1 shows us an example of a single tetrahedron. Without loss of generality, we can always pick one surface of the tetrahedron to lie on the  $x$ - $y$  plane, two of its vertices  $P_2$  and  $P_4$  along  $x$ -axis with one of them  $P_4$  at the origin, and the other with coordinates  $(\tilde{x}_2, 0, 0)$ .



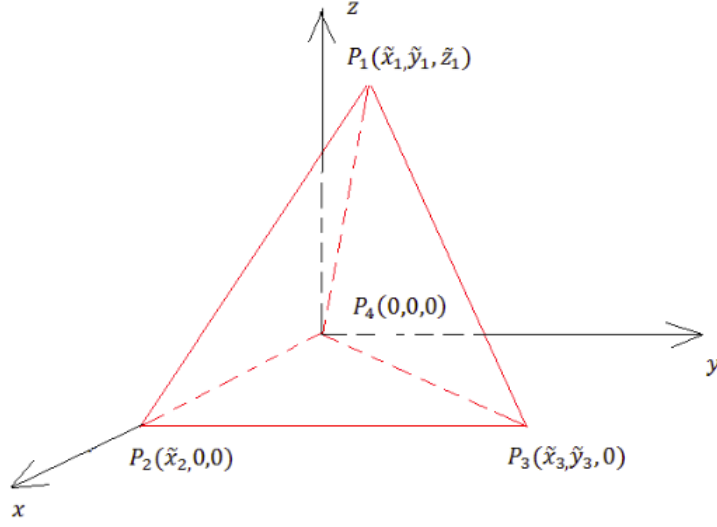


Figure 6.5: A tetrahedron

Nine constraints are imposed from fixing the vertices  $P_2$ ,  $P_3$ , and  $P_4$ . We are left with only three variables, which are  $u_1$ ,  $v_1$ , and  $w_1$ . Therefore, we can reduce the twelve nonlinear equations in equation(6.17) to just three equations, which are the first three rows of each of the component. The reduced system is shown as below:

$$\begin{pmatrix} \frac{EV}{4(1+\nu)(w_1-\tilde{z}_1)^2} & 0 & 0 \\ 0 & \frac{EV}{4(1+\nu)(w_1-\tilde{z}_1)^2} & 0 \\ 0 & 0 & \frac{EV(\nu-1)}{2(1+\nu)(2\nu-1)(w_1-\tilde{z}_1)^2} \end{pmatrix} \begin{pmatrix} u_1 \\ v_1 \\ w_1 \end{pmatrix} = \begin{pmatrix} 0 \\ 0 \\ -\frac{G}{4} \end{pmatrix}, \quad (6.20)$$

where  $E$  is the Young's modulus,  $\nu$  is Poisson's ratio, and  $V$  is the volume of the original tetrahedron. We denote the above equation as:

$$\bar{K}\bar{\Delta} = \bar{G}, \quad (6.21)$$

Since  $\bar{K}$  is a diagonal matrix,  $u_1$  and  $v_1$  will be 0. This implies that the displacement of the top point only happens in  $z$  direction. Recall that our goal is to solve  $\bar{\Delta}$ . Since  $\bar{K}$  is a full rank matrix, we can simply solve the system by:

$$\bar{\Delta} = \bar{K}^{-1}\bar{G}. \quad (6.22)$$

For one tetrahedron, it seems to be very easy to solve it algebraically, but for other complex models, we should consider using numerical iteration methods. Here, we introduce a damping factor  $r \in (0, 1]$  to form the following iteration equation based on equation (6.22):

$$\bar{\Delta}^{(k+1)} = (1 - r)\bar{\Delta}^{(k)} + r\bar{K}(\bar{\Delta}^{(k)})^{-1}\bar{G}. \quad (6.23)$$

We may rewrite the method as:

$$\alpha(\bar{\Delta}) = (1 - r)\bar{\Delta} + r\bar{K}(\bar{\Delta})^{-1}\bar{G}. \quad (6.24)$$

Then rewrite the major iteration part as another function:

$$\beta(\bar{\Delta}) = \bar{K}(\bar{\Delta})^{-1}\bar{G}. \quad (6.25)$$

the algorithm is:

---

**Algorithm 9** iteration method for recovering the shape of the object without gravity

---

- 1: Compute the initial stiffness matrix of the object under gravity, and  $\bar{\Delta}^{(0)} = \mathbf{0}$ .
  - 2: At step  $k$ ,  $k=1,2,\dots$ , apply an extra gravity force  $\mathbf{G}$  and compute the reduced displacement vector  $\bar{\Delta}^{(k)}$  by using equation (6.22), which is based on the stiffness matrix  $\bar{K}(\bar{\Delta}^{(k-1)})$ . Then, apply  $-\bar{\Delta}^{(k)}$  to the current shape and compute the new reduced stiffness matrix  $\bar{K}(\bar{\Delta}^{(k)})$ .
  - 3:  $k = k + 1$ .
  - 4: Repeat steps 2 and 3 until the difference of the shapes in two consecutive steps are close enough.
- 

The iteration method comes down to solving a fixed point problem:

$$\bar{\Delta} = h(\bar{\Delta}), \quad (6.26)$$

where,

$$\begin{aligned} h(\bar{\Delta}) &= (1 - r)\bar{\Delta} + r\bar{K}(\bar{\Delta})^{-1}\bar{G} \\ &= (1 - r) \begin{pmatrix} u_1 \\ v_1 \\ w_1 \end{pmatrix} + r \begin{pmatrix} \frac{4(1+\nu)(w_1 - \tilde{z}_1)^2}{EV} & 0 & 0 \\ 0 & \frac{4(1+\nu)(w_1 - \tilde{z}_1)^2}{EV} & 0 \\ 0 & 0 & \frac{2(1+\nu)(2\nu-1)(w_1 - \tilde{z}_1)^2}{EV(\nu-1)} \end{pmatrix} \begin{pmatrix} 0 \\ 0 \\ -\frac{G}{4} \end{pmatrix} \\ &= \begin{pmatrix} (1 - r)u_1 \\ (1 - r)v_1 \\ (1 - r)w_1 - \frac{r(1+\nu)(2\nu-1)G(w_1 - \tilde{z}_1)^2}{2EV(\nu-1)} \end{pmatrix}. \end{aligned}$$

In the above,  $V$  is the volume of the original shape:

$$V = \frac{1}{3} \times \frac{1}{2} \times x_2 \times y_3 \times z_1 = \frac{\tilde{x}_2 \tilde{y}_3 (\tilde{z}_1 - w_1)}{6}. \quad (6.27)$$

Then,

$$h(\bar{\Delta}) = \begin{pmatrix} (1-r)u_1 \\ (1-r)v_1 \\ (1-r)w_1 + \frac{3r(1+\nu)(2\nu-1)G(w_1-\tilde{z}_1)}{E(\nu-1)\tilde{x}_2\tilde{y}_3} \end{pmatrix}. \quad (6.28)$$

To analyze the convergence of the iteration method, we should consider two conditions: a) the two-norm of the Jacobian matrix of function  $h$  in (6.28) with respect to  $\bar{\Delta}$  is less than a constant which is less than one; b)  $h$  maps a space  $M$  to itself.

Now, we consider about the first condition. Compute the Jacobian matrix of function  $h$  from equation (6.28) with respect to  $\bar{\Delta}$ :

$$\frac{\partial h(\bar{\Delta})}{\partial \bar{\Delta}} = \begin{pmatrix} 1-r & 0 & 0 \\ 0 & 1-r & 0 \\ 0 & 0 & 1-r + \frac{3r(1+\nu)(2\nu-1)G}{E(\nu-1)\tilde{x}_2\tilde{y}_3} \end{pmatrix}, \quad (6.29)$$

By definition, the two-norm of a matrix is the square root of the largest singular value. In this case, since the Jacobian is a diagonal matrix, the two-norm will be the absolute value of the largest diagonal entry. Now, since  $\nu < 0.5$ , the biggest entry in the Jacobian matrix is the last entry and it is positive. In order to converge, we derive:

$$1-r + \frac{3r(1+\nu)(2\nu-1)G}{E(\nu-1)\tilde{x}_2\tilde{y}_3} < 1. \quad (6.30)$$

After simplifying it, we obtain:

$$\frac{3(1+\nu)(2\nu-1)}{E(\nu-1)\tilde{x}_2\tilde{y}_3} G < 1. \quad (6.31)$$

Since  $G = mg$ , where  $g = 9.8N/kg$ , and  $\tilde{V} = \tilde{y}_3\tilde{z}_1/6$ , we can transform the above inequality to obtain a relation between density  $\tilde{\rho} = m/\tilde{V}$  and variable  $\tilde{z}_1$ :

$$\frac{3(1+\nu)(2\nu-1)}{E(\nu-1)\tilde{x}_2\tilde{y}_3} mg < 1. \quad (6.32)$$

Subsequently,

$$\frac{3(1+\nu)(2\nu-1)mg\tilde{z}_1/6}{E(\nu-1)\tilde{x}_2\tilde{y}_3\tilde{z}_1/6} < 1. \quad (6.33)$$

Substituting  $\tilde{V}$  into the above inequality,

$$\frac{(1+\nu)(2\nu-1)mg\tilde{z}_1}{2E(\nu-1)\tilde{V}} < 1. \quad (6.34)$$

Plug in  $\tilde{\rho} = m/\tilde{V}$ ,

$$\frac{(1+\nu)(2\nu-1)g\tilde{z}_1\tilde{\rho}}{2E(\nu-1)} < 1, \quad (6.35)$$

After simplification, we obtain:

$$\tilde{\rho} < \frac{2E(\nu-1)}{(1+\nu)(2\nu-1)g\tilde{z}_1}. \quad (6.36)$$

Thus, if the density of a single tetrahedron is within which the above inequality holds, then the numerical method will satisfy convergence condition a).

Finally, we consider the convergence condition b). In our algorithm, since we apply an extra gravity force at the beginning, the first step displacement happens only in the  $z$  direction, which means  $u_1^{(0)}$  and  $v_1^{(0)}$  will be 0. From equation (6.28), we know that in any step  $k$ ,  $u_1^{(k)}$  and  $v_1^{(k)}$  will always be 0. Therefore the displacement happens only in  $z$  direction, which is  $w_1$ .

In other words, we only analyze the third element in equation (6.28), and see if we will find a interval of  $w_1$  that maps to the same range interval of the third element. We rewrite this element as a line equation with variable  $w_1$ :

$$\begin{aligned} h(\bar{\Delta})(3) &= (1-r)w_1 + \frac{3r(1+\nu)(2\nu-1)G(w_1 - \tilde{z}_1)}{E(\nu-1)\tilde{x}_2\tilde{y}_3} \\ &= \left(1-r + \frac{3r(1+\nu)(2\nu-1)G}{E(\nu-1)\tilde{x}_2\tilde{y}_3}\right)w_1 - \frac{3r(1+\nu)(2\nu-1)G}{E(\nu-1)\tilde{x}_2\tilde{y}_3}z_1 \end{aligned} \quad (6.37)$$

We can treat  $\gamma = \alpha(w_1)$  as a function, which is a line in the  $w_1$ - $\gamma$  plane. It's clear that the  $y$ -intercept is negative, and the slope is positive. Therefore, only when the slope is less than one, after several iterations, the interval of  $w_1$  can be mapped to a smaller interval, which satisfies condition b):

$$1-r + \frac{3r(1+\nu)(2\nu-1)G}{E(\nu-1)\tilde{x}_2\tilde{y}_3} < 1 \quad (6.38)$$

Hence, we notice that the above inequality is exactly the same as inequality (6.30). The rest of analysis here is the same as inequalities (6.31) to (6.36).

Also, since our goal is to find the interval that the function maps it to itself, we can consider about the line  $\gamma = w_1$  intersect with the line  $\gamma = \alpha(w_1)$ . Then for any  $d \leq w_1^*$ , the region  $D = [d, 0]$  will satisfy our requirement (b). Figure (6.6) illustrate it:

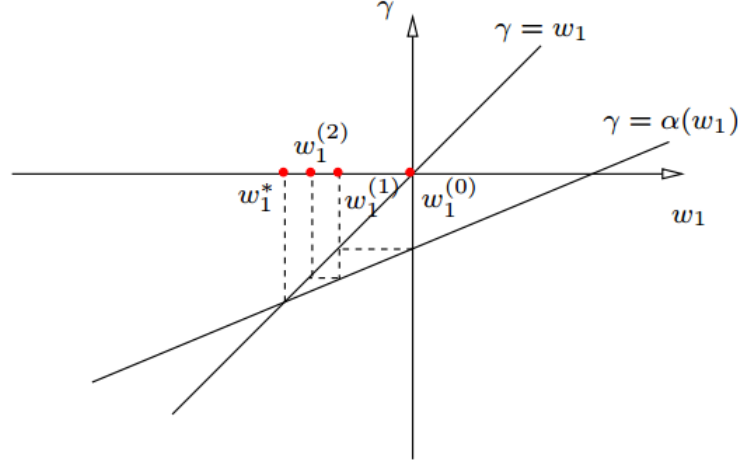


Figure 6.6: Convergence analysis of single tetrahedron

Therefore, combine condition a) and b), the sufficient condition for the iteration method to converge is:

$$\tilde{\rho} < \frac{2E(\nu - 1)}{(1 + \nu)(2\nu - 1)gz_1}. \quad (6.39)$$

Let's see the numerical simulation result of the iteration method applied on a single tetrahedron. Here, we chose Young's modulus  $E = 5 \times 10^3$ , mass 0.0765, density  $10^3$ , and Poisson's ratio  $\nu = 0.3$ . The vertices of the tetrahedron are:  $\tilde{\mathbf{p}}_1 = (\sqrt{3}, 1, 2\sqrt{2})^T/40$ ,  $\tilde{\mathbf{p}}_2 = (\sqrt{3}/20, 0, 0)^T$ ,  $\tilde{\mathbf{p}}_3 = (\sqrt{3}, 3, 0)^T/40$ ,  $\tilde{\mathbf{p}}_4 = (0, 0, 0)$ ,

The figure 6.7 illustrates several more examples and comparisons between iteration steps and parameter  $r$ .

The result we got is  $w_1 \approx -0.00435467$ . It tells us the gravity free shape of the tetrahedron would be the top vertex moves up for  $-w_1$ . We can also get the result of the bottom three inner forces of each of the vertex. The result will be listed after figure 6.7.

Table 6.3: Convergence condition (b) analysis

	$r = 1$	$r = 0.5$
$\tilde{\rho}$	# iters	# iters
$10^2$	4	10
$5 \times 10^2$	4	14
$10^4$	6	17
$2 \times 10^3$	11	27

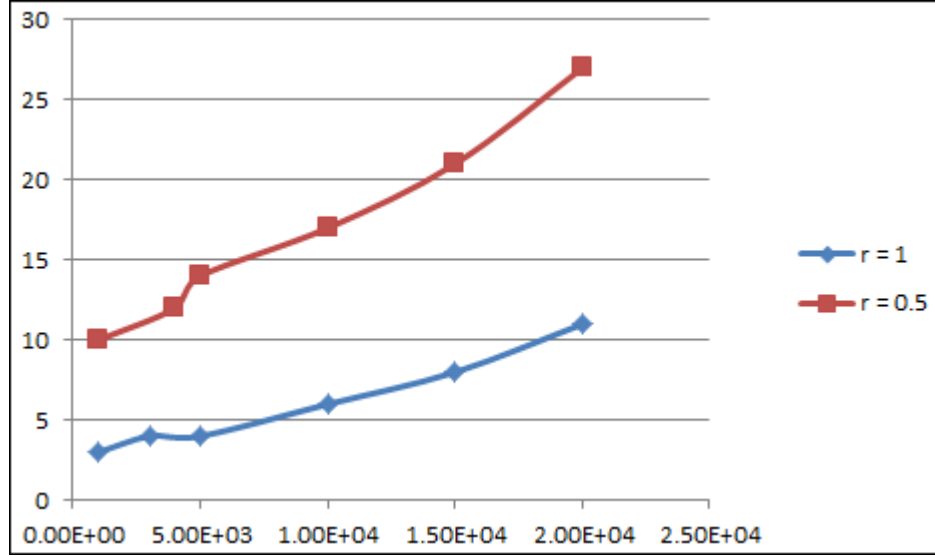


Figure 6.7: Iteration comparisons

$$\begin{aligned}
(f_{2x}, f_{2y}, f_{2z})^T &\approx (-0.0694, 0.04, 0.25)^T \\
(f_{3x}, f_{3y}, f_{3z})^T &\approx (0, -0.08, 0.25)^T \\
(f_{4x}, f_{4y}, f_{4z})^T &\approx (0.0694, 0.04, 0.25)^T
\end{aligned} \tag{6.40}$$

Then, the ratio between the magnitudes of the tangential forces and normal forces at each of the tetrahedron vertex  $\mathbf{p}_2, \mathbf{p}_3, \mathbf{p}_4$  will be:

$$\text{ratio 2 : } \frac{\sqrt{f_{2x}^2 + f_{2y}^2}}{f_{2z}} \approx \frac{(-0.0694)^2 + (0.04)^2}{0.25} = 0.320494$$

$$\begin{aligned}
\text{ratio 3 : } \frac{\sqrt{f_{3x}^2 + f_{3y}^2}}{f_{3z}} &\approx \frac{(0)^2 + (-0.08)^2}{0.25} = 0.320494 \\
\text{ratio 4 : } \frac{\sqrt{f_{4x}^2 + f_{4y}^2}}{f_{4z}} &\approx \frac{(0.0694)^2 + (0.04)^2}{0.25} = 0.320494
\end{aligned} \tag{6.41}$$

Therefore, the result of the ratios is consistent with what we thought. They are the same number due to the symmetry of the shape of the tetrahedron. Some frictional forces are needed to keep the tetrahedron to stay on the table.

### 6.3.3 General shape

#### 6.3.3.1 Jacobian under 2-norm

The iteration function is

$$\boldsymbol{\alpha}(\boldsymbol{\Delta}) = \boldsymbol{\Delta}' = (1 - r)\boldsymbol{\Delta} + r\bar{K}^{-1}(\boldsymbol{\Delta})\bar{\mathbf{G}}, \tag{6.42}$$

which is based on equation 6.23, where  $r \in (0, 1]$  is the parameter,  $\bar{K}$  is the reduced stiffness matrix, and  $\bar{\mathbf{G}}$  is the reduced gravity vector. It is not hard to see that the gravity on each node is constant due to our way of distributing the gravity, it is proportional to the density  $\rho$ , let us denote

$$\bar{\mathbf{G}} = \check{\mathbf{G}}\rho, \tag{6.43}$$

and  $\check{\mathbf{G}}$  is a vector with the same size as  $\bar{\mathbf{G}}$ . Also, given that the stiffness matrix is scaled by Young's Modulus  $E$ , denote

$$\bar{K} = E\check{K}, \tag{6.44}$$

we will get:

$$\bar{K}^{-1} = \frac{1}{E}\check{K}^{-1}. \tag{6.45}$$

Let  $s = \rho/E$ ,

$$\boldsymbol{\Delta}' = (1 - r)\boldsymbol{\Delta} + rs\check{K}^{-1}\check{\mathbf{G}}. \tag{6.46}$$

It would be interesting for us to know about the convergence of the iteration method for general model. In the next part, we will discuss about the condition that the two norm of the

Jacobian being less than one, which is one of the sufficient conditions for the iteration method to converge. The Jacobian of  $\Delta'$  is

$$J[\Delta'] = (1-r)I + rsJ[\check{K}^{-1}\check{G}]. \quad (6.47)$$

Denote  $J_\beta = J[\check{K}^{-1}\check{G}]$ . The 2-norm of the Jacobian is

$$\begin{aligned} \|J[\Delta']\|_2 &= \|(1-r)I + rsJ_\beta\|_2 \\ &= \max_{\mathbf{x}} \|(1-r)I + rsJ_\beta\mathbf{x}\|_2 \\ &= \max_{\mathbf{x}} \|(1-r)\mathbf{x} + rsJ_\beta\mathbf{x}\|_2, \end{aligned} \quad (6.48)$$

where  $\mathbf{x}$  is a unit vector.<sup>2</sup> Suppose the eigenvectors of  $J_\beta$  are  $\mathbf{v}_1, \mathbf{v}_2, \dots, \mathbf{v}_{3n-9}$ , and the corresponding eigenvalues are  $\lambda_1, \lambda_2, \dots, \lambda_{3n-9}$ . So

$$\mathbf{x} = \sum_{i=1}^{3n-9} (\mathbf{v}_i^T \mathbf{x}) \mathbf{v}_i. \quad (6.49)$$

Set  $p_i = \mathbf{v}_i^T \mathbf{x}$ , and plug in the Equation 6.49,

$$\begin{aligned} \|J[\Delta']\|_2 &= \max_{\mathbf{x}} \|(1-r) \sum_{i=1}^{3n-9} p_i \mathbf{v}_i + rs \sum_{i=1}^{3n-9} \lambda_i p_i \mathbf{v}_i\|_2 \\ &= \max_{\mathbf{x}} \left\| \sum_{i=1}^{3n-9} (1-r + rs\lambda_i) p_i \mathbf{v}_i \right\|_2 \\ &= \max_{\mathbf{x}} \sqrt{\sum_{i=1}^{3n-9} (1-r + rs\lambda_i)^2 p_i^2} \\ &= \max_i |1-r + rs\lambda_i|. \end{aligned} \quad (6.50)$$

Since  $\sum_{i=1}^{3n-9} p_i^2 = 1$ , we can get to the last step.

Let  $\lambda_{\max}$  be the maximum eigenvalue and  $\lambda_{\min}$  be the minimum eigenvalue. Fix  $s$ , and define a group of lines with respect to  $r$ :

$$f_i(r) = 1 + (s\lambda_i - 1)r \quad (6.51)$$

---

<sup>2</sup>Proof and analysis was provided by Feng Guo.



this group of line segments will be bounded by the following two because of the restrictions limit on  $\lambda_{\max}$  and  $\lambda_{\min}$

$$\begin{aligned} f_{\max}(r) &= 1 + (s\lambda_{\max} - 1)r \\ f_{\min}(r) &= 1 + (s\lambda_{\min} - 1)r \end{aligned} \quad (6.52)$$

i.e.  $f_{\min} \leq f_i \leq f_{\max}, \forall r \in (0, 1]$ . This suggests that

$$\|J[\Delta']\|_2(r) = \max(|f_{\min}|, |f_{\max}|). \quad (6.53)$$

The following discussions will be dependent on the values of  $\lambda_{\max}$  and  $\lambda_{\min}$ .

1. When  $\lambda_{\max} \geq \frac{1}{s}$ ,  $\|J[\Delta']\|_2 \geq f_{\max} \geq 1, \forall r \in (0, 1]$ .
2. When  $0 \leq \lambda_{\max} < \frac{1}{s}$  and  $\lambda_{\min} \geq -\lambda_{\max}, \forall r \in (0, 1], \|J[\Delta']\|_2 = f_{\max} < 1$ . The optimal value of  $\|J[\Delta']\|_2^* = s\lambda_{\max}$  will be reached at  $r^* = 1$ .

**Proof** When  $\lambda_{\min} \geq 0, \forall r \in (0, 1], 0 \leq f_{\min} \leq f_{\max}$ . The minimum of  $\|J[\Delta']\|_2$  is reached when  $r = 1$ .

When  $-\lambda_{\max} \leq \lambda_{\min} < 0$ ,

$$|f_{\max}(1)| = s\lambda_{\max} \geq -s\lambda_{\min} = |f_{\min}(1)|$$

So  $\forall r \in (0, 1], f_{\max} \geq f_{\min}$ . □

3. When  $\lambda_{\max} < \frac{1}{s}$  and  $\lambda_{\min} < -\lambda_{\max}$ ,

$$r^* = \frac{2}{2 - s(\lambda_{\min} + \lambda_{\max})},$$

that's when the minimum is achieved.

$$\|J[\Delta']\|_2^* = \frac{s(\lambda_{\max} - \lambda_{\min})}{2 - s(\lambda_{\max} + \lambda_{\min})}$$

For the other situations, the proof will be similar to the previous one.

- (a)  $\lambda_{\min} > -\frac{1}{s}$ ,  $r$  can be any value in  $(0, 1]$ ;
- (b)  $\lambda_{\min} \leq -\frac{1}{s}$ ,  $r$  can only be values in  $(0, \frac{2}{1-s\lambda_{\min}})$ .

In summation, when  $\lambda_{\max} \leq 0$ , given any  $s$ , there always exists some  $r$  so that the iteration can converge.

$$\begin{aligned}
\|J[\Delta']\|_2^* &= \frac{\lambda_{\max} - \lambda_{\min}}{2/s - (\lambda_{\max} + \lambda_{\min})} \\
&< -\frac{\lambda_{\max} - \lambda_{\min}}{\lambda_{\max} + \lambda_{\min}} \\
&= 1 - \frac{2\lambda_{\max}}{\lambda_{\max} + \lambda_{\min}} \\
&\leq 1.
\end{aligned} \tag{6.54}$$

### 6.3.3.2 Analysis of the Jacobian with 1-norm or $\infty$ -norm

The computing time of the eigenvalues of  $J_\beta$  will be long. Therefore, we may take a look at the other norms to see if there can be any difference. For example, to compute the 1-norm or  $\infty$ -norm, we only have to go through all the elements in  $J_k$ , which may help us save a copious amount of time in computing.

By definition, the 1-norm ( $\infty$ -norm) of a matrix is the maximum of the matrix's absolute column (row) sum. So the 1-norm is:

$$\kappa_i = \sum_{j \neq i} |A_{ji}| \tag{6.55}$$

the  $\infty$ -norm be:

$$\kappa_i = \sum_{j \neq i} |A_{ij}| \tag{6.56}$$

where  $A_{ij}$  is the element of  $A$  on the  $i$ -th row and  $j$ -th column. To simplify the notation, in the following analysis we denote  $A = J_\beta$ .

Then

$$\begin{aligned}
\|J[\Delta']\| &= \|(1-r)I + rsA\| \\
&= \max_i \||1-r + rsA_{ii}| + rs\kappa_i\|
\end{aligned} \tag{6.57}$$

Let

$$g_i = |1 - r + rsA_{ii}| + rs\kappa_i,$$

then if  $A_{ii} \geq 0$ ,

$$g_i = r[s(A_{ii} + \kappa_i) - 1] + 1, \tag{6.58}$$

and if  $A_{ii} < 0$ ,

$$g_i = \begin{cases} r[s(\kappa_i + A_{ii}) - 1] + 1, & r \in (0, \frac{1}{1-sA_{ii}}] \\ r[s(\kappa_i - A_{ii}) + 1] - 1, & r \in (\frac{1}{1-sA_{ii}}, 1] \end{cases} \quad (6.59)$$

Clearly that for all  $i = 1, \dots, 3n - 9$ ,  $g_i \geq 0$ .

Let  $a = \max_i(\kappa_i + A_{ii})$ , and  $b = \max_j(\kappa_j - A_{jj})$ , where  $j \in \{x \in Z^+ | x \leq 3n - 9 \text{ and } A_{xx} < 0\}$ , then it's not hard to see that  $\|J[\Delta']\| = \max\{r(sa - 1) + 1, r(sb + 1) - 1\}$ .

Depending on the values of  $a$  and  $b$ , there are several cases:

1. When  $a \geq \frac{1}{s}$ ,  $\|J[\Delta']\| \geq 1$ .
2. When  $a < \frac{1}{s}, b \leq a$ ,  $\|J[\Delta']\| = r(sa - 1) + 1 < 1$ . With  $r^* = 1$ , and  $\|J[\Delta']^*\| = sa$ .
3. When  $a < \frac{1}{s}, b > a$ ,

$$\|J[\Delta']\| = \begin{cases} r(sa - 1) + 1, & r \in (0, \frac{2}{s(b-a)+2}] \\ r(sb + 1) - 1, & r \in (\frac{2}{s(b-a)+2}, 1] \end{cases} \quad (6.60)$$

Here  $r^* = \frac{2}{s(b-a)+2}$ , where  $\|J[\Delta']\|^* = \frac{s(a+b)}{s(b-a)+2}$ . The range of possible  $r$  could be

- (a)  $(0, 1]$ , when  $b < \frac{1}{s}$
- (b)  $(0, \frac{2}{sb+1})$ , when  $b \geq \frac{1}{s}$

Suppose  $a = \kappa_h + A_{hh}$ , and  $b = \kappa_l - A_{ll}$ . Note that

$$\begin{aligned} r^* &= \frac{2}{s(b-a)+2} \\ &= \frac{2}{s(\kappa_l - A_{ll} - \kappa_h - A_{hh}) + 2} \\ &= \frac{2}{s(\kappa_l + A_{ll} - \kappa_h - A_{hh} - 2A_{ll}) + 2} \\ &\geq \frac{2}{-2sA_{ll} + 2} \\ &= \frac{1}{1 - sA_{ll}}. \end{aligned}$$

It is not hard for one to tell that the  $r^*$  value is always a constant value, and it lies in the valid range of  $[\frac{1}{1-sA_{ii}}, 1]$ .

### 6.3.4 Simulation, experiment and results

Based on the result from previous section, to do a little bit transformation, we can get the Jacobian matrix in general norm with the following, here  $\mathbf{x}$  is a very small vector:

$$\|J_\alpha\| = \|J\| \approx \max \frac{\|(1-r)\mathbf{x} + r(\boldsymbol{\beta} - K^{-1}K(\boldsymbol{\Delta} + \mathbf{x})\boldsymbol{\beta})\|}{\|\mathbf{x}\|}, \quad (6.61)$$

where

$$\boldsymbol{\beta}(\boldsymbol{\Delta}) = K^{-1}(\boldsymbol{\Delta})\mathbf{G}. \quad (6.62)$$

We did the numerical simulation on a ball with radius 0.05, density 700, Young's modulus  $2.5 \times 10^5$ , and Poisson's ratio 0.3. The figure 6.8 shows us the ball deformed under gravity sitting on the table with one triangle facet contacting with the table. The three vertices were fixed. There are in total 367 vertices, 1144 tetrahedrons and 2613 triangular facets. The result of the computed  $\boldsymbol{\Delta}$  was 0.239769 in 2-norm.

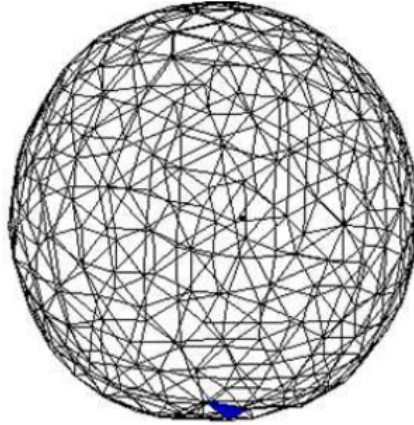


Figure 6.8: A ball sitting on a table under gravity

The next figure shows us during the process, we compare the approximated Jacobian norm  $\frac{\|J_\alpha \mathbf{x}\|}{\|\mathbf{x}\|}$  with respect to iteration steps between different  $r$  values. Each of the curve below represents different executions. Here, we take the  $\mathbf{x} = \boldsymbol{\Delta}^{(l)} - \boldsymbol{\Delta}^{(l-1)}$ , and also evaluate the value of Jacobian approximately at  $\boldsymbol{\Delta}^{(l-1)}$ .

From the figure 6.9 we can see that the iteration method succeed with the parameter  $r = 0.5$  but failed with the parameter  $r = 1$ . The plot of the curve with respect to  $r = 1$  goes dramatically up at the end. But the iteration method parameter  $r = 0.5$  curve goes to zero at

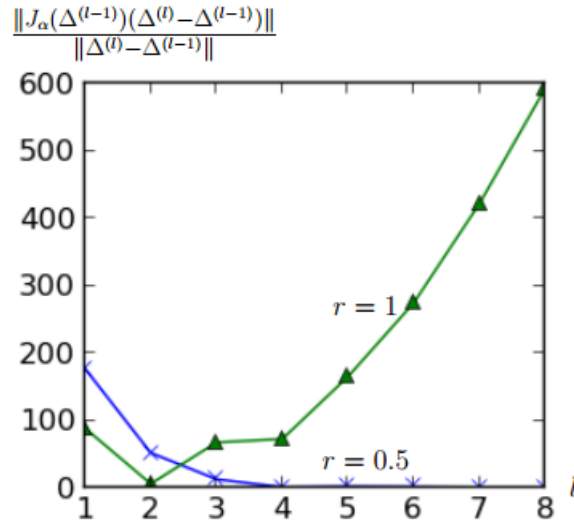


Figure 6.9: Curves from the simulation

the end, which means the norm of the Jacobian matrix should be within a small range, and thus the convergence of the iteration method in this situation would be convergent.

In order to prove our gravity free recover helps the accuracy of computing deformations of objects, we have conducted several experiments. In the experiment, the gelatin with name brand "Jell-O" was used. We use the 3D scanner to get the tetrahedron mesh of the gelatin, then use the iteration numerical method to recover the shape under gravity free situation. Finally we wanted to flip the jelly, and predict the shape under gravity by using the old FEM stiffness matrix model and also our recovered shape stiffness matrix model. The original picture of the jelly will be shown below.



Figure 6.10: Gelatin pudding

The gelatin is in a bowl shape as shown in figure 6.10. We put it bottom up on a platform, the bigger disk surface is in contacting with the plane. The 3D scanner we used was from NextEngine, Inc., and to simplify the mesh using MeshLab (<http://meshlab.sourceforge.net/>). The measured Young's modulus of this gelatin was  $3 \times 10^3$ , the Poisson's ratio was 0.4, the density was  $9.6 \times 10^2$ . The picture of the gelatin under gravity with the mesh output from the scanner, and then our predicted gelatin shape in the mesh are:

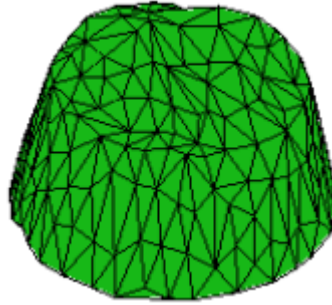


Figure 6.11: Mesh representation of the pudding

The mesh we got from the 3D scanner was then transformed using the code from Computational Geometry Algorithm Library (<http://www.cgal.org/>) into the tetrahedron mesh we needed with 1119 vertices and 1012 facets. In total there were 5152 tetrahedra inside the body of the model.

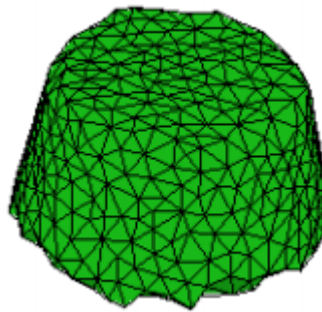


Figure 6.12: Gelatin with recovered shape mesh

Using the same assumption that the vertices on the face that contacting the platform were fixed, we restored the shape of the gelatin by using the iteration numerical method we have introduced. The iteration parameter  $r$  was set to be 1, so the major part of the iteration

function will be  $\beta$  from equation (6.25). The total number of iteration steps is 8 by applying the criteria that  $\|\Delta^{(k+1)} - \Delta^{(k)}\| < 10^{-6}$ . The detailed table of the data is in table 6.4:

Table 6.4: Information of measurements

	height	top diam.	bot. diam.	volume
original	0.031	0.050	0.062	$7.68 \times 10^{-5}$
original (gravity-free)	0.034	0.050	0.060	$7.8 \times 10^{-5}$
flipped	0.031	0.057	0.056	$7.6 \times 10^{-5}$
flipped (gravity)	0.028	0.062	0.051	$7.4 \times 10^{-5}$
flipped (gravity-free)	0.030	0.060	0.050	$7.5 \times 10^{-5}$

The figures of the flipped gelatin in real, triangulated mesh, predicted mesh by old stiffness matrix model and the predicted shape by using recovering gravity free shape model are shown in figure 6.13.

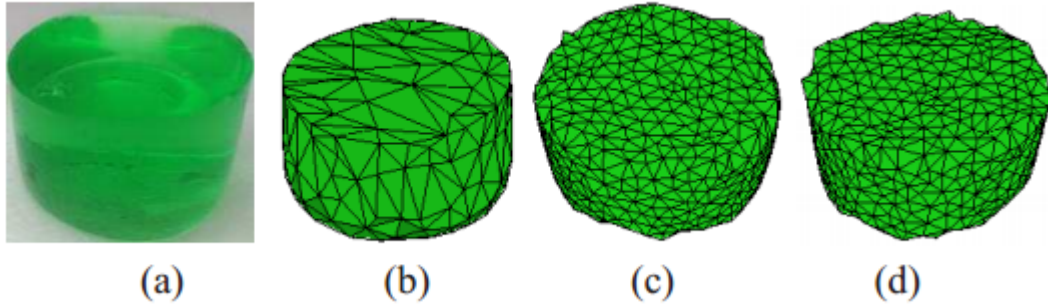


Figure 6.13: Flipped gelatin in (a) original. (b) original shape triangulation. (c) predicted shape using old stiffness matrix model. (d) predicted shape using gravity-free model

There are more figures <sup>3</sup> shown below for us to analyze the data. We plot the 2-norm of the vector  $\Delta$  during the iteration. This measures the difference between the current gelatin shape with the observed gelatin. At the end of the iteration, we can use the observed gelatin shape add the vector  $\Delta$  to get the recovered gravity-free shape of the gelatin. These figures are shown in figure 6.14 and in figure 6.15

<sup>3</sup>The simulation and experiment figures were provided by Huan Lin.

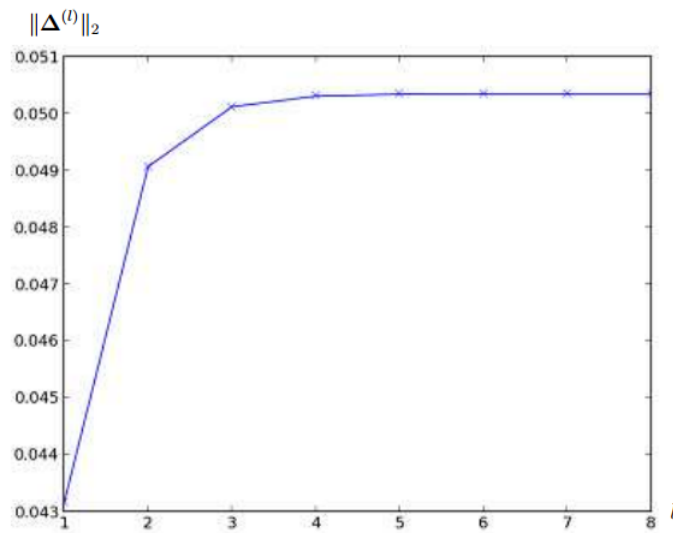


Figure 6.14: 2-norm of the vector  $\Delta$  during the iterations at  $l$ th step

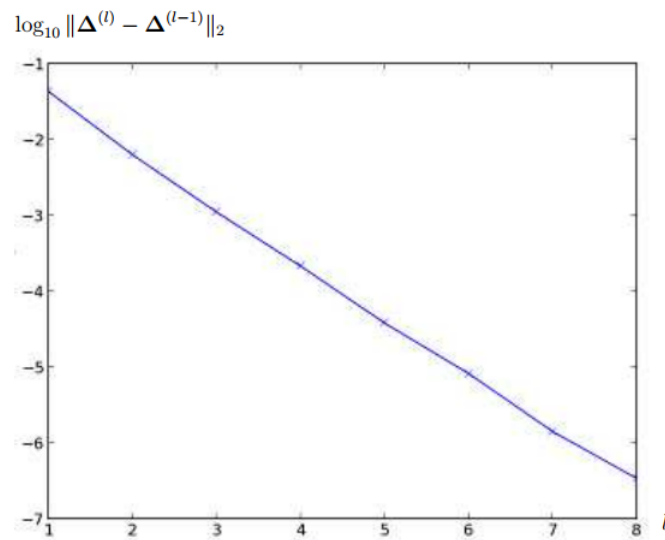


Figure 6.15: 2-norm of the logarithm of difference between the vector  $\Delta$  in two consecutive steps during the iterations



## CHAPTER 7. SUMMARY AND DISCUSSION

This thesis presented results of computational models for impact outcome for two-body and multi-body impact; proposed strategies for finding initial contact velocity in robotic planning task; Discussed coefficient of restitution of elastic rod bouncing problem; Studied the deformation and grasping task for soft objects in 3D.

In Chapter 2 and 3, the algorithm of computing the impact outcome for two-body collisions was shown in Algorithm 1 combining closed form analysis and numerical iterations. For multi-body collisions, the outcome was computed numerically based on impulse-impulse and energy-impulse differential relationships, which was shown in Algorithm 3.

In Chapter 4, for the sake of planning contact velocity in robotic batting tasks, both closed form solution in Algorithm 4 and numerical bounding triangle solution in subsection 4.4.4 were proposed. The closed form solution gave results instantly. However, we might not always be able to find solutions using closed form analysis. In the future, adjusting batting configurations to satisfy the existence of closed form solution should be considered. The numerical methods usually were able to find solutions. However, the convergence was not always guaranteed and it depended on the initialization. Thus, there could be more investigations on the convergence conditions for the numerical method.

In Chapter 5, a theorem regarding to the bouncing time of elastic rod hitting the ground with viscous damping was proved in Theorem 13. We observed that in some situations, the rod may not bounce. If there would be a bounce, then the bouncing time will be no earlier than a constant value. Computational results of the dependence of coefficient of restitution on the velocity and damping parameter can be seen from Fig. 5.4.

In Chapter 6, the strategy of picking up soft 3D objects with two robot fingers was shown in Algorithm 7. We used the liftability test to verify if an object can be picked up successfully

at each iteration. The results of comparisons between experiment and simulation were in Fig. 6.3, and it showed a closed match for different objects.

There is also prospective work that can be considered in the future: including but not limited to, a more in-depth understanding of the convergence of the numerical method being applied on a general model multi-body collision model, how to manipulate impact configuration to ensure the applicability of closed form solutions in planning contact velocity batting task, the difference when applying structural damping than viscous damping in the elastic rod impact modeling, and how the softness of the object affects the result of picking up strategies.

## APPENDIX A. STIFFNESS MATRIX CONSTRUCTION

In a 3D body under a displacement field  $(u, v, w)$ , the strain energy density is given as

$$U_0 = \frac{1}{2}(\sigma_x \epsilon_x + \sigma_y \epsilon_y + \sigma_z \epsilon_z + \tau_{xy} \gamma_{xy} + \tau_{yz} \gamma_{yz} + \tau_{zx} \gamma_{zx}) \quad (\text{A.1})$$

where

$$\epsilon_x = \partial u / \partial x$$

$$\epsilon_y = \partial v / \partial y$$

$$\epsilon_z = \partial w / \partial z$$

$$\gamma_{xy} = \partial u / \partial y + \partial v / \partial x$$

$$\gamma_{yz} = \partial v / \partial z + \partial w / \partial y$$

$$\gamma_{zx} = \partial w / \partial x + \partial u / \partial z$$

are strains, and

$$\sigma_x = \frac{E}{(1 + \nu)(1 - 2\nu)} [(1 - \nu)\epsilon_x + \nu\epsilon_y + \nu\epsilon_z] \quad (\text{A.2})$$

$$\sigma_y = \frac{E}{(1 + \nu)(1 - 2\nu)} [\nu\epsilon_x + (1 - \nu)\epsilon_y + \nu\epsilon_z] \quad (\text{A.3})$$

$$\sigma_z = \frac{E}{(1 + \nu)(1 - 2\nu)} [\nu\epsilon_x + \nu\epsilon_y + (1 - \nu)\epsilon_z] \quad (\text{A.4})$$

$$\tau_{xy} = \frac{E}{2(1 + \nu)} \gamma_{xy} \quad (\text{A.5})$$

$$\tau_{yz} = \frac{E}{2(1 + \nu)} \gamma_{yz} \quad (\text{A.6})$$

$$\tau_{zx} = \frac{E}{2(1 + \nu)} \gamma_{zx} \quad (\text{A.7})$$

are stresses, and  $E$  and  $\nu$  are Young's Modulus and Poisson's ratio.

Substitute Equations (A.2) to (A.7) in Equation (A.1),

$$U_0 = \frac{E}{4(1+\nu)} \int_V \left[ \frac{2(1-\nu)}{1-2\nu} (\epsilon_x^2 + \epsilon_y^2 + \epsilon_z^2) + \frac{4\nu}{1-2\nu} (\epsilon_x\epsilon_y + \epsilon_y\epsilon_z + \epsilon_z\epsilon_x) + (\gamma_{xy}^2 + \gamma_{yz}^2 + \gamma_{zx}^2) \right] dV. \quad (\text{A.8})$$

Rewrite the inside integrals to be perfect squares, we get:

$$U_0 = \frac{E}{2(1+\nu)} \int_V \left[ \frac{\nu}{1-2\nu} (\epsilon_x + \epsilon_y + \epsilon_z)^2 + (\epsilon_x^2 + \epsilon_y^2 + \epsilon_z^2) + \frac{1}{2} (\gamma_{xy}^2 + \gamma_{yz}^2 + \gamma_{zx}^2) \right] dV. \quad (\text{A.9})$$

Suppose  $V_i = (x_i, y_i, z_i)^T$ , and  $d_i = (u_i, v_i, w_i)^T$ ,  $i = 1, 2, 3$  and 4 are the position and displacements of the vertices of a Tetrahedron respectively. Denote  $P$  the position, and  $d$  the displacement of a point inside the tetrahedron. They can be interpolated using Barycentric interpolation:

$$P = \sum_{i=1}^4 c_i (x_i, y_i, z_i)^T, \quad (\text{A.10})$$

$$d = \sum_{i=1}^4 c_i (u_i, v_i, w_i)^T \quad (\text{A.11})$$

where  $c_i$ 's are positive and  $\sum_{i=1}^4 c_i = 1$ . Substitute  $c_4 = 1 - \sum_{i=1}^3 c_i$  in Equations (A.10) and (A.11):

$$P = (x, y, z)^T = (x_4, y_4, z_4)^T + \sum_{i=1}^3 c_i (x_i - x_4, y_i - y_4, z_i - z_4)^T, \quad (\text{A.12})$$

$$d = (u, v, w)^T = (u_4, v_4, w_4)^T + \sum_{i=1}^3 c_i (u_i - u_4, v_i - v_4, w_i - w_4)^T. \quad (\text{A.13})$$

Taking partial derivatives with respect to  $c_1$ ,  $c_2$  and  $c_3$ , we get

$$\begin{bmatrix} \frac{\partial x}{\partial c_1} & \frac{\partial x}{\partial c_2} & \frac{\partial x}{\partial c_3} \\ \frac{\partial y}{\partial c_1} & \frac{\partial y}{\partial c_2} & \frac{\partial y}{\partial c_3} \\ \frac{\partial z}{\partial c_1} & \frac{\partial z}{\partial c_2} & \frac{\partial z}{\partial c_3} \end{bmatrix} = \begin{bmatrix} x_1 - x_4 & x_2 - x_4 & x_3 - x_4 \\ y_1 - y_4 & y_2 - y_4 & y_3 - y_4 \\ z_1 - z_4 & z_2 - z_4 & z_3 - z_4 \end{bmatrix} \quad (\text{A.14})$$

$$\begin{bmatrix} \frac{\partial u}{\partial c_1} & \frac{\partial u}{\partial c_2} & \frac{\partial u}{\partial c_3} \\ \frac{\partial v}{\partial c_1} & \frac{\partial v}{\partial c_2} & \frac{\partial v}{\partial c_3} \\ \frac{\partial w}{\partial c_1} & \frac{\partial w}{\partial c_2} & \frac{\partial w}{\partial c_3} \end{bmatrix} = \begin{bmatrix} u_1 - u_4 & u_2 - u_4 & u_3 - u_4 \\ v_1 - v_4 & v_2 - v_4 & v_3 - v_4 \\ w_1 - w_4 & w_2 - w_4 & w_3 - w_4 \end{bmatrix}. \quad (\text{A.15})$$

The absolute value of the determinant of the matrix in the right hand side of Equation (A.14) is 6 times the volume of the tetrahedron. Since the tetrahedrons have positive volume in this

case, the matrix is fully ranked, and its inverse exists. From Equation (A.14), we obtain

$$\begin{bmatrix} \frac{\partial c_1}{\partial x} & \frac{\partial c_1}{\partial y} & \frac{\partial c_1}{\partial z} \\ \frac{\partial c_2}{\partial x} & \frac{\partial c_2}{\partial y} & \frac{\partial c_2}{\partial z} \\ \frac{\partial c_3}{\partial x} & \frac{\partial c_3}{\partial y} & \frac{\partial c_3}{\partial z} \end{bmatrix} = \begin{bmatrix} \frac{\partial x}{\partial c_1} & \frac{\partial x}{\partial c_2} & \frac{\partial x}{\partial c_3} \\ \frac{\partial y}{\partial c_1} & \frac{\partial y}{\partial c_2} & \frac{\partial y}{\partial c_3} \\ \frac{\partial z}{\partial c_1} & \frac{\partial z}{\partial c_2} & \frac{\partial z}{\partial c_3} \end{bmatrix}^{-1} = \begin{bmatrix} x_1 - x_4 & x_2 - x_4 & x_3 - x_4 \\ y_1 - y_4 & y_2 - y_4 & y_3 - y_4 \\ z_1 - z_4 & z_2 - z_4 & z_3 - z_4 \end{bmatrix}^{-1} \quad (\text{A.16})$$

Let us go back to the strains,

$$\epsilon_x = \frac{\partial u}{\partial x} = \sum_{i=1}^3 \frac{\partial u}{\partial c_i} \frac{\partial c_i}{\partial x} = \sum_{i=1}^3 \frac{\partial c_i}{\partial x} (u_i - u_4) = \sum_{i=1}^3 \frac{\partial c_i}{\partial x} u_i - \sum_{i=1}^3 \frac{\partial c_i}{\partial x} u_4. \quad (\text{A.17})$$

Now  $\epsilon_x$  is represented by the displacements of the 4 vertices. Similarly, we represent all the (parts of) strain terms by the displacements of vertices as

$$\begin{bmatrix} \frac{\partial u}{\partial x} & \frac{\partial v}{\partial x} & \frac{\partial w}{\partial x} \\ \frac{\partial u}{\partial y} & \frac{\partial v}{\partial y} & \frac{\partial w}{\partial y} \\ \frac{\partial u}{\partial z} & \frac{\partial v}{\partial z} & \frac{\partial w}{\partial z} \end{bmatrix} = \begin{bmatrix} \frac{\partial c_1}{\partial x} & \frac{\partial c_2}{\partial x} & \frac{\partial c_3}{\partial x} & -\sum_{i=1}^3 \frac{\partial c_i}{\partial x} \\ \frac{\partial c_1}{\partial y} & \frac{\partial c_2}{\partial y} & \frac{\partial c_3}{\partial y} & -\sum_{i=1}^3 \frac{\partial c_i}{\partial y} \\ \frac{\partial c_1}{\partial z} & \frac{\partial c_2}{\partial z} & \frac{\partial c_3}{\partial z} & -\sum_{i=1}^3 \frac{\partial c_i}{\partial z} \end{bmatrix} \begin{bmatrix} u_1 & v_1 & w_1 \\ u_2 & v_2 & w_2 \\ u_3 & v_3 & w_3 \\ u_4 & v_4 & w_4 \end{bmatrix}. \quad (\text{A.18})$$

With Equation (A.18), we can assemble the stiffness matrix.

Denote  $Q$  the first matrix on the right-hand side of (A.18), and  $Q_{ij}$  its entry in row  $i$  and column  $j$ . Then

$$\epsilon_x = \frac{\partial u}{\partial x} = \sum_{i=1}^4 Q_{1i} u_i, \quad \epsilon_y = \frac{\partial v}{\partial y} = \sum_{i=1}^4 Q_{2i} v_i, \quad \text{and} \quad \epsilon_z = \frac{\partial w}{\partial z} = \sum_{i=1}^4 Q_{3i} w_i.$$

So

$$\epsilon_x^2 = (u_1, u_2, u_3, u_4) \begin{pmatrix} Q_{11}^2 & Q_{11}Q_{12} & Q_{11}Q_{13} & Q_{11}Q_{14} \\ Q_{12}Q_{11} & Q_{12}^2 & Q_{12}Q_{13} & Q_{12}Q_{14} \\ Q_{13}Q_{11} & Q_{13}Q_{12} & Q_{13}^2 & Q_{13}Q_{14} \\ Q_{14}Q_{11} & Q_{14}Q_{12} & Q_{14}Q_{13} & Q_{14}^2 \end{pmatrix} \begin{pmatrix} u_1 \\ u_2 \\ u_3 \\ u_4 \end{pmatrix}, \quad (\text{A.19})$$

$$\epsilon_y^2 = (v_1, v_2, v_3, v_4) \begin{pmatrix} Q_{21}^2 & Q_{21}Q_{22} & Q_{21}Q_{23} & Q_{21}Q_{24} \\ Q_{22}Q_{21} & Q_{22}^2 & Q_{22}Q_{23} & Q_{22}Q_{24} \\ Q_{23}Q_{21} & Q_{23}Q_{22} & Q_{23}^2 & Q_{23}Q_{24} \\ Q_{24}Q_{21} & Q_{24}Q_{22} & Q_{24}Q_{23} & Q_{24}^2 \end{pmatrix} \begin{pmatrix} v_1 \\ v_2 \\ v_3 \\ v_4 \end{pmatrix}, \quad (\text{A.20})$$

$$\epsilon_z^2 = (w_1, w_2, w_3, w_4) \begin{pmatrix} Q_{31}^2 & Q_{31}Q_{32} & Q_{31}Q_{33} & Q_{31}Q_{34} \\ Q_{32}Q_{31} & Q_{32}^2 & Q_{32}Q_{33} & Q_{32}Q_{34} \\ Q_{33}Q_{31} & Q_{33}Q_{32} & Q_{33}^2 & Q_{33}Q_{34} \\ Q_{34}Q_{31} & Q_{34}Q_{32} & Q_{34}Q_{33} & Q_{34}^2 \end{pmatrix} \begin{pmatrix} w_1 \\ w_2 \\ w_3 \\ w_4 \end{pmatrix}. \quad (\text{A.21})$$

On the other hand,

$$\begin{aligned} \gamma_{xy} &= \frac{\partial u}{\partial y} + \frac{\partial v}{\partial x} = \sum_{i=1}^4 (Q_{1i}v_i + Q_{2i}u_i), \\ \gamma_{yz} &= \frac{\partial v}{\partial z} + \frac{\partial w}{\partial y} = \sum_{i=1}^4 (Q_{3i}v_i + Q_{2i}w_i), \\ \gamma_{zx} &= \frac{\partial u}{\partial z} + \frac{\partial w}{\partial x} = \sum_{i=1}^4 (Q_{3i}u_i + Q_{1i}w_i). \end{aligned}$$

Let  $d_t = (u_1, v_1, w_1, \dots, u_4, v_4, w_4)^T$ . Then,

$$\gamma_{xy}^2 = \left( \sum_{i=1}^4 Q_{1i}v_i \right)^2 + \left( \sum_{i=1}^4 Q_{2i}u_i \right)^2 + 2 \left( \sum_{i=1}^4 Q_{1i}v_i \cdot \sum_{i=1}^4 Q_{2i}u_i \right) \quad (\text{A.22})$$

After we expand every term in equation A.9, we also know that

$$U_0 = \frac{1}{2} d_t^T K d_t, \quad (\text{A.23})$$

then we compare those two expansions to get the form of stiffness matrix  $K$ .

## APPENDIX B. NUMERICAL COMPUTATION OF $\mathcal{E}(t_1)$

In this appendix, we sketch the steps that were taken to numerically compute  $\mathcal{E}(t_1)$ , particularly when  $r \neq 0$  and  $t_b = t_1$ . Reviewing equation (5.55),

$$\mathcal{E}(t_1) = \frac{1}{2} \int_0^L (v_t(x, t_1)^2 + c^2 v_x(x, t_1)^2) dx + Lgh(t_1).$$

$h(t_1)$  can be calculated using (5.39) and (5.40) as shown in Section 5.3.1. Alternatively, (5.35) can be used once  $v_t(x, t_1)$  has been computed numerically. Then again use (5.40) to get  $h(t_1)$ . We need to compute  $v_t(x, t_1)$  and  $v_x(x, t_1)$ . The idea is to apply equations (C.14), (C.15) and (C.16) with  $v(x, t) = e^{-rt}w(x, t)$ ,  $\phi^e(y) = -\mu^e(y)$  and  $h^e(y, t - \tau) = -g^e(y)e^{r(t-\tau)}$ .

Thus,  $v_t(x, t_1)$  and  $v_x(x, t_1)$  can be computed from  $w(x, t_1)$ ,  $w_t(x, t_1)$  and  $w_x(x, t_1)$  as below:

$$\begin{aligned} v_t(x, t_1) &= -re^{-rt_1}w(x, t_1) + e^{-rt_1}w_t(x, t_1), \\ v_x(x, t_1) &= e^{-rt_1}w_x(x, t_1). \end{aligned}$$

The integrands for the terms  $w_t(x, t_1)$  and  $w_x(x, t_1)$  have discontinuities along characteristic lines  $ct = \pm(x - 2kL)$ ,  $k \in \mathbb{Z}$ . Consequently some care should be taken to evaluate the integrals correctly in the separate regions, which are defined by the characteristics, see Fig. B.1. For example, in order to compute  $w_t(x, t_1)$ , after using the definition of the extended functions  $\mu^e$  and  $g^e$ , and recall that  $\lambda = r/c$  and  $s(t, r) = \sqrt{c^2t^2 - r^2}$ , (C.15) becomes the following,

$$\begin{aligned} w_t(x, t_1) &= \frac{1}{2c} \left( c^2 t_1 \mu \lambda \int_{x-ct_1}^0 \frac{I_1(\lambda s(t_1, x-y))}{s(t_1, x-y)} dy - c^2 t_1 \mu \lambda \int_0^{2L} \frac{I_1(\lambda s(t_1, x-y))}{s(t_1, x-y)} dy \right. \\ &+ c^2 t_1 \mu \lambda \int_{2L}^{x+ct_1} \frac{I_1(\lambda s(t_1, x-y))}{s(t_1, x-y)} dy + 2c\mu \\ &+ g \int_{x-ct_1}^0 I_0(\lambda s(t_1, x-y)) s(t_1, x-y) dy - \int_0^{2L} I_0(\lambda s(t_1, x-y)) s(t_1, x-y) dy \\ &+ \int_{2L}^{x+ct_1} I_0(\lambda s(t_1, x-y)) s(t_1, x-y) dy \\ &\left. + r \int_0^{t_1} \int_{x-c\tau}^{x+c\tau} I_0(\lambda s(\tau, x-y)) (-g^e(y) e^{r(t_1-\tau)}) dy d\tau \right). \end{aligned}$$

We handle the last double integral as follows. Given a point  $(x, t_1)$ , where  $x \in (0, L)$ , the region of integration is the region in Fig. B.1 determined by characteristic lines emanating from point  $(x, t_1)$ . We write this integral as a sum of three integrals, based on their region of integration. In Fig. B.1, the purple regions correspond to  $g^e(x) = -g$ , while the green area corresponds

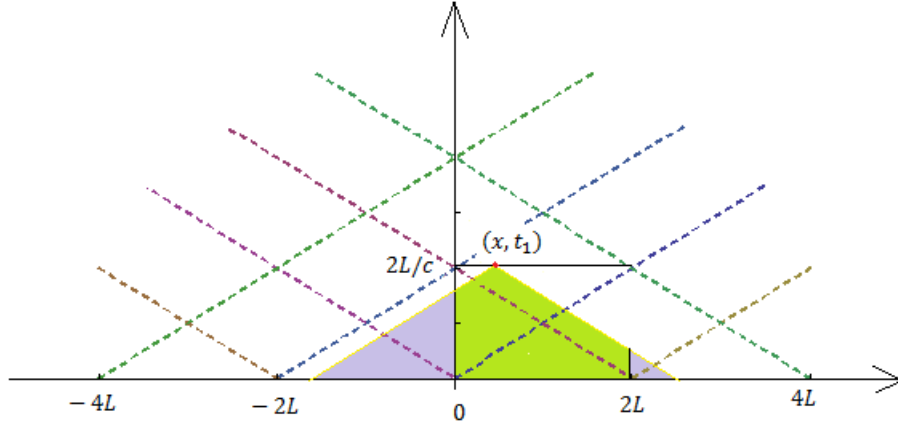


Figure B.1: Integration regions A, B and C.

to  $g^e(x) = g$ . Taking this geometry into consideration, the last term can be written as

$$\begin{aligned}
& r \int_0^t \int_{x-c\tau}^{x+c\tau} I_0(\lambda s(\tau, x-y)) (-g^e(y) e^{r(t-\tau)}) dy d\tau \\
&= 2(-r \int_{x-ct_1}^0 \int_0^{t_1 + \frac{y-x}{c}} (-g) I_0(\lambda s(t_1 - \tau, x-y)) e^{r\tau} d\tau dy) \\
&+ (-r \int_0^{t_1} \int_{x-c(t_1-\tau)}^{x+c(t_1-\tau)} (g) I_0(\lambda s(t_1 - \tau, x-y)) e^{r\tau} dy d\tau) \\
&+ 2(-r \int_{2L}^{x+ct_1} \int_0^{t_1 - \frac{y-x}{c}} (-g) I_0(\lambda s(t_1 - \tau, x-y)) e^{r\tau} d\tau dy).
\end{aligned}$$

Similar explicit expressions for  $w(x, t_1)$  and  $w_x(x, t_1)$  can likewise be written down. Therefore,  $\mathcal{E}(t_1)$  can be expressed directly in terms of integrals that can be computed numerically using Mathematica.

As a benchmark, we computed  $\mathcal{E}(t_1)$  this way in the conservative case  $r = 0$ , and obtained the red curves in Fig. 5.6 and 5.7. The maximum error of each of them is on the order of 1% using Mathematica 10.3.



## APPENDIX C. ELASTIC ROD WITH STRUCTURAL DAMPING

Compare to Chapter 5, instead of using viscous damping, here we consider the following constant coefficient elastic rod with structural damping:

$$v_{tt} - 2rv_{xxt} - c^2v_{xx} = -g \quad x \in \Omega_L := (0, L), \quad t \in (0, +\infty), \quad (\text{C.1})$$

where in comparison to (5.1), we have divided the equation by  $\rho$  so that  $g \geq 0$  is the gravitational constant, and the wave speed  $c = \sqrt{\frac{\sigma}{\rho}}$  is positive. The structural damping term  $2rv_{xxt}$  ( $r \geq 0$ ) describes an internal damping force.

The rod is assumed to be stress-free at the end  $x = L$  and we impose Signorini boundary conditions at the end  $x = 0$ :

$$v_x(L, t) = 0, \quad t \in (0, +\infty), \quad (\text{C.2})$$

$$v_x(0, t) \leq 0, \quad t \in (0, +\infty), \quad (\text{C.3})$$

$$v(0, t) \geq 0, \quad t \in (0, +\infty), \quad (\text{C.4})$$

$$v(0, t)v_x(0, t) = 0, \quad t \in (0, +\infty). \quad (\text{C.5})$$

In our formulation of this problem, we assume that the rod impacts the ground at time 0 with constant initial velocity  $-\mu$ :

$$v(x, 0) = 0, \quad x \in \Omega_L, \quad (\text{C.6})$$

$$v_t(x, 0) = -\mu, \quad x \in \Omega_L, \quad (\text{C.7})$$

and with zero displacement from the reference configuration

$$X(x, 0) = x, \quad x \in [0, L],$$

thus the deformed position at time  $t$  is given by

$$X(x, t) = x + v(x, t). \quad (\text{C.8})$$

The Signorini boundary conditions (C.3)–(C.5) (also called unilateral constraints) essentially state that the bottom of the rod should be stress-free while not in contact with the ground and the Dirichlet condition  $v(0, t) = 0$  should be imposed when in contact with the ground.

For the present appendix, we only need to consider the time interval  $[0, t_b + \epsilon]$ , where  $[0, t_b]$  is the contact interval and  $\epsilon$  is sufficiently small so that there is at most one bounce. In this situation, solutions are classical except for jumps in the derivatives along certain characteristic rays due to the bounce. Here  $t_b$  (possibly  $= \infty$ ) is defined by

$$t_b = \sup\{t > 0 : v(0, \tau) = 0, \quad 0 \leq \tau < t\}. \quad (\text{C.9})$$

### Analysis of impact when $r = 0$

Some of the analysis in this section coincides with the analysis in chapter 5 for the case of  $r = 0$ . However, the solution formulas are simplified considerably here, since (C.11) is included for convenience. During the time interval  $[0, t_b]$ , (C.1)–(C.7) can be written as:

$$\begin{cases} v_{tt} - c^2 v_{xx} = -g, & (x, t) \in \Omega_L \times (0, t_b), \\ v(x, 0) = 0, \quad v_t(x, 0) = -\mu, & x \in \Omega_L, \\ v(0, t) = 0, \quad v_x(L, t) = 0, & t \in (0, t_b). \end{cases} \quad (\text{C.10})$$

As is well known, an explicit solution formula for (C.10) can be obtained using the reflection principle and D'Alembert's formula. We first define appropriate extensions of the data in ((C.10)) to all of  $\mathbb{R}$ . To this end, let  $1^e$  denote the odd, positive extension of the function  $f(x) = 1, x \in \Omega_{2L}$ , that is

$$1^e(x) = \begin{cases} 1, & x \in (2kL, 2(k+1)L), k \in \mathbb{Z}, \\ -1, & x \in ((2k-1)L, 2kL), k \in \mathbb{Z} \end{cases} \quad (\text{C.11})$$

We will also write  $\mu^e(x) := \mu 1^e(x)$ ,  $g^e(x) := g 1^e(x)$ . We use symmetry to extend the data in (C.12) to all of  $\mathbb{R}$ . To this end, given a function  $f : (0, 2L) \rightarrow \mathbb{R}$ , let  $\tilde{f} : (-2L, 2L) \setminus \{0\} \rightarrow \mathbb{R}$  be the odd extension of  $f$ , and define the *symmetric extension*  $f^e : \mathbb{R} \setminus 2L\mathbb{Z} \rightarrow \mathbb{R}$  as the periodic

extension of  $\tilde{f}$ . The solution of (C.10) coincides with solution of

$$\begin{cases} u_{tt} - c^2 u_{xx} = -g^e, & x \in \mathbb{R}, t \in (0, t_b), \\ u(x, 0) = 0, u_t(x, 0) = -\mu^e, & x \in \mathbb{R}. \end{cases} \quad (\text{C.12})$$

D'Alembert's formula (the non homogeneous version, see e.g. McOwen (1996)) gives

**Theorem 19** (C.12) has a unique weak solution  $v$  in  $C([0, T]; H_0^1[0, 2L])$ , and  $v_t$  in  $C([0, T]; L^2(0, 2L))$ ,

which is given point wise by

$$\begin{aligned} v(x, t) = & -\frac{1}{2c} \int_{x-ct}^{x+ct} \mu^e(y) dy \\ & -\frac{1}{2c} \int_0^t \int_{x-c\tau}^{x+c\tau} g^e(y) dy d\tau. \end{aligned} \quad (\text{C.13})$$

The solution above is continuous and continuously differentiable except on the characteristics  $ct = \pm(x - 2kL)$ ,  $k \in \mathbb{Z}$ , where the partial derivatives  $u_x$  and  $u_t$  could have jump discontinuities.

### Calculation of jumps along characteristics

In the case of interest, namely  $\varphi(x) = -\mu$  is a constant and  $h(x, t) = -g$  with  $x \in \Omega_{2L}$ . Therefore  $\varphi^e(x) = -\mu^e(x)$  and  $h(x, t)^e = -g^e(x)$ , where  $g^e(x)$  and  $\mu^e(x)$  denote the symmetric extensions defined on  $\mathbb{R} \setminus 2L\mathbb{Z}$  of the constant functions  $g, \mu$  (originally defined on  $(0, 2L)$ ). Let  $u(x, t)$  be the solution of (C.12) as given by (C.13). A calculation gives

$$\begin{aligned} u_x(x, t) = & \frac{1}{2c} (-\mu^e(x + ct) + \mu^e(x - ct)) \\ & + \frac{1}{2c} \int_0^t (-g^e(x + c(t - \tau)) + g^e(x - c(t - \tau))) d\tau. \end{aligned} \quad (\text{C.14})$$

Let  $\Xi^\pm$  denote the set of points  $(x, t)$  that are on the characteristics  $ct = \pm(x - x_0)$  emanating from points  $(x_0, 0)$  with  $x_0 \in 2L\mathbb{Z}$ , and let  $\Xi = \Xi^+ \cup \Xi^-$ . If  $\varphi$  is continuous on  $(0, 2L)$  but  $-\mu^e$  has jump discontinuities, then (C.14) remains valid for points  $(x, t) \notin \Xi$ . Let  $[\psi(x)] = \psi(x^+) - \psi(x^-)$  denote the jump of function  $\psi$  at  $x$ . For functions  $\beta(x, t)$  with jump discontinuities on the characteristics  $\Xi$ , define  $[\beta(x, t)]$  to be the jump of  $\beta$  at  $(x, t)$ , as a function of  $t$ , with  $x$  fixed.

Consider the case where  $(x, t) = (x_0 - ct, t) \in \Xi^- \setminus \Xi^+$ . Since the only contributions to  $[u_x(x, t)]$  are due to terms in the first line of (C.14), we have

$$[u_x(x, t)] = [u_x(x_0 - ct, t)] = \frac{1}{2c}([- \mu^e(x_0)] - [- \mu^e(x_0 - 2ct)]) = -\frac{1}{2c}[\mu^e(x_0)].$$

If instead,  $(x, t) = (x_0 + ct, t) \in \Xi^+ \setminus \Xi^-$ , noting that along these characteristics, crossing a characteristic in the  $t$  direction corresponds to the negative jump in the  $x$  direction. Hence

$$[u_x(x, t)] = [u_x(x_0 + ct, t)] = \frac{-1}{2c}([- \mu^e(2ct + x_0)] - [- \mu^e(x_0)]) = \frac{1}{2c}[- \mu^e(x_0)].$$

Similarly,

$$\begin{aligned} u_t(x, t) &= \frac{1}{2}(-\mu^e(x + ct) + -\mu^e(x - ct)) \\ &\quad + \frac{1}{2c} \int_{x-ct}^{x+ct} -g^e(y) dy \end{aligned} \tag{C.15}$$

We again can easily calculate  $[u_t]$ , the jump in  $u_t$  along the characteristics. If  $(x, t) \in \Xi^- \setminus \Xi^+$ , then

$$[u_t(x, t)] = [u_t(x_0 - ct, t)] = \frac{1}{2}([- \mu^e(x_0 - 2ct)] + [- \mu^e(x_0)]) = \frac{1}{2}[- \mu^e(x_0)].$$

If  $(x, t) \in \Xi^+ \setminus \Xi^-$ , then

$$[u_t(x, t)] = [u_t(x_0 + ct, t)] = \frac{-1}{2}([- \mu^e(x_0)] + [- \mu^e(x_0 + 2ct)]) = -\frac{1}{2}[- \mu^e(x_0)].$$

We summarize this calculation in the following.

**Proposition 20** *The solutions  $u(x, t)$  given in Proposition 19 satisfy the following properties:*

(i) *If  $(x, t) = (x_0 - ct, t) \in \Xi^- \setminus \Xi^+$ , then*

$$[u_x(x, t)] = \frac{1}{2c}[- \mu^e(x_0)], \quad [u_t(x, t)] = \frac{1}{2}[- \mu^e(x_0)].$$

(ii) *If  $(x, t) = (x_0 + ct, t) \in \Xi^+ \setminus \Xi^-$ , then*

$$[u_x(x, t)] = \frac{1}{2c}[- \mu^e(x_0)], \quad [u_t(x, t)] = -\frac{1}{2}[- \mu^e(x_0)].$$

(iii) *If  $(x, t) = (x_0 + ct, t) = (x_1 - ct, t) \in \Xi^+ \cap \Xi^-$ , then*

$$[u_x(x, t)] = \frac{[- \mu^e(x_0)] + [- \mu^e(x_1)]}{2c}, \quad [u_t(x, t)] = \frac{[- \mu^e(x_1)] - [- \mu^e(x_0)]}{2}.$$

### Calculation of contact time

We see from (5.13) and Proposition 19 that the solution  $v(x, t)$  to the original problem (C.10) is

$$\begin{aligned} v(x, t) &= u(x, t) \\ &= \frac{1}{2c} \int_{x-ct}^{x+ct} (-\mu^e(y)) dy; \\ &+ \frac{1}{2c} \int_0^t \int_{x-c\tau}^{x+c\tau} (-g^e(y)) dy d\tau. \end{aligned} \quad (\text{C.16})$$

Since  $v_x(0, t) = w_x(0, t)$ , boundary condition (C.3) holds if and only if  $w_x(0, t) \leq 0$ . Therefore, we compute  $w_x(0, t) = u_x(0, t)$  where  $u(x, t)$  is given by (C.13) with  $\varphi^e = -\mu^e$  and  $h^e = -g^e$ . We obtain

$$\begin{aligned} v_x(0, t) &= \frac{1}{2c}(-\mu^e(ct) + \mu^e(-ct)) \\ &+ \frac{1}{2c} \int_0^t -g^e(c\tau, t - \tau) + g^e(-c\tau, t - \tau) d\tau. \end{aligned} \quad (\text{C.17})$$

Assume for some  $k = k(t) \in \mathbb{N}_0 = \{0, 1, 2, \dots\}$  that

$$2Lk < ct < 2L(k+1),$$

or equivalently

$$t_1 k < t < t_1(k+1). \quad (\text{C.18})$$

We compute the first two terms in (C.17),

$$\begin{aligned} &\frac{1}{2c}(-\mu^e(ct) + \mu^e(-ct)) \\ &= -\mu^e(ct)/c \end{aligned} \quad (\text{C.19})$$

where on each interval  $t \in (t_1 k, t_1(k+1))$ , from (C.11)

$$1^e(ct) := \begin{cases} 1, & t \in (0, t_1 := \frac{2L}{c}), \\ 1 + 2 \sum_{j=1}^k (-1)^j & t \in (kt_1, (k+1)t_1). \end{cases}$$

and  $k$  is defined in terms of  $t$  as in (C.18). Similar calculations can be used to simplify the last two terms in (C.17). Hence we obtain

$$v_x(0, t) = \Psi_0(t) := \frac{-\mu}{c} 1^e(ct) - \frac{g}{c} \int_0^t 1^e(c\tau) d\tau. \quad (\text{C.20})$$

Returning to the original system (C.1)–(C.7), we see that inequality (C.3) is maintained if and only if  $\Psi_r(t) \leq 0$ . Therefore, we have the following result that defines time  $t_b$  of the first bounce in equation (C.9).

**The case  $g > 0$ :** The stress function  $\Psi_0(t)$  becomes

$$\Psi_0(t) = -\frac{\mu}{c}1^e(ct) - \frac{g}{c} \int_0^t 1^e(c\tau) d\tau. \quad (\text{C.21})$$

The function  $\Psi_0(t)$  is piecewise linear and  $2t_1$ -periodic.

**Corollary 21** *Assume  $r = 0$  and  $g > 0$  and  $\mu > 0$ . There is a first bounce at time  $t_b \geq t_1$  for which*

- (i) *if  $\mu \geq gt_1$ , the first bounce time is  $t_b = t_1$*
- (ii)  *$0 < \mu < gt_1$ , the first bounce time is  $t_b = 2t_1 - \frac{\mu}{g}$ .*

**Proof** Note that  $\Psi_0(0) < 0$  and is strictly decreasing for  $t \in (0, t_1)$ . Therefore  $t_b \geq t_1$ .

For part (i), in order for a bounce to occur at time  $t_1$ , the stress function  $\Psi_0(t)$  has to change sign at time  $t_1$ . By Proposition 20,  $[u_x(0, t_1)] = 2\mu/c$ . Hence, the condition for a bounce is  $\Psi_0(t_1^-) + 2\mu/c \geq 0$ , which simplifies to  $\mu \geq gt_1$ .

Part (ii) is easy to prove since the stress function in (C.21) is piecewise linear.  $\square$

### Fourier series for finding the solution

Now consider the general problem

$$\begin{cases} v_{tt} - 2rv_{xxt} - c^2v_{xx} = -g, & (x, t) \in \Omega_L \times (0, t_b), \\ v(x, 0) = 0, \quad v_t(x, 0) = -\mu, & x \in \Omega_L, \\ v(0, t) = 0, \quad v_x(L, t) = 0, & t \in (0, t_b). \end{cases} \quad (\text{C.22})$$

Let  $\alpha_k = (k\pi + \pi/2)/L$ . Note that  $\varphi_k(x) = \sqrt{\frac{2}{L}} \sin(\alpha_k x)$  for  $k = 0, 1, \dots, \infty$  is an orthonormal basis, i.e.

$$\int_0^L \varphi_k(x)\varphi_j(x) dx = \begin{cases} 0, & k \neq j, \\ 1, & k = j, \end{cases}$$

because

$$\begin{aligned} -D^2\varphi_k(x) &= \alpha_k^2\varphi_k(x) := \lambda_k\varphi_k(x) \\ \varphi(0) &= 0, \quad \varphi_x(L) = 0. \end{aligned}$$

Since  $f = \sum(f, e_k)e_k = f_k e_k$ , and  $1 = \sum(1, e_k)e_k = \sum \beta_k \phi_k$ , we found

$$1 = \sum_{k=0}^{\infty} \beta_k \varphi_k = \sum_{k=0}^{\infty} \left( \sqrt{\frac{2}{L}} \frac{L}{k\pi + \pi/2} \right) \left( \sqrt{\frac{2}{L}} \sin(\alpha_k x) \right), \quad (\text{C.23})$$

since

$$\beta_k = \langle 1, \varphi_k \rangle = \int_0^L \varphi_k dx = \int_0^L \sqrt{\frac{2}{L}} \sin(\alpha_k x) dx = \sqrt{\frac{2}{L}} \frac{L}{k\pi + \pi/2}.$$

Likewise, with

$$\begin{aligned} v(x, t) = \sum_{k=0}^{\infty} (v_k(t)\varphi_k(x)) &= \sum_{k=0}^{\infty} \left( v_k(t) \sqrt{\frac{2}{L}} \sin(\alpha_k x) \right) \\ &= \sum_{k=0}^{\infty} \left( v_k(t) \sqrt{\frac{2}{L}} \sin\left(\frac{k\pi + \pi/2}{L} x\right) \right), \end{aligned} \quad (\text{C.24})$$

where  $v_k$  satisfies

$$\begin{aligned} v_k(0) &= 0, \quad (v(x, 0) = 0) \\ v_k'(0) &= -\mu\beta_k, \quad (\text{by expansion of } 1, v_t(x, 0) = -\mu). \end{aligned}$$

Thus  $\alpha_k = (k\pi + \pi/2)/L$ . Also, by plugging into (C.1), one obtains the ODE as below

$$\begin{cases} v_k''(t) + 2r\alpha_k^2 v_k'(t) + c^2\alpha_k^2 v_k(t) = -g\beta_k, & (x, t) \in \Omega_L \times (0, t_b), \\ v_k(0) = 0, \quad v_k'(0) = -\mu\beta_k, & x \in \Omega_L, \end{cases} \quad (\text{C.25})$$

where  $\alpha_k = (k\pi + \pi/2)/L$  and  $\beta_k = \sqrt{\frac{2}{L}} \frac{L}{k\pi + \pi/2}$ . Using Mathematica, one can easily get the solution.

## Energy

Define energy  $\mathcal{E}(t) = \frac{1}{2} \int_0^L ((v_t(x, t))^2 + c^2 v_x(x, t)^2) dx + Lgh(t)$ . One can get Fourier expansions and plug in here to get the approximated numerical value for energy. The derivative here

can be seen from below

$$\begin{aligned}
\frac{d\mathcal{E}(t)}{dt} &= \int_0^L v_t(2rv_{xxt} - g) dx + gP(t) \\
&= \int_0^L 2rv_tv_{xxt} dx = 2r \int_0^L v_t dv_{xt} \\
&= 2r \left( v_tv_{xt}|_0^L - \int_0^L v_{xt}v_{xt} dx \right) \\
&= -2r \int_0^L (v_{xt})^2 dx.
\end{aligned}$$

Then

$$\Delta\mathcal{E} = \mathcal{E}(T) - \mathcal{E}(0) = -2r \int_0^T \int_0^L (v_{xt})^2 dx dt. \quad (\text{C.26})$$

Note that

$$\mathcal{E}(0) = \frac{1}{2} \int_0^L \mu^2 dx + Lg0 = \frac{1}{2} \mu^2 L.$$

Define instantaneous dissipation rate as

$$E(t) := \int_0^L (v_{xt})^2 dx. \quad (\text{C.27})$$

Then

$$\Delta\mathcal{E}(t) = -2r \int_0^t E(s) ds.$$

To compute  $E(t)$ , and eventually  $\mathcal{E}(T) = \mathcal{E}(0) - 2r \int_0^T \int_0^L (v_{xt})^2 dx dt$ , there are two ways:

**(1) Numerically Plug in** When computing  $\int_0^T \int_0^L (v_{xt})^2 dx dt$ , one can use the fourier expansion from (C.24) for finite number of terms numerically. But this method usually costs a lot of time for computing.

**(2) Using the eigenvalues**

$$\begin{aligned}
E(t) &= \int_0^L (v_{xt})^2 dx = \int_0^L v_{xt} d(v_t) \\
&= v_tv_{xt}|_0^L - \int_0^L v_tv_{xxt} dx \\
&= - \int_0^L v_tv_{xxt} dx \\
&= \int_0^L v_t(\mathcal{A}v_t) dx.
\end{aligned} \quad (\text{C.28})$$

Here the operator  $\mathcal{A} := -D^2$ . Since  $v(x, t) = \sum_{k=0}^{\infty} (v_k(t)\varphi_k(x))$ , we have

$$v_t(x, t) = \sum_{k=0}^{\infty} (v'_k(t)\varphi_k(x))$$



and

$$\mathcal{A}v_t(x, t) = \sum_{k=0}^{\infty} (v'_k(t) \alpha_k^2 \varphi_k(x)).$$

Then

$$\begin{aligned} E(t) &= \int_0^L \sum_{j=0}^{\infty} (v'_j(t) \varphi_j(x)) \sum_{k=0}^{\infty} (v'_k(t) \alpha_k^2 \varphi_k(x)) dx. \\ &= \sum_{k=0}^{\infty} (v'_k(t)^2 \alpha_k^2). \end{aligned} \quad (\text{C.29})$$

This way is a lot faster when computing since integration in  $x$  is not needed. Here are some plots.

(1) Fig. C.1 is numerically computing  $v(x, t)$ , with parameters:  $tot = 9; g = 9.8; L = 5.0; c = 60; r = 18.0; \mu = 5; T = 2L/c$ .

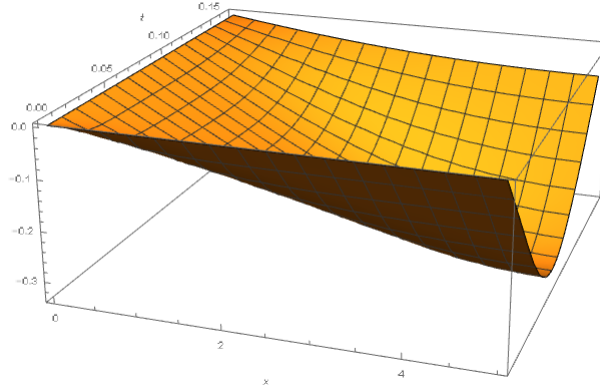


Figure C.1: Plot for  $v(x, t)$ , with parameters:  $tot = 9; g = 9.8; L = 5.0; c = 60; r = 18.0; \mu = 5; T = 2L/c$ .

(2) Fig. C.2 is numerically computing  $v_x(0, t)$ ,  $t$  from range  $(0, 2L/c + 2L/(10c))$ , with parameters:  $tot = 9; g = 9.8; L = 5.0; c = 60; r = 18.0; \mu = 5; T = 2L/c$ . The orange point is at  $t = 2L/c$ . The intercept point after the orange point is approximately  $t =$ , which indicates the bounce time  $t_b \simeq 0.184$  is bigger than  $2L/c$ .

(3) Fig. C.3 is numerically computing  $E(t), t = 0 T$  using (C.29), with parameters:  $tot = 9; g = 9.8; L = 5.0; c = 60; r = 18.0; \mu = 5; T = 2L/c$ . One can also use (C.27) to numerically compute and get this graph, but it will take longer and may not be as accurate.

(4) This Fig. C.4 is the plot for  $\int_0^T v_{xt}^2 dt$  with 5 terms.

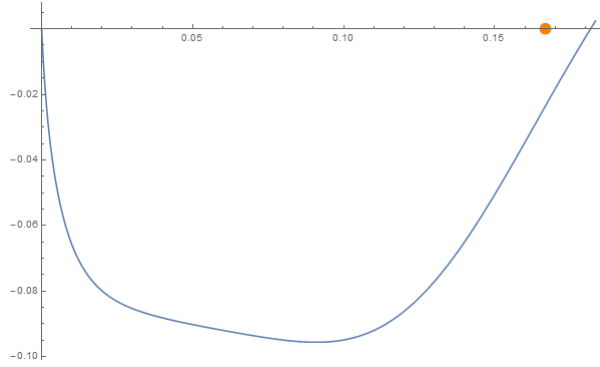


Figure C.2: Plot for  $v_x(0, t)$ , with parameters  $tot = 9; g = 9.8; L = 5.0; c = 60; r = 18.0; \mu = 5; T = 2L/c$ .

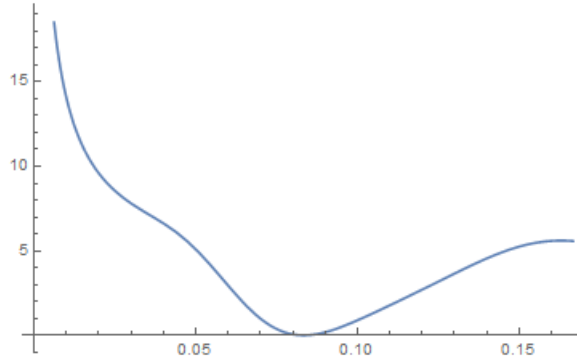


Figure C.3: Plot for  $E(t), t = 0 T$  using (C.29), with parameters  $tot = 9; g = 9.8; L = 5.0; c = 60; r = 18.0; \mu = 5; T = 2L/c$ .

(5) This Fig. C.5 is the plot for  $\int_0^T v_{xt}^2 dt$  computed with 9 terms in expansion. This graphs indicates that approximately half of the overall damping is due to the 20 percent of the round near the ground.

(6) This Fig. C.6 is the plot for summary of energetic coefficient of restitution computed by  $(\mathcal{E}(0) + \Delta\mathcal{E}(t))/\mathcal{E}(0)$ .

The parameters for rubber are:  $r_0 = 1; r_{end} = 200; epsilon = (r_{end} - r_0)/10; Num = 20; tot = 20; g = 9.8; L = 5.0; c = 60; mu = 5; T = 2L/c$ ; The parameters for steel are the same except:  $c = 4984.45$ . The parameters for concrete are the same except:  $c = 3500$ . For various values of  $r$ , the coefficient of restitution of steel and concrete vary between 0.8 and 1.0. These values seem to be in agreement with experimental data found in the literature.

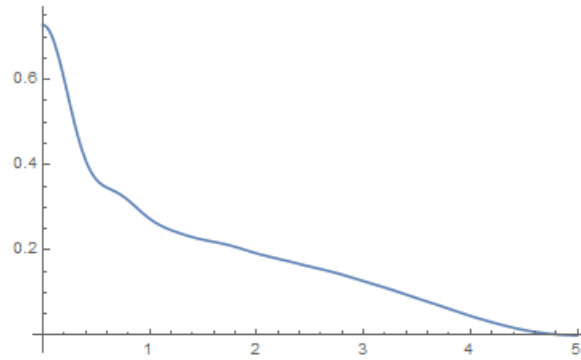


Figure C.4: Plot for  $\text{Integrate}(v_{xt}^2, t, 0, T)$ , with parameters  $tot = 9; g = 9.8; L = 5.0; c = 60; r = 18.0; \mu = 5; T = 2L/c$ .

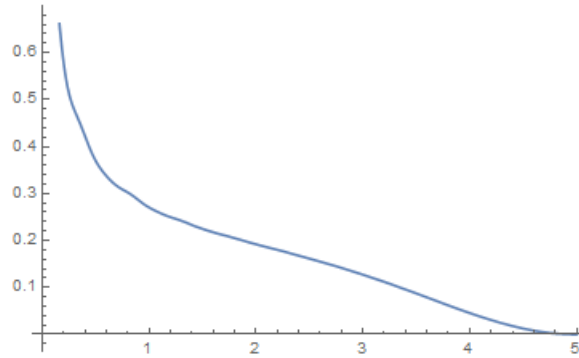


Figure C.5: Plot for  $\text{Integrate}(v_{xt}^2, t, 0, T)$ , with parameters  $tot = 9; g = 9.8; L = 5.0; c = 60; r = 18.0; \mu = 5; T = 2L/c$  with more terms.

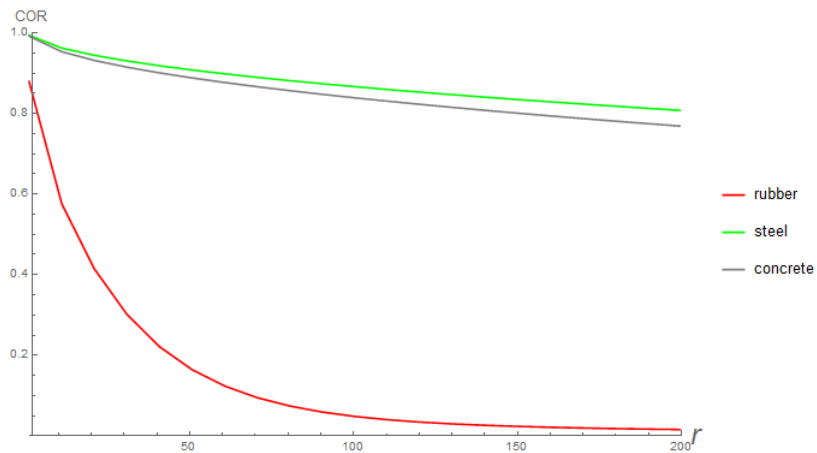


Figure C.6: summary of COR computed by  $(\mathcal{E}(0) + \Delta\mathcal{E}(t))/\mathcal{E}(0)$ .

## Bibliography

- Acary, V. and Brogliato, B. (2003). Concurrent multiple impacts modelling: Case-study of a 3-ball chain. In *Computational Fluid and Solid Mechanics. Second Mit Conference*. Elsevier.
- Ahn, J. (2007). A vibrating string with dynamic frictionless impact. *Applied numerical mathematics*, 57(8):861–884.
- Ahn, J. and Stewart, D. E. (2009). Dynamic frictionless contact in linear viscoelasticity. *IMA journal of numerical analysis*, 29(1):43–71.
- Ammar-Khodja, F., Micu, S., and Münch, A. (2010). Controllability of a string submitted to unilateral constraint. In *Annales de l’Institut Henri Poincaré (C) Non Linear Analysis*, volume 27, pages 1097–1119. Elsevier.
- Bhatt, V. and Koechling, J. (1995). Three-dimensional frictional rigid-body impact. *Journal of applied mechanics*, 62(4):893–898.
- Brach, R. M. (1989). Rigid body collisions. *Journal of Applied Mechanics*, 56(1):133–138.
- Ceanga, V. and Hurmuzlu, Y. (2001). A new look at an old problem: Newtons cradle. *Journal of applied mechanics*, 68(4):575–583.
- Chatterjee, A. and Ruina, A. (1998). A new algebraic rigid-body collision law based on impulse space considerations. *Journal of Applied Mechanics*, 65(4):939–951.
- Cross, R. (2009). Mechanics of swinging a bat. *American Journal of Physics*, 77(1):36–43.
- Elkaranshawy, H. (2007). Rough collision in three-dimensional rigid multi-body systems. *Proceedings of the Institution of Mechanical Engineers, Part K: Journal of Multi-body Dynamics*, 221(4):541–550.

- Gardner, M., Jia, Y.-B., and Lin, H. (2016). Batting flying objects to the target in 2d. In *Intelligent Robots and Systems (IROS), 2016 IEEE/RSJ International Conference on*, pages 3225–3232. IEEE.
- Glocker, C. and Pfeiffer, F. (1995). Multiple impacts with friction in rigid multibody systems. *Nonlinear Dynamics*, 7(4):471–497.
- Han, I. and Park, S.-U. (2001). Impulsive motion planning for positioning and orienting a polygonal part. *The International Journal of Robotics Research*, 20(3):249–262.
- Hertz, H. (1882). Über die berührung fester elastischer körper.
- Higuchi, T. (1985). Application of electromagnetic impulsive force to precise positioning tools in robot systems. In *International Symposium on Robotics Research*, pages 281–285.
- Hirai, S., Niwa, M., and Kawamura, S. (1999a). Development of impulsive object sorting device with air floating. In *International Conference on Robotics and Automation*, pages 3065–3070. IEEE.
- Hirai, S., Niwa, M., and Kawamura, S. (1999b). Development of impulsive object sorting device with air floating. In *Robotics and Automation, 1999. Proceedings. 1999 IEEE International Conference on*, volume 4, pages 3065–3070. IEEE.
- Huang, W. H. and Mason, M. T. (2000a). Mechanics, planning, and control for tapping. *The International Journal of Robotics Research*, 19(10):883–894.
- Huang, W. H. and Mason, M. T. (2000b). Mechanics, planning, and control for tapping. *The International Journal of Robotics Research*, 19(10):883–894.
- Jia, Y. (2012a). Three-dimensional impact: energy-based modeling of tangential compliance. *The International Journal of Robotics Research*, 32(1):56–83.
- Jia, Y. (2015). Planning the motion of a sliding and rolling sphere under friction. *Accepted to the IEEE International Conference on Robotics and Automation, Seattle, WA*.

- Jia, Y., Mason, M., and Erdmann, M. (2012). Multiple impacts: A state transition diagram approach. *The International Journal of Robotics Research*, 32(1):84–114.
- Jia, Y. and Wang, F. (2017). Analysis and computation of two body impact in three dimensions. *Journal of Computational and Nonlinear Dynamics*, 12(4):041012–1–041012–16.
- Jia, Y.-B. (2012b). Three-dimensional impact: energy-based modeling of tangential compliance. *The International Journal of Robotics Research*, page 0278364912457832.
- Jia, Y.-B., Mason, M., and Erdmann, M. (2009). A state transition diagram for simultaneous collisions with application in billiard shooting. In *Algorithmic Foundation of Robotics VIII*, pages 135–150. Springer.
- Jia, Y.-B. and Wang, F. (2016). Analysis and Computation of Two Body Impact in Three Dimensions . <http://web.cs.iastate.edu/~jia/papers/CND16-submit.pdf>.
- John, F. (1982). Partial differential equations, volume 1 of applied mathematical sciences.
- Johnson, K. L. and Johnson, K. L. (1987). *Contact mechanics*. Cambridge university press.
- Kirkpatrick, P. (1963). Batting the ball. *American Journal of Physics*, 31(8):606–613.
- Lab, S. B. (2016). bowling-pin-specification. <http://biosport.ucdavis.edu/research-projects/bowling-dynamics-2/>.
- Lebeau, G. and Schatzman, M. (1984). A wave problem in a half-space with a unilateral constraint at the boundary. *Journal of differential equations*, 53(3):309–361.
- Lin, H., Guo, F., Wang, F., and Jia, Y.-B. (2014). Picking up soft 3d objects with two fingers. In *2014 IEEE International Conference on Robotics and Automation (ICRA)*, pages 3656–3661. IEEE.
- Lipscombe, P. and Pellegrino, S. (1993). Free rocking of prismatic blocks. *Journal of engineering mechanics*, 119(7):1387–1410.

- Liu, C., Zhao, Z., and Brogliato, B. (2008). Frictionless multiple impacts in multibody systems. i. theoretical framework. *Proceedings of the Royal Society of London A: Mathematical, Physical and Engineering Sciences*, 464(2100):3193–3211.
- Liu, C., Zhao, Z., and Brogliato, B. (2009). Frictionless multiple impacts in multibody systems. ii. numerical algorithm and simulation results. *Proceedings of the Royal Society A: Mathematical, Physical and Engineering Science*, 465(2101):1–23.
- Liu, S., Wu, L., and Lu, Z. (2007). Impact dynamics and control of a flexible dual-arm space robot capturing an object. *Applied mathematics and computation*, 185(2):1149–1159.
- Love, A. E. H. (1905). *A treatise on the mathematical theory of elasticity*, volume 1. Cambridge University Press.
- McOwen, R. C. (1996). *Partial differential equations: Methods and applications*. .
- Moll, M. and Erdmann, M. A. (2002). Manipulation of pose distributions. *The International Journal of Robotics Research*, 21(3):277–292.
- Partridge, C. B. and Spong, M. W. (2000). Control of planar rigid body sliding with impacts and friction. *The International Journal of Robotics Research*, 19(4):336–348.
- Rivera, J. and Oquendo, H. P. (1999). Exponential decay for a contact problem with local damping. *FUNKCIALAJ EKVACIOJ SERIO INTERNACIA*, 42(3):371–388.
- Senoo, T., Namiki, A., and Ishikawa, M. (2004). High-speed batting using a multi-jointed manipulator. In *Robotics and Automation, 2004. Proceedings. ICRA'04. 2004 IEEE International Conference on*, volume 2, pages 1191–1196. IEEE.
- Shi, P. (1998a). The restitution coefficient for a linear elastic rod. *Mathematical and computer modelling*, 28(4):427–435.
- Shi, P. (1998b). Simulation of impact involving an elastic rod. *Computer methods in applied mechanics and engineering*, 151(3):497–499.

- Smith, C. E. (1991). Predicting rebounds using rigid-body dynamics. *Journal of Applied Mechanics*, 58(3):754–758.
- Stewart, D. E. (2000). Rigid-body dynamics with friction and impact. *SIAM review*, 42(1):3–39.
- Stronge, W. (2004a). *Impact mechanics*. Cambridge university press.
- Stronge, W. J. (2004b). *Impact mechanics*. Cambridge university press.
- Tagawa, K., Hirota, K., and Hirose, M. (2010). *Manipulation of dynamically deformable object using impulse-based approach*. INTECH Open Access Publisher.
- Walker, I. D. (1994). Impact configurations and measures for kinematically redundant and multiple armed robot systems. *IEEE transactions on robotics and automation*, 10(5):670–683.
- Wang, F., Lin, H., and Jia, Y.-B. (2015). Computational modeling of n-body collisions. In *Intelligent Robots and Systems (IROS), 2015 IEEE/RSJ International Conference on*, pages 5376–5381. IEEE.
- Wang, Y., Kumar, V., and Abel, J. (1992). Dynamics of rigid bodies undergoing multiple frictional contacts. In *International Conference on Robotics and Automation*, pages 2764–2769. IEEE.
- Wang, Y. and Mason, M. (1987). Modeling impact dynamics for robotic operations. In *Robotics and Automation. Proceedings. 1987 IEEE International Conference on*, volume 4, pages 678–685. IEEE.
- Yuen, H. K., Princen, J., Illingworth, J., and Kittler, J. (1990). Comparative study of hough transform methods for circle finding. *Image and vision computing*, 8(1):71–77.
- Zhang, H., Brogliato, B., and Liu, C. (2014). Dynamics of planar rocking-blocks with coulomb friction and unilateral constraints: comparisons between experimental and numerical data. *Multibody System Dynamics*, 32(1):1–25.